UNIVERSITY OF RIJEKA
FACULTY OF PHYSICS

Sherif Kamal

SPECTROSCOPY AND MICROSCOPY OF PRISTINE AND DECORATED EPITAXIAL BOROPHENE ON IRIDIUM

DOCTORAL THESIS

Rijeka, 2026

UNIVERSITY OF RIJEKA
FACULTY OF PHYSICS

Sherif Kamal

SPECTROSCOPY AND MICROSCOPY OF PRISTINE AND DECORATED EPITAXIAL BOROPHENE ON IRIDIUM

DOCTORAL THESIS

Supervisor:
dr. sc. Marin Petrović

Co-supervisor:
Assoc. Prof. dr. sc. Iva Šarić Janković

Rijeka, 2026

SVEUČILIŠTE U RIJECI
FAKULTET ZA FIZIKU

Sherif Kamal

SPEKTROSKOPIJA I MIKROSKOPIJA ČISTOG I FUNKCIONALIZIRANOG EPITAKSIJALNOG BOROFENA NA IRIDIJU

DOKTORSKA DISERTACIJA

Mentor:
dr. sc. Marin Petrović

Komentorica:
Izv. prof. dr. sc. Iva Šarić Janković

Rijeka, 2026

Mentor rada: dr. sc. Marin Petrović, Institut za fiziku, Zagreb

Komentorica rada: izv. prof. dr. sc. Iva Šarić Janković, Fakultet za fiziku, Sveučilište u Rijeci

Doktorski rad obranjen je dana _________________________ u/na______________________ ________________________, pred povjerenstvom u sastavu:

1. ____
2. ____
3. ____
4. ____
5. ____

This thesis was written under the supervision of Dr Marin Petrović as a part of the doctoral study programme in condensed matter physics at the Faculty of Physics at the University of Rijeka. Presented experimental work was carried out at the Institute of Physics (IFS) in Zagreb, Solaris Synchrotron in Krakow in Poland, Elettra Sincrotrone Trieste in Italy, the Faculty of Physics at the University of Rijeka and MESA+ Institute at University of Twente in the Netherlands.

ACKNOWLEDGEMENTS

This work would not have been achieved without the support of: my supervisor Dr Marin Petrović and co-supervisor Dr Iva Šarić Janković whom I would like to thank deeply for the masterful guidance and patience. Special thanks to Dr Marko Kralj, the leader of Surface, interfaces and 2D materials research group (SIMAT) for giving me the opportunity to work in the group. I feel grateful to all members of SIMAT research group, in particular Dr Borna Radatović and Patrick Seleš for conducting AFM measurements, Dr Martina Lihter for providing access to recently published papers, Dr Iva Šrut Rakić and Dr Nataša Vujičić for the thorough review of the thesis and suggested corrections. My appreciation also extends to Dr Petar Pervan for his elaboration on the fundamentals of surface physics and theoretical foundations of photoemission techniques and Dr Branko Gumhalter for fruitful discussions about theoretical aspects of photoemission spectroscopy.

I am thankful for external research collaborators Dr Insung Seo and Prof. Dr Yoshihiro Gohda of Tokyo Institute of Technology for DFT calculations. Dr Paulina Sheverdyaeva, Dr Paolo Moras and Dr Andrey Matetskii of VUV beamline at Elettra, Dr Matteo Jugovac, Dr Tevfik Onur Mentes, Dr Carlo Alberto Brondin and Dr Andrea Locatelli of the Nanospectroscopy beamline at Elettra.

My appreciation also extends to PIN research group staff for all support and hospitality they demonstrated during my two-month research stay at the University of Twente in the Netherlands, especially the host supervisor Dr Pantelis Bampoulis, the group leader Prof. Dr Harold Zandvliet, Dr Arie van Houselt, Martin Siekman, Esra van ‘t Westende and Dennis Klaassen. My gratitude extends to other colleagues with whom I had fruitful discussions during the PhD journey in particular Dr Yaroslav Zhumagulov and Dr Stefan van Vliet for the big picture discussions about materials science in our time.

I convey my gratitude to Prof. Dr Zoran Kaliman who encouraged me to enrol into the Engineering and Physics of Materials Master’s programme at the University of Rijeka, without which I would have been unable to embark on my PhD journey. My thankfulness extends to Dr Robert Peter for reviewing the thesis draft and providing suggestions.

The laboratories in the Institute of Physics (IFS) in Zagreb were supported through the Center of Excellence for Advanced Materials and Sensing Devices (ERDF grant no. KK.01.1.1.01.0001) and Centre for Advanced Laser Techniques (ERDF Grant KK.01.1.1.05.0001), co-financed by the Croatian Government and the European Union through the European Regional Development Fund - Competitiveness and Cohesion Operational Program. Research within this thesis was also funded by the Croatian Science Foundation project “Boron-based 2D materials”, UIP 2020-02-1732 and the MOBDOK-2023-9676 project. The laboratory equipping at the University of Rijeka was supported by infrastructural ERDF project no. RC.2.2.06-0001: “Research Infrastructure for Campus-based Laboratories at the University of Rijeka – RISK.”

Abstract

Borophene (Bo), a polymorphic 2D sheet of boron atoms, has been intensely researched over the past decade. Several Bo polymorphs have been predicted to be metallic and hosting Dirac cones, thus representing an alternative to graphene and other atomically-thin 2D metals. Motivated by these and many other interesting properties of Bo, I have investigated single-phase Bo samples of high coverage in terms of their nanoscopic morphology and electronic band structure. Furthermore, my work on the Bo decoration, as a viable route for modification of Bo's intrinsic properties, is governed by potential applications of Bo in electric batteries and gas storage systems. In an attempt to comprehensively characterize the electronic properties of pristine Bo after growing it on Ir(111) substrate, data from photoemission spectroscopies and scanning probe techniques have been integrated with density functional theory calculations. The non-uniform bonding between pristine Bo and iridium, confirmed by X-ray photoelectron spectroscopy and scanning tunnelling microscopy / spectroscopy data, was found to be the reason behind the Bo stripy structure characterized by nanoscopic and unidirectional modulation. The modulation accounts for the observed replicated bands in the angle-resolved photoemission spectroscopy spectra. Therefore, the stripe-like Bo sheet, acts as a diffraction grating for the photoelectrons. Afterwards, *in situ* and *ex situ* Bo ageing was investigated along with possible routes for restoring the pristine structure of Bo through annealing cycles in ultra-high vacuum. Also, the band structure of a freshly-made Bo sample was manipulated through its decoration with Li atoms which is related to charge transfer effects within the system. The present studies contribute to the understanding of the fundamental structural and electronic properties of the investigated Bo polymorph, which is indispensable for materializing its applicative potential.

Keywords: 2D materials, borophene, iridium, Umklapp bands, surface states, Li decoration, ageing

Sažetak

Borofen (Bo), polimorfni 2D sloj atoma bora, intenzivno je istraživan tijekom posljednjeg desetljeća. Predviđeno je da su nekoliko polimorfa Bo metalni i da sadrže Diracove konuse, što predstavlja alternativu grafenu i drugim atomski tankim 2D metalima. Motiviran ovim i mnogim drugim zanimljivim svojstvima Bo, istražio sam jednofazne uzorke Bo visoke pokrivenosti u smislu njihove nanoskopske morfologije i elektroničke strukture vrpci. Nadalje, moj rad na dekoraciji Bo, kao održivom putu za modifikaciju intrinzičnih svojstava Bo, određen je potencijalnim primjenama Bo u električnim baterijama i sustavima za pohranu plina. U pokušaju da se sveobuhvatno karakteriziraju elektronička svojstva čistog Bo nakon uzgoja na Ir(111) podlozi, podaci iz fotoemisijske spektroskopije i tehnika skenirajuće sonde integrirani su s izračunima teorije funkcionalne gustoće. Utvrđeno je da je nejednoliko vezanje između čistog Bo i iridija, potvrđeno rendgenskom fotoelektronskom spektroskopijom i podacima skenirajuće tunelske mikroskopije / spektroskopije, razlog prugaste strukture Bo karakterizirane nanoskopskom i jednosmjernom modulacijom. Modulacija objašnjava uočene replicirane vrpce u spektrima fotoemisijske spektroskopije razlučene pod kutom. Stoga, trakasti sloj borofena djeluje kao difrakcijska rešetka za fotoelektrone. Nakon toga, istraženo je in situ i ex situ starenje borofena, zajedno s mogućim putevima za vraćanje izvorne strukture borofena kroz cikluse žarenja u ultra visokom vakuumu. Također, struktura vrpci svježe pripremljenog uzorka borofena manipulirana je njegovim ukrašavanjem atomima litija, što je povezano s efektima prijenosa naboja unutar sustava. Sadašnja istraživanja doprinose razumijevanju temeljnih strukturnih i elektroničkih svojstava istraživanog polimorfa borofena, što je neophodno za ostvarenje njegovog aplikativnog potencijala.

Ključne riječi: 2D materijali, borofen, iridij, Umklappove vrpce, površinska stanja Li dekoriranje, starenje

Contents

List of abbreviations

1D – one-dimensional

2D – two-dimensional

3D – three-dimensional

ARPES – Angle Resolved Photoemission Spectroscopy

B – Boron

Bo – Borophene

DFT– Density Functional Theory

EUV – Extreme Ultraviolet

FFT – Fast Fourier Transform

FWHM – Full Width at Half Maximum

hBN – hexagonal Boron Nitride

HH – Hexagonal Hole

LEED – Low Energy Electron Diffraction

LEEM – Low Energy Electron Microscopy

Li – Lithium

ML – Monolayer

SBZ – Surface Brillouin Zone

STM – Scanning Tunnelling Microscopy

STS – Scanning Tunnelling Spectroscopy

SS – Surface State

LT – Low Temperature

UHV – Ultra High Vacuum

UV – Ultraviolet

VUV – Vacuum Ultraviolet

XPS – X-ray Photoemission Spectroscopy

Z – Atomic number

1 Introduction

1.1 Graphene and beyond: an overview of elemental 2D materials

The relation among size, morphology and fundamental properties of matter (*e.g.* mechanical, chemical, electrical, magnetic, optical, etc.) is complex: it depends on the scale at which the material is investigated. To illustrate, when reducing any of the spatial dimensions of a physical object to a few nanometres (1 nm = 10^{-9} m), physical properties drastically change due to the pronounced influence of surface effects, structural defects and quantum phenomena [1]. For example, as the spatial dimension *z* – i.e. the thickness – of graphite is diminished to one-atom thick sheet, graphene is formed. Graphene is a rightly semi-metallic nanostructure with a nanoscopic dimension along *z* axis where electrons are confined, and two macroscopic dimensions along *x* and *y* axes where electrons are delocalized, hence rendering it a two-dimensional (2D) material. Such nanostructures usually require a solid substrate for mechanical support. In other words, dimensionality is a crucial defining parameter in materials science nowadays [2].

Graphene was realised in 2004 by graphite exfoliation (Fig. 1.1) for the purpose of studying electric field effect on such a nanostructure [3]. Graphene, characterised by ambient stability [4], high carrier mobility at room temperature due to the energy bands linear dispersion [5 , 6], mechanical robustness [4] and scalable fabrication, was encouraging for researchers to produce other elements of the periodic table in 2D form. Moreover, the zero-band gap of graphene [7, 8] has also been an additional motivation to search for other candidates to be either complementary or alternative 2D materials to graphene as far as potential device applications were concerned. Hence, other 2D materials exhibiting a band gap such as transition metal dichalcogenides (TMDs) have been identified as suitable candidates for use as semiconductors, while hexagonal boron nitride (hBN) and transition metal oxides have a potential to be used as insulators [9].

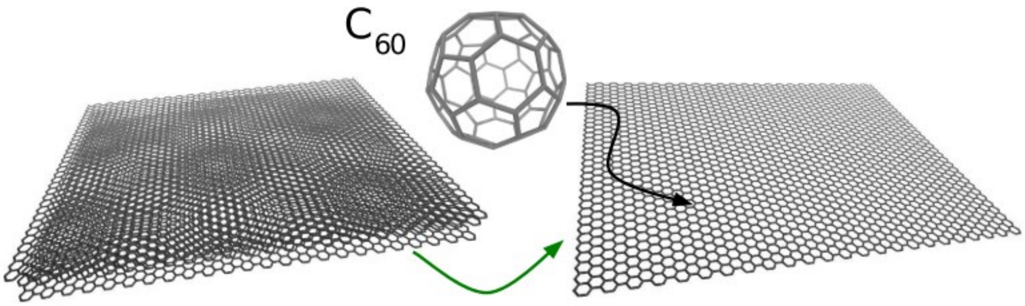

Figure 1.1 Graphene may be exfoliated from graphite, its bulk predecessor. In addition, graphene sheet is conceptually viewed as a planar unfolding of C_{60} molecule. Adopted from [10].

Generally speaking, there are three key advantages of 2D materials over more "conventional" materials: high surface area, reduced dimensionality and easily tuneable electronic structure [11]. The big surface-to-volume ratio is crucial for applications related to catalysis, sensors and energy storage; the latter aspect also benefits from the characteristic high charge capacitance. The reduced dimensionality means that properties of such materials are dominated by quantum effects thanks to their two-dimensional nature. The tuneability of the electronic structure, in particular the electronic bandgap, as in silicene, germanene, and phosphorene, renders such materials ideal for electronics and optoelectronics [12] with an optical response spanning from microwaves to infrared radiation [13]. Also, they are promising in photonics applications due to their potential in manipulation of the propagation and detection of electromagnetic waves [14].

Tuneability of the electronic structure of 2D materials may be realised in response to the following external stimuli: strain, electric field, stacking of different monolayers, doping, adsorption of various atoms or molecules on top of the 2D material (chemical functionalization) or via the intercalation of another material between the 2D material and the substrate [15, 16]. In addition, nanoribbon formation is one effective way for modulating the electronic properties of the parent 2D material. For example, reducing the graphene to a nanoribbon, whose width is less than 10 nm, results in band gap opening, thus rendering graphene semiconducting [17 , 18]. A nanoribbon is an interesting physical system because electrons in such a system are confined in two dimensions: the nanoribbon width (y) and height (z), thus $l(y,z) \lesssim \lambda_F$ where $l(y,z)$ is the critical dimensionality of the system[1] and λ_F is Fermi wavelength of the electron[2] [1]. In other words, electrons behave as if they are in an infinite potential 1D quantum well: the narrower the ribbon, the larger the energy separation between the electronic states. Hence, nanoribbons may provide a platform for 1D-quantum electronically confined system investigation [19].

Returning to the family of elemental 2D materials, the experimentally realised members have expanded beyond graphene as illustrated in the evolution timeline displayed in Fig. 1.2. The atoms in monoelemental sheets adopt a range of structures: honeycomb structure, including puckered variants as in bismuthene or phosphorene [20], octagonal lattice, square lattice and rectangular lattice [12], [21, 22]. In addition, the diversity in lattice structures and differences in the number of valence electrons result in numerous interesting properties. In terms of electronic properties, moving across the periodic table of elements from group II to group VI, elemental 2D materials exhibit a transition from metallic to semi-metallic to semiconducting behaviour [12].

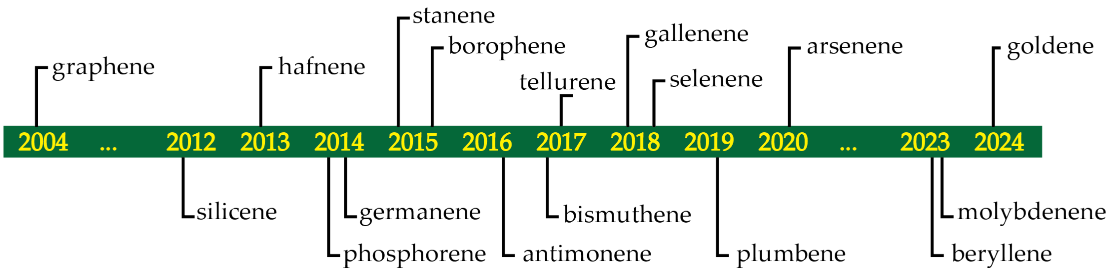

Figure 1.2 Evolution timeline of experimentally realised elemental 2D materials. Adapted from [12].

Spin-orbit coupling in elemental 2D materials is an essential factor influencing the electronic properties. It causes a small bandgap opening around the Dirac cone in 2D materials with a linear band dispersion such as graphene, silicene

---

[1] The spatial dimensions below which the quantum size effect of the system is prevalent.

[2] For metals: $\lambda_F \sim 0.5 - 1$ nm, and for semiconductors: $\lambda_F \sim 200$ nm [1].

and germanene [23]. The coupling strength increases with the increase of the atomic number (Z > 30), consequently candidates such as stanene, antimonene, bismuthene [24] and plumbene [23] are predicted to exhibit quantum spin Hall effect and host non-trivial topology. The non-trivial topology results in the following: a nanoribbon of such material may host both 1D electronic states at its edge (physical border), yielding a non-dissipative electric current, and a band gap within the 2D body of the nanoribbon [23].

The growth of elemental 2D materials is a rapidly advancing field with various methods tailored to different materials and applications. Chemical vapour deposition (CVD) and molecular beam epitaxy (MBE) are leading techniques for producing high-quality monolayers of graphene, silicene and germanene. Although methods like liquid-phase exfoliation and hydrothermal synthesis are scalable, they may result in lower material quality. Laser ablation and sputtering are useful for specialized applications but face challenges in achieving uniform monolayer growth. Deciding on the growth method largely depends on properties sought in the 2D material, scalability, and application requirements. For a well-comprehensive review of the growth methods for the elemental 2D materials, the reader is advised to consult reference [23].

Although the unique properties of elemental 2D materials have promising applications in electronics, photonics and energy storage, overcoming challenges related to synthesis, stability, and integration will be key for their broader adoption in commercial applications [25]. Production of high-quality monolayers of such materials remains a challenge, as many of them are difficult to isolate or maintain under standard conditions [12]. Regarding chemical stability, in contrast to graphene, elemental 2D materials are highly reactive: they either quickly oxidise or decompose when exposed to air. Therefore, either chemical modification [16] or encapsulation of the 2D material would be required in order to achieve its environmental stability, hence its technological exploitation [23]. Finally, integrating such materials with existing technologies still poses a serious challenge.

1.2 Idealistic freestanding borophene

Since the discovery of boron B (Z = 5) in 1808, diverse studies, experimental as well as theoretical, have been conducted on pristine forms (allotropes) of the element and its compounds. Bulk boron, unlike a multitude of 2D materials that are naturally layered and also have 3D counterparts, is not layered [26]. To illustrate, the β-rhombohedral unit cell of bulk boron, shown in Fig. 1.3, consists of 105 atoms and it is not trivial to exploit for fabrication of a single sheet of boron atoms in the top-down approach. Thus, bottom-up synthesis routes of 2D boron are vital.

The first two decades of 21st century witnessed a number of significant theoretical studies on diverse B configurations of reduced (lower) spatial dimensions such as B nanoclusters, B nanotubes and 2D nanosheets of B atoms dubbed borophene (Bo) [27-31] which served as guidelines for experimentalists in the field. Yakobson and co-workers, for instance, did ground-breaking theoretical research on structure, kinetics, and properties of various geometrical configurations of borophenes, derived from macroscopic and fundamental molecular interactions. The group has also worked on theoretical prediction of 2D materials, in particular on their behaviour and physical properties [30-33]. Theoretical prediction of material physical properties is derived from computational models such as density functional theory (DFT) and cluster expansion (CE) that forecast the material existence and model its electronic, mechanical, and thermal properties prior to its synthesis in the laboratory. Predictive modelling, therefore provides a roadmap for experimentalists as it was the case in the early stage of borophene research (see Section 1.3.1): predictions made about Bo stability, synthesis conditions, and potential applications have been a crucial guide for 2D materials research community. For an in-depth treatment of theoretical prediction of 2D materials, the reader is advised to consult the overview given in reference [10].

Borophene's structure may be defined as a triangular mesh of B atoms with periodically arranged hexagonal holes or vacancies [30]. The idealistic triangular structure of Bo has no hexagonal holes (HH) (see Fig. 1.4) which are necessary for the stability of the Bo sheet [34]. Therefore, such a structure is merely a theoretical model used as a starting point for examination of other realistic (*i.e.* obtainable in experiments) Bo polymorphs.

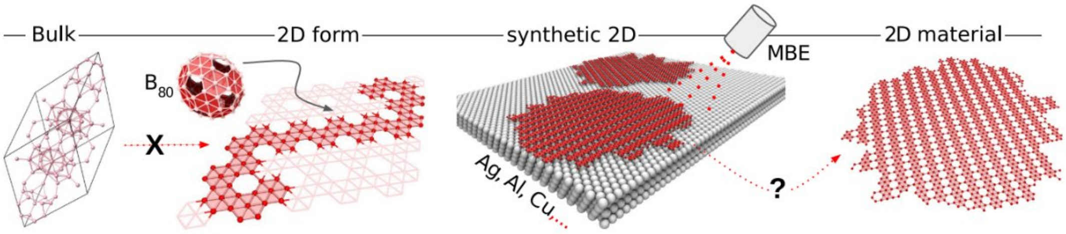

Figure 1.3 The β-rhombohedral unit cell of bulk boron (left), consisting of 105 atoms, is not possible to exfoliate into a single sheet of boron atoms (second from left). The most stable sheet of B atoms, labelled α-sheet, may be conceptually formed by unfolding B_{80} cluster. Molecular-beam epitaxy (MBE) is one of the promising bottom-up synthesis routes to fabricate monolayer borophenes on different substrates (third from left), however decoupling such monolayers from their substrates remains a challenge (right). Adopted from [10].

Favourable Bo structure is conceptually dictated by balancing the surplus of electrons in a triangular B mesh via creation of hexagonal holes. In other words, hexagonal hole formation and metal substrates passivation, as will be shown in Section 1.3, are two ways of realizing Bo in the laboratory. The number η is a characteristic global density parameter [29] of a Bo sheet defined as follows:

$$\eta = \frac{Number\ of\ hexagonal\ holes}{Number\ of\ atoms\ in\ the\ original\ triangular\ lattice}$$

Different Bo polymorphs may share the same η value, therefore the size and basis (*i.e.* B atom arrangement) of Bo unit cell, is an equally important distinction amongst polymorphs as is the η parameter. Most published work on borophenes follow a notation established earlier [29] where the Greek letters α, β, δ, χ, ψ were adopted to label Bo polymorphs. The most stable freestanding Bo polymorph is considered to be α-sheet ($\eta = 1/9$) (shown in Fig. 1.4b) due to the optimal filling of B orbitals *i.e.* all bonding states are occupied while all antibonding states are empty [34]. This stability, however, shifts to other polymorphs when interaction with the substrate is taken into account. The α-sheet may be conceptually thought of as an unfolded B_{80} cluster as sketched in Fig. 1.3, thus providing further analogy with the graphene-fullerene system.

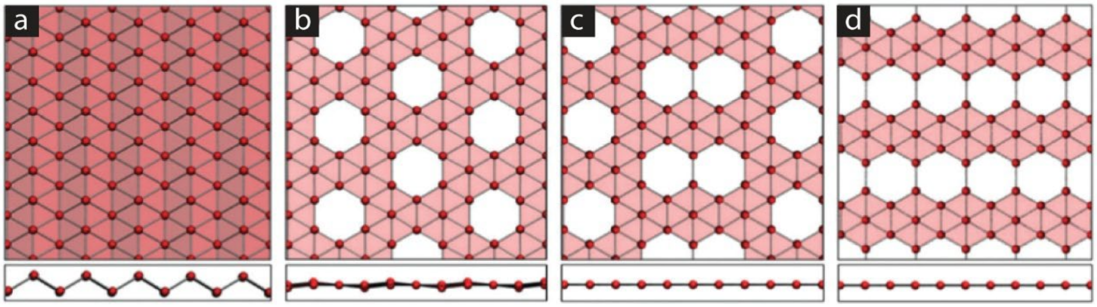

Figure 1.4 Top (upper row) and side (bottom row) views of several different Bo sheets. (a) Ideal free-standing triangular Bo (η = 0) with considerable buckling. Panels (b), (c) and (d) display diverse configurations of HH in Bo sheets of $\eta = 1/9$, $\eta = 1/8$ and $\eta = 1/6$, respectively. The configuration ($\eta = 1/9$) shown in (b) is the most stable freestanding Bo polymorph, called α sheet. Adopted from [33].

The electron deficiency of B atom (Z = 5; $1s^2 2s^2 2p^1$) gives rise to the Bo polymorphism [33] and its high reactivity [35]. As a result, two-centre two-electron (2c2e) and multicentre two-electron bonding co-exist. The covalent bonds endow the sheet with considerable strength while the metallic-like multicentre bonds make the structure potentially flexible [33]. The metallic character of Bo, theoretically predicted via DFT calculations, originates from the delocalization of the p_z orbital over a wide energy range around E_F [33]. Bo metallicity renders the material a potential conductive layer in future flexible electronics [33]. However, the metallic character of Bo polymorphs realised so far are still lacking experimental evidence. For such evidence, transport measurements are yet to be done to estimate the electron mobility which in turn requires mastering the transfer of Bo to an arbitrary substrate. Mazaheri *et al.* could successfully transfer χ_3 polymorph onto a dielectric substrate and obtain a linear current voltage (*I-V)* curve as a confirmation of the polymorph metallicity [36]. Successful transfer of Bo sheets to an arbitrary substrate is a crucial step towards their transfer to a device-compatible substrate [37] .

1.3 Substrate-supported borophene

1.3.1 Crystal structure: polymorphism and stability

For epitaxial Bo systems, it has been predicted that the Bo-sheet geometrical configuration depends on its interactions with the supporting substrate [31]. In other words, different substrates yield different Bo polymorphs as boron vacancies in the Bo triangular lattice stabilise the Bo sheet. Hence, epitaxial growth on metallic substrates of well-defined surface crystallography was thought to be a feasible method for fabrication and stabilisation of 2D boron sheets. Employing first principles calculations in 2013, Liu *et al.* predicted the formation of HH-embedded Bo sheets on metal substrates such as Cu(111), Ag(111), Au(111) and on metal borides such as MgB_2 and TiB_2 [31] (refer to Fig. 1.5) where the coordination number of each B atom may be 3, 4, 5 or 6. Interestingly, the occurrence of HHs within Bo sheets was later predicted to be the reason behind the high storage capacity of Bo, hence its potential usage as an electrode material [38-40].

The first successful experimental realisation of two Bo polymorphs on a metallic substrate, Ag(111), was reported independently by two groups: Mannix and co-workers in 2015 (see Fig. 1.6a-c) [41] and Feng and co-workers in 2016 [42]. This was followed by a surge in publications reporting alternative Bo synthesis routes and investigating the morphology and physical properties of various Bo polymorphs. Synthesis methods of monolayer Bo include molecular beam epitaxy (MBE) from solid boron rods [41, 43, 44], sonochemical exfoliation from boron powders [45, 46], chemical vapor deposition (CVD) from gaseous diborane precursors [36, 47] and segregation-enhanced epitaxy from borazine [48]. This is by no means an exhaustive list of Bo growth methods, the reader may consult the reviews given in references [49-51] for a well-comprehensive treatment of the subject.

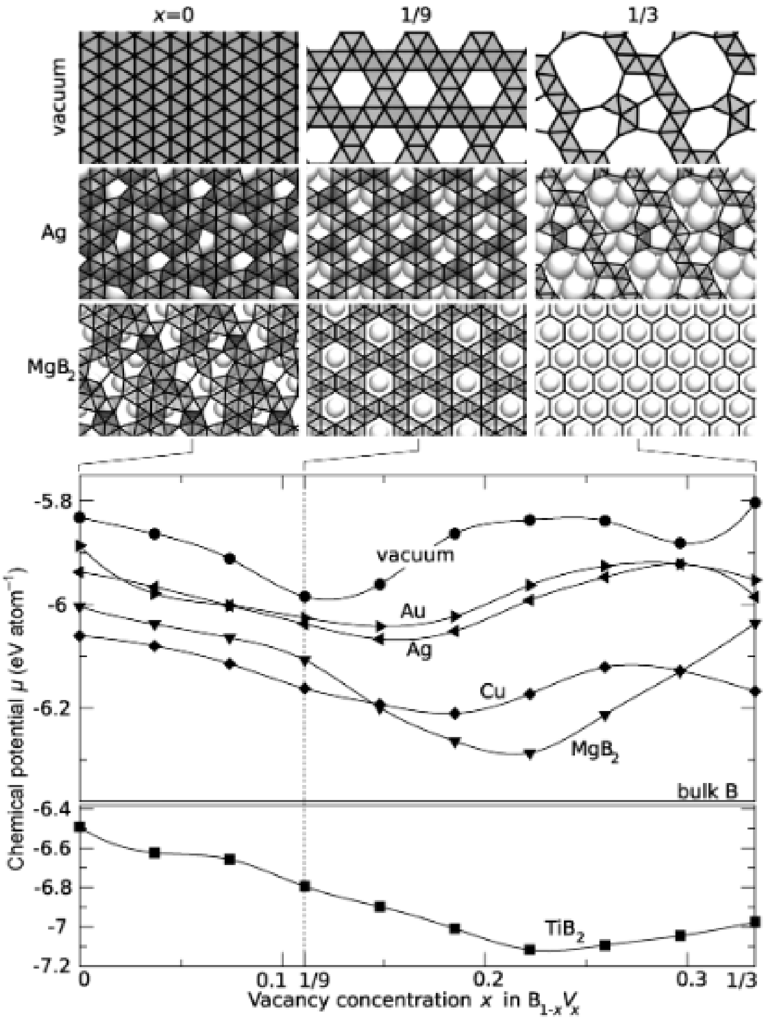

Figure 1.5 Top: schematics of Bo sheets atomic structure (represented by line networks) with different vacancy concentrations x (equivalent to η parameter) in vacuum and on substrates (bright spheres indicate the topmost substrate layer). Bottom: the plots show the chemical potential of Bo sheets as a function of vacancy concentration x in vacuum and on various substrates: Cu(111), Ag(111), Au(111), Mg-terminated MgB_2, and Ti-terminated TiB_2 surfaces. Adopted from [31].

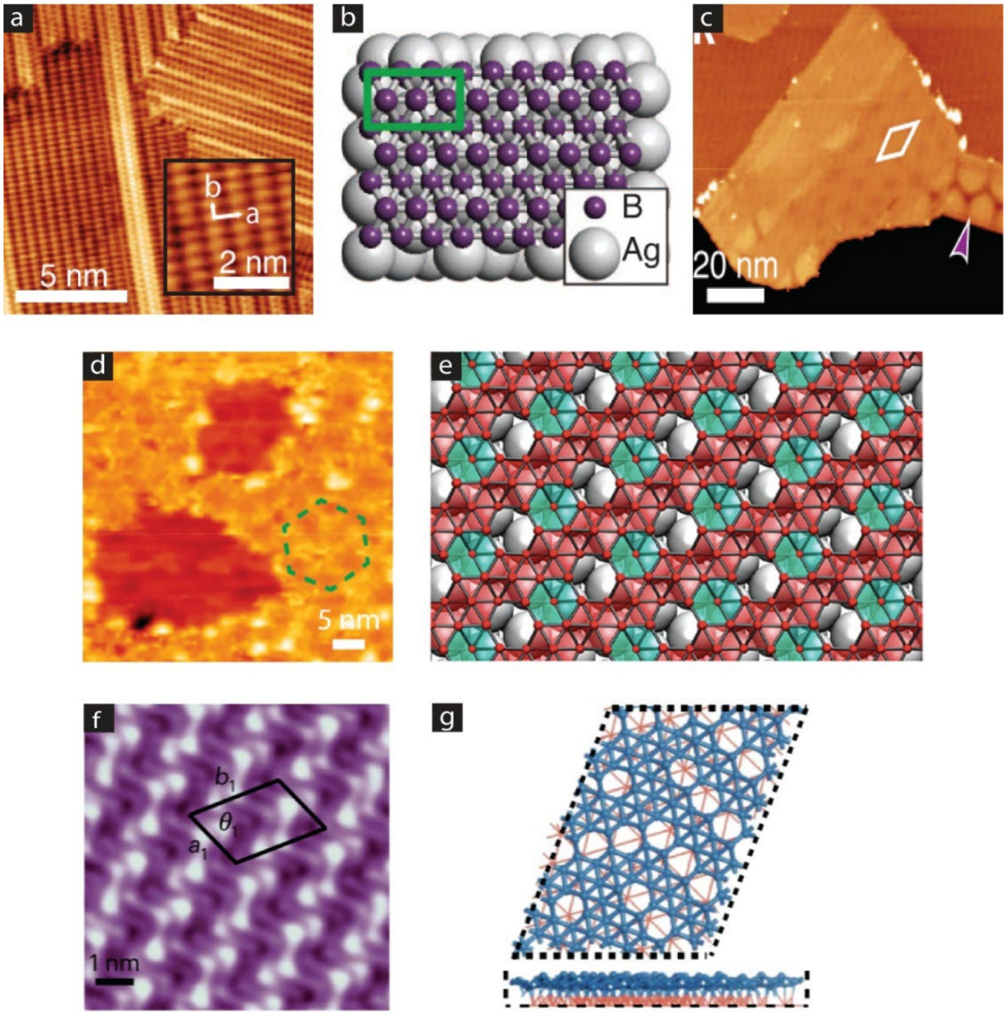

Figure 1.6 STM images and schematic models of monolayer Bo polymorphs grown on three different metallic substrates. (a) striped-phase Bo on Ag(111). The inset displays rectangular lattice with overlaid lattice vectors. (b) Top view sketch of the Bo monolayer. The green rectangle marks the Bo unit cell. (c) Striped phase with two moiré patterns: rhombohedral and honeycomb indicated with white rhombus and purple arrow, respectively [41]. (d) Bo islands on Au(111) and its corresponding structural model (e) [43]. (f) Bo sheet on Cu(111) and its model (g) [52].

A well-defined metal substrate effectively reduces the Bo formation barrier, henceforth provides fine energetic balance towards the emergence of novel epitaxially grown Bo polymorphs [31, 53]. Bo monolayer sheets of different configurations have been experimentally synthesized on the substrates of Ag(111) [41], Au(111) (see Fig. 1.6d-e) [43], Cu(111) [52, 54] (see Fig. 1.6f-g), Ir(111) [48, 55], and Al(111) [56]. It is worth mentioning that the monolayer limit has been surpassed or at least challenged by the synthesis of a bilayer of Bo on a number of well-defined metallic substrates as: Ru(0001) [57], Ag(111) [58] and Cu(111) [52]. Besides the demand for high-quality and large-area synthesis, Bo manipulation for device fabrication and its transfer to arbitrary substrates pose another challenge [33].

Although there are published theoretical predictions of Bo stability and structure on different metallic substrates [31], accompanying valence-band and core-level spectroscopy experiments investigating the electronic structure of the pristine epitaxial Bo systems remain lacking judging by the few publications on the subject. For instance, oxidation [35] and hydrogenation of Bo on Ag(111) [59], recently investigated by some research groups, are two possible routes to stabilise Bo in non-pristine form and retrieve its initial pristine form upon annealing. Further research into other chemical species for stabilizing Bo is still needed.

1.3.2 Physical properties

Physical properties of Bo - such as mechanical, electronic and optical properties- are generally affected by various factors such as temperature, polymorphism and in-plane anisotropy (see Fig. 1.7 for the key properties). For instance, the mechanical properties of Bo may be tuned by varying the concentration of HH [60]. To add, the calculated considerable strength of Bo sheets has been found to originate from B-B bond whereas the multicentre bonding (refer to Section 1.2) provides the sheet with flexibility. When a Bo sheet is mechanically stretched beyond critical strain, it becomes stronger due to the induced phase transition [61]. The mechanical robustness of Bo sheets is an essential condition for a successful transfer to an arbitrary substrate.

Phonon heat capacity and thermal conductance have been theoretically predicted to be inversely proportional to the characteristic η parameter of the Bo sheet: Bo sheets of high η value exhibit low phonon heat capacity and thermal conductance due to the reduced interatomic vibrations as the Bo sheet density decreases [62].

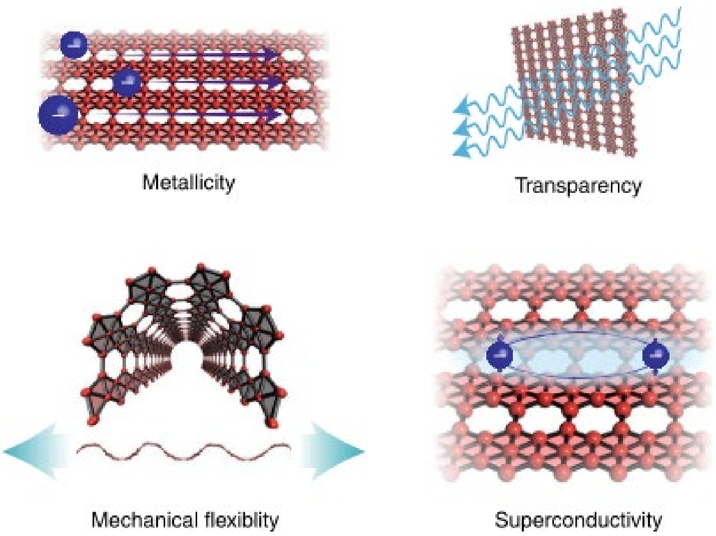

Figure 1.7 Key physical properties of Bo. Adopted from [63].

Electronic structure of Bo can exhibit various interesting features, depending on the particular polymorph, which have been examined both theoretically and experimentally. For example, Dirac cones and superconductivity signatures are being currently intensively investigated in the 2D community [64-66]. Angle-resolved photoemission spectroscopy (APRES) reportedly confirms the existence of gapless conical shaped valence and conduction bands at the Fermi level in two phases of borophene on Ag(111), namely β_{12} and χ_3 sheets [67, 68]. A strong electron–phonon coupling resulting in phonon-mediated superconductivity has been calculated for several Bo polymorphs in references [32, 69]. The predicted critical temperature[3] T_c of various borophenes is influenced by electronic DOS at the Fermi level. However, electron doping and tensile tension of Bo, arising from the atoms of the substrate topmost layer, are two factors deterring the realisation of

---

[3] the temperature below which the material loses its electric resistivity *i.e.* becomes a superconductor.

superconductivity because of their negative impact on the electron-phonon coupling, rendering it a challenge to realise T_c experimentally [70]. Thus, theoretical research on superconductivity in borophenes still lacks experimental verification.

The examination of Bo-substrate interaction, as well as Bo interaction with other atoms and molecules may be used for functionalization of Bo [59]. In this context, borophenes have a potential to serve as materials for energy storage: it has been found that dispersion of alkali metal atoms onto the boron sheet considerably increases hydrogen binding energies and storage capacities. Hence, borophenes are considered potential candidates for hydrogen storage and Li ion batteries. First-principles calculations predict that the most stable site for the spontaneous adsorption of Li to be above the hexagonal hollow sites of the Bo sheet (see Fig. 1.4) [71]. The Li adsorption is characterized by low diffusion energy barriers ~ 0.69 eV [71] and a relatively strong binding energy of ~ 3.28 eV between the Bo sheet and Li adatom [39]. It should be noted that low energy barrier of Li diffusion is desirable for optimal charge-discharge rates of rechargeable batteries [71]. Recently, it has been predicted that the energy barrier of Li diffusion increases by depositing more Li [72] due to the repulsive forces between Li adatoms. In addition, by investigating the effect of adatoms coverage on average adsorption energy, a gradual decrease in the adsorption energy with increasing the coverage of adatoms has been predicted [71]. Also, since the simulated Li adatoms intercalation on Bo exhibit high charge capacity of ~1720 mA h/g, three metallic Bo polymorphs have been later reported to be a potential high-performing anode material for non-lithium-ion batteries [73]. To add, the simulations of Li adatoms on Bo have shown induced lattice distortion, hence deformation of Bo sheet [39]. However, the Bo sheet original structure is retrievable after the separation of Li ions [39]. Borophenes are also likely to exhibit structural phase transition when adsorbing metal atoms as a consequence of charge donation from the adsorbates, however further examination is still required [33].

Bilayer Bo is a system consisting of two Bo layers in which the upper Bo sheet is expected to be less affected by the substrate topmost layer while the layer at the interface is significantly bound to the substrate, thus acting as a buffer [74, 75]. Liu and co-workers reported successful MBE of bilayer Bo on Ag(111) substrate [58]. Using STM and non-contact AFM, they determined the structure of the bilayer Bo to be two sparsely covalently bonded α-phase layers. Field-emission resonance spectroscopy revealed that bilayer Bo has higher crystallinity, revealed by the Stark-shift in image potential states, and work function in comparison with single-layer Bo [58]. Along with induced resilience to chemical degradation, phonon-mediated superconductivity has been theoretically explored in bilayer Bo intercalated with the alkali, alkaline-earth, and transition metal atoms. Such a system is expected to exhibit enhanced T_c values (ranging up to 36 K) compared to its freestanding monolayer counterparts whose predicted T_c ranges up to 33 K (Bo interaction with the substrate would notably suppresses superconductivity rendering T_c much lower, though) [76]. Theoretical calculations demonstrate that superconductivity in bilayer Bo arises from the interplay between the out-plane p_z states of B atom and the partially occupied in-plane (s + p_z) bonding state at the Fermi level [76]. Experimental realisation of such intercalated Bo bilayers has not been reported yet. For an even more detailed overview of recent progress in Bo research, the reader is kindly advised to consult recent review articles such as references [49-51].

1.3.3 χ_6 polymorph: borophene on Ir(111)

A Bo polymorph on the Ir(111) surface, specifically the χ_6 polymorph, was first reported towards the end of 2019 by Vinogradov *et al*. [55]. Bo χ_6 polymorph formed as B atoms were deposited onto Ir(111) during the MBE evaporation of a boron rod of high purity. The substrate was heated in the temperature interval 300 - 600 °C during B deposition. It is worth mentioning that this polymorph was experimentally realised as a new phase of Bo much earlier during the cooldown of Ir(111) after dissolving hBN islands grown on the same substrate- by exposing it to borazine vapour [77, 78], however, the reported Bo coverages were rather low. Based on LEED and high-resolution STM measurements, the proposed unit cell of χ_6 polymorph shown in Fig. 1.8 contains 25 B atoms and 5 atomic vacancies (*i.e.* HHs) [55] rendering it one of the largest experimentally realised Bo unit cells - in comparison with the unit cells of other Bo polymorphs realised so far. The characteristic HH density parameter is $\eta = 1/6$. Theoretical calculations show that Ir supported Bo χ_6 polymorph exhibits a smaller DOS at the Fermi level than its analogous freestanding sheet, however, metallicity has been predicted for both cases [55].

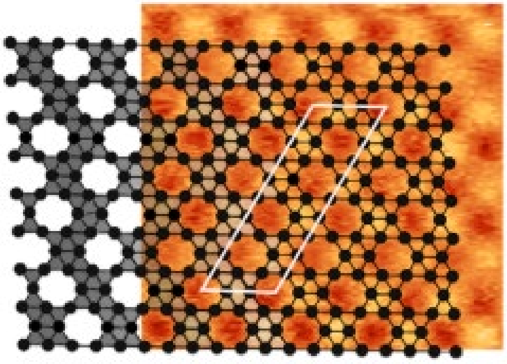

Figure 1.8 The proposed model for Bo $\chi_6$unit cell imposed on an STM image. The filled black circles are boron atoms. Adopted from [55].

The total charge transfer between Bo-sheet and the Ir substrate, based on the reported Bader charge analysis, was found to be small: approximately two electrons per Bo unit cell are donated to Ir surface. The χ_6 polymorph intercalation with gold (Au) atoms proved its robustness: Au atoms could lift off the Bo-sheet without breaking it apart [55].

In an alternative synthesis approach, Omambac and co-workers reported the epitaxial growth of single-phase micrometre-sized Bo on Ir(111) using borazine as a precursor via the segregation-enhanced mechanism [48], the details of which are elaborated on in Section 3.1. Furthermore, Cuxart and co-workers reported the growth of Bo χ_6 polymorph on Ir from diborane [47]. They also managed to produce lateral and vertical heterostructures of Bo and hBN from two precursors: borazine and diborane. The findings highlight the importance of using high-purity precursors to ensure the selective deposition of single phases and pave away for the *in-situ* growth of heterostructures and for safeguarding Bo from oxidation.

1.4 Objectives

The first aim of the research in this thesis is to fabricate extended, high-quality Bo χ_6 polymorph samples on Ir(111), with uniform thickness and homogeneous structure using the segregation-enhanced epitaxial growth. Borazine ($B_3N_3H_6$) is to be used as a precursor, instead of the widely-used method of evaporation of a boron rod of high purity, in order to realise a few-millimetre continuous Bo coverage. The main drawback of the boron source evaporation, often used by other research groups, is that the grown samples are often inhomogeneous and likely to contain 3D boron clusters.

A high and homogeneous Bo coverage is a crucial step for the characterisation of the pristine sample using high-resolution surface-area-averaging techniques of surface science. These include methods such as XPS and ARPES for the sake of investigating the chemical composition, stability, binding to the substrate and electronic band structure of the system. Also, as borophenes are reactive and prone to oxidation, ageing of a freshly grown pristine Bo/Ir(111) is to be further investigated in both UHV environment and ambient conditions via XPS and STM/STS techniques to examine its retrievability after ageing.

Considering the potential of Bo as an electrode material due to the predicted high storage capacity, the Bo electronic structure will be manipulated by decorating the Bo/ Ir system with a charge donor such as Li atoms. Li (Z = 3; $1s^2 2s^1$), characterised by its low ionization potential *i.e.* high reactivity, easily donates its lone valence electron and can effectively induce charge rearrangement in epitaxial Bo systems.

2 Experimental methods

2.1 Low-energy electron diffraction (LEED)

Low energy electron diffraction is a technique employed to probe the crystal structure of surface and subsurface layers of atoms of a given specimen using electrons in the 20-500 eV energy range. Only the first few atomic layers contribute to the diffraction due to the short mean free path of electrons inside a crystal. The electron gun (e-gun) emits electrons impinging on the sample surface which are backscattered towards the fluorescent screen (as shown by the arrows in Fig. 2.1). The backscattered electrons constitute diffraction spots (see below for the corresponding mathematical description) which are then displayed on a fluorescent screen and can be imaged in a digital format using a CCD camera. The geometry of the diffraction pattern reveals the arrangement of surface atoms and any adsorbates while the spot intensities may provide information on the adsorbate coverage density. LEED is usually applied in the backscattering geometry near normal incidence. A basic LEED display system is shown in Fig. 2.1 [79].

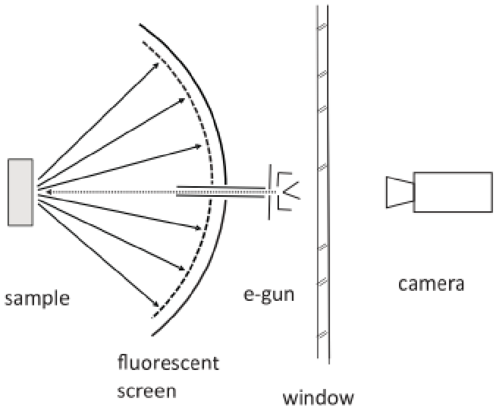

Figure 2.1 Schematic of basic LEED setup. Adopted from [79].

LEED experiments are conducted in a UHV chamber where a well-defined crystalline surface of the specimen under investigation elastically scatters the electrons yielding a characteristic diffraction pattern provided that $\lambda_0 \sim a$ where $\lambda_0$is the wavelength of the incident electron and a is the interatomic spacing of the investigated specimen. The energies of incident and diffracted electron beams are conserved *i.e.* $|\boldsymbol{k}_0| = |\boldsymbol{k}|$ where $\boldsymbol{k}_0$ and $\boldsymbol{k}$ are the wavevectors of incident and scattered beams, respectively. The wavevector absolute value and wavelength of an electron are interrelated through the following relations:

$$|\boldsymbol{k}_0| = \frac{2\pi}{\lambda_0} \qquad |\boldsymbol{k}| = \frac{2\pi}{\lambda}$$

The 2D reciprocal lattice of the surface may be represented as an array of rods extending from the surface lattice points as illustrated in Fig. 2.2a-b in a construction known as Ewald sphere. The distance between diffraction spots (green points where the rods cross the sphere) is inversely proportional to a. The von Laue condition for constructive interference states that:

$$\mathbf{G}_{hk} = \boldsymbol{k} - \boldsymbol{k}_0 = h\boldsymbol{a}^* + k\boldsymbol{b}^*$$

$\mathbf{G}_{hk}$ is a vector of the reciprocal lattice, h and k indicate the crystal Miller indices in reciprocal space, and $\mathbf{a}^*$ and $\mathbf{b}^*$are the reciprocal lattice vectors. The Ewald sphere (Fig. 2.2) visualises the effect of von Laue condition where green spots correspond to the points of constructive interference formed by the diffracted electron waves. The hemispherical fluorescent screen of the LEED apparatus (Fig. 2.1) corresponds to the upper half of the Ewald sphere. The incident wavevector $\boldsymbol{k}_\mathbf{0}$ lies parallel to the reciprocal lattice rods (LEED is performed using a beam of electrons impinging normal to the surface). The vectors $\mathbf{a}^*$ and $\mathbf{b}^*$are related to the real-space lattice vectors $\mathbf{a}$ and $\mathbf{b}$ by the following relations:

$$\mathbf{a}^* = 2\pi \frac{\mathbf{b} \times \hat{\boldsymbol{n}}}{|\mathbf{a} \times \mathbf{b}|} \qquad \mathbf{b}^* = 2\pi \frac{\mathbf{a} \times \hat{\boldsymbol{n}}}{|\mathbf{a} \times \mathbf{b}|}$$

where $\hat{\boldsymbol{n}}$ is the surface normal unit vector [79]. Thus, the resultant LEED pattern depicts reciprocal space.

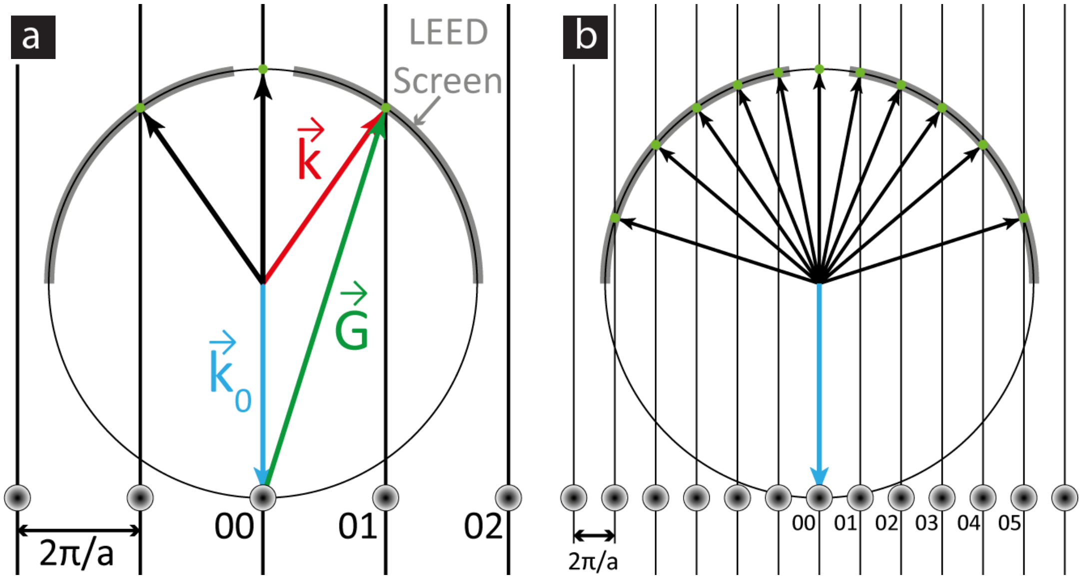

Figure 2.2 Construction of Ewald sphere. (a) Diffraction spots (green circles) form on the fluorescent LEED screen at points of constructive interference. The spots (rods) are numbered by their *hk* values. (b) More LEED spots are visible as the radius of Ewald sphere (and thus the $|\boldsymbol{k}_0|$ value) increases at higher kinetic energies of the impinging electrons [80].

2.2 Low-energy electron microscopy (LEEM)

Low-energy electron microscopy is a technique which uses elastically backscattered electrons to image a crystalline surface. High resolution imaging is achievable by LEEM (as low as ~ 5 nm), where the real-space image (LEEM mode in Fig. 2.3a) and diffracted intensities (LEED mode in Fig. 2.3b) may be also acquired by selecting different operation modes of the instrument [81]. In LEEM, an electron beam of low energy (below 100 eV) strikes the sample, some electrons are reflected back, while others may be scattered or absorbed. The reflected electrons carry information about the surface structure. The intensity of the detected electrons depends on the local surface potential and topography. Therefore, LEEM may capture variations in surface topography such as steps, terraces, domain stacking order or defects [81]. LEEM also enables the measurement of diffraction intensities from tiny areas and individual domains (so-called micro-LEED or μ-LEED), which is usually unattainable with conventional LEED setups. Hence, it can also provide a deep insight into *in-situ* crystal growth. Another advantage of LEEM is its capability of real-time imaging by capturing dynamic processes occurring on surfaces in real time, such as phase transitions, adsorption, and desorption events. The ability to observe these processes relies on the rapid acquisition of reflected electron signals, which can be correlated with time-dependent changes in the surface structure [79]. A distinctive intensity-voltage spectrum (LEEM I-V curve) may also be recorded for each pixel of the detector camera where the kinetic energy of the incident electrons is varied by tuning the start voltage applied to the sample. LEEM I-V spectrum provides energy-dependent reflectivity of the sample surface (as shown in Fig. 3.7) where the resultant contrast basically comes from the atomic structure and electronic band structure of the surface. Thus, LEEM I-V curves may be used as a fingerprint for distinctive surface phases [79, 81].

The LEEM images and XPS spectra shown in Chapter 3 of the thesis were all recorded in Spectroscopic PhotoEmission and Low Energy Electron Microscope (SPELEEM) (sketches of its operation modes are displayed in Fig. 2.3) at Elettra synchrotron Nanospectroscopy beamline shown in Fig. 2.4. In such a setup, spectroscopic operation may be realised either in real space photoemission electron microscopy (PEEM), diffraction imaging mode (microprobe LEED, microprobe photoelectron diffraction, microprobe ARPES), or spectroscopy mode (microprobe-XPS) [81]. Thus, the sample in the SPELEEM may be probed either with low energy electrons (0 – 750 eV) generated by a source such as LaB_6, or employing monochromatized soft X-rays (40 – 1000 eV). During real space imaging, contrast apertures of 10, 30, or 100 µm (Fig. 2.3a) were employed in order to adjust the lateral resolution of the microscope by limiting its angular acceptance. The lateral resolution in LEEM mode is ~ 10 nm. LEEM images are recorded in bright-field imaging mode when only specular diffraction spots are utilized for the formation of the real space sample image. The hemispherical energy filter and contrast aperture may be used simultaneously (Figs. 2.3a, c) in order to select a well-defined photoemission angle and kinetic energy, to enable real space PEEM imaging of the corresponding features in the electronic structure. The measurements may be confined to micron-sized surface areas in the microprobe diffraction and spectroscopy operation modes by using the field limiting aperture (Figs. 2.3b, c), thus allowing micro-XPS or micro-ARPES measurements. The reader is advised to refer to references [81, 82] for a thorough treatment of the subject.

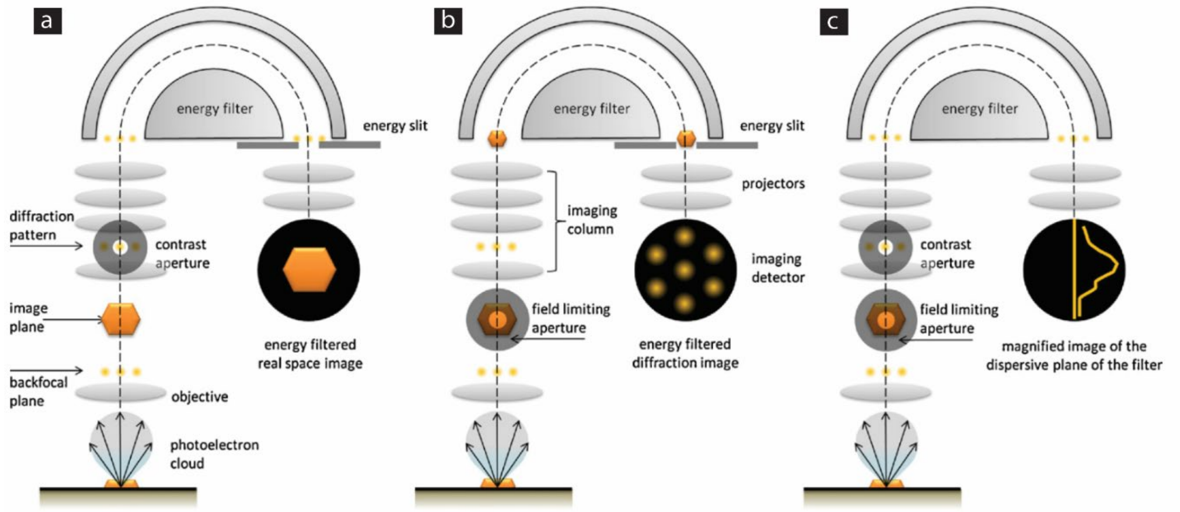

Figure 2.3 Setup of electron optics in three operation modes of SPELEEM: (a) imaging (LEEM or PEEM) mode. (b) diffraction (LEED) mode. (c) micro-spectroscopy mode. SPELEEM is displayed below in Fig. 2.4. Adopted from [81].

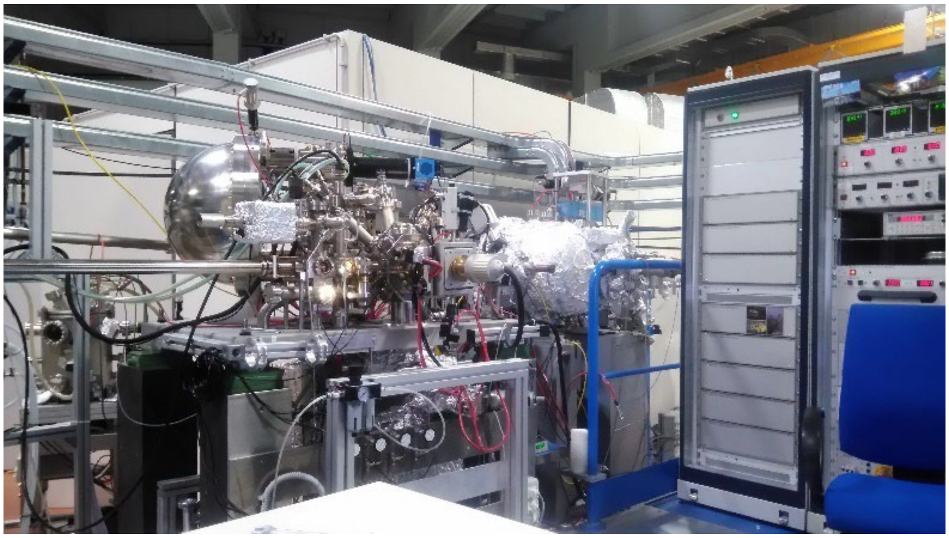

Figure 2.4 Nanospectroscopy beamline in Elettra synchrotron. The shown apparatus enables recording LEED, LEEM, PEEM, XPS and ARPES data.

2.3 Scanning tunnelling microscopy (STM)

Scanning Tunnelling Microscopy (STM) is an experimental technique employed for simultaneous analysis of the structural and electronic characteristics of the conductive surfaces. The microscope was invented by Heinrich Rohrer and Gerd Binning in 1981 to map surface topography with atomic resolution using quantum tunnelling effect [83]. Therefore, the invention sparked a revolution in surface characterisation in the field of materials science. The sample surface in an STM is scanned by an extremely sharp metallic tip in a raster pattern as a small bias (tunnelling) voltage V_{b} (in the range from a few mV to a few V) is applied between the tip and the sample. The STM may be operated in two modes: the *constant-height* mode where the tip position is kept unchanged along z axis while monitoring the tunnelling current I_{t}; and the *constant-current* mode where I_{t} is kept constant while changing the z position of the tip. I_{t} is then detected as the tip is moved across the sample surface (Fig. 2.5). As the sample-tip separation z, *i.e.* the tunnelling barrier width, increases, the tunnelling current decays exponentially:

$$I_{\mathrm{t}} \sim V_{\mathrm{b}}\, e^{-2\kappa z} \quad \text{where} \quad \kappa = \frac{\sqrt{m_e(\phi_t + \phi_s + eV_{\mathrm{b}})}}{\hbar}$$

The decay constant κ is related to the work functions of the tip $\phi_{\boldsymbol{t}}$ and sample $\phi_{\boldsymbol{s}}$. The energy of electrons encountering the lowest potential barrier is given by eV_{b}. The symbols m_e and $\hbar$ correspond to the electron effective mass and reduced Planck constant, respectively. Since $\kappa \sim 1$ Å^{-1} for most metals, I_{t} decays by an order of magnitude for z ~ 1 Å, therefore the topmost atom at the tip apex contributes significantly to the tunnelling curent. For a tiny separation between the sample and the tip (z < 1 Å), their respective wavefunctions overlap and the electrons may tunnel through the vacuum barrier between them. When a small bias (tunnelling) voltage V_{b} is applied, one obtains I_{t} from the occupied states of one conductor (either the tip or the sample) to the unoccupied states of the other [84].

Scanning tunnelling spectroscopy (STS) is performed at a bias voltage between the tip and sample to estimate the local electronic density of states (LDOS) of the sample ρ_s. The quality of an STM image depends on ρ_s: the higher the value of ρ_s, the higher the number of electronic states contributing to I_{t}. STM/STS measurements are highly sensitive to the thermal drift of the sample induced by temperature variations, therefore cryogenic temperature is necessary for accurate measurements. For a tip made of Pt-Ir alloy (Fig. 2.6, inset), its LDOS (ρ_t) is rather flat, therefore we have $\rho_t\ (\epsilon - eV_\mathrm{b}) \approx \rho_t(0)$, *i.e.* ρ_t may be assumed to be constant. Also, assuming that there is a minimal overlap between the wavefunctions of the tip and sample leading to a constant matrix element $|M_{st}|^2$, the tunnelling current for small tunnelling voltages may be approximated by the following integral [84]:

$$I_\mathrm{t}(z, V) \approx \frac{4\pi e}{\hbar} \rho_t(0)\ |M_{st}|^2 \int_0^{eV_\mathrm{b}} \rho_s(\epsilon)\, d\epsilon$$

The derivative of I_t with respect to the applied voltage is: $\frac{dI}{dV} \sim \rho_s(eV_\mathrm{b})$, therefore measuring $\frac{dI}{dV}$ is measuring the density of electronic states of the sample. STS is employed to measure $\frac{dI}{dV}$ point spectra in relation to the bias voltage or to measure STS maps. In the latter, the tip scans the surface at a fixed bias voltage to measure $\frac{dI}{dV}$ signal for the preset bias voltage along with surface topography [84].

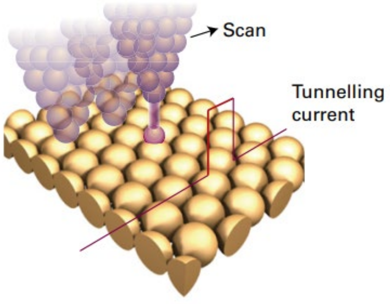

Figure 2.5 Schematic of an STM tip above a metallic surface containing an adsorbate. The tunnelling current between the surface and the tip is highly sensitive to the distance of the tip above the surface. Adopted from reference [85].

STM/STS measurements within this thesis were performed in: (i) home-built Athene STM setup in Cologne, Germany. Single-point I/V spectra, acquired in 128 × 128-point grids, were numerically differentiated to obtain $\mathrm{d}I/\mathrm{d}V$ curves. All data were recorded at room temperature $T \approx 300$ K. The processing of STM images (background subtraction and contrast enhancement) was performed via WSxM software [86]. (ii) low-temperature STM setup (Omicron LT-STM) in the Faculty of Science and Technology, University of Twente, Enschede, the Netherlands (Refer to Fig. 2.6). In this setup the data were recorded at $T \approx 77.5$ K. Data processing was done with Gwyddion software.

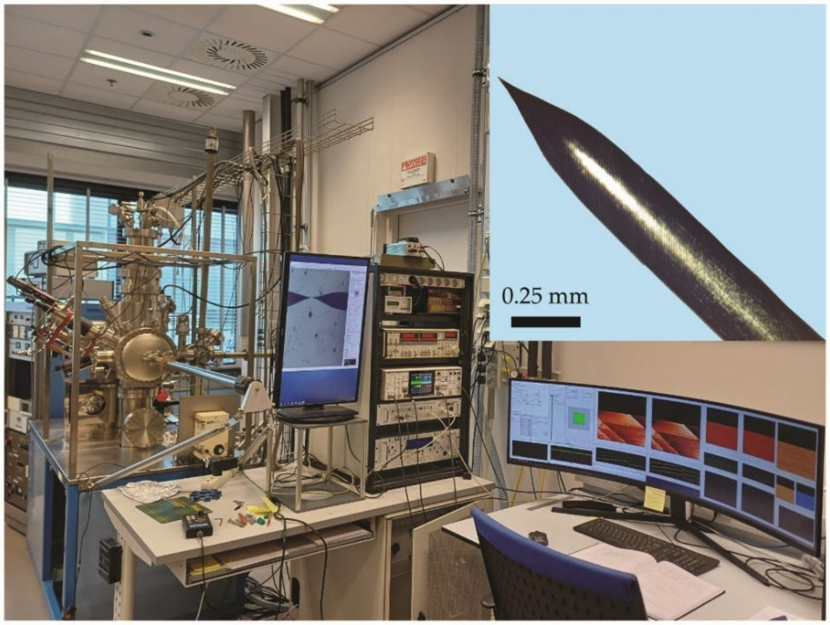

Figure 2.6 Omicron LT-STM setup. The inset shows a freshly chemically-etched Ir-Pt tip before mounting it onto the tip-holder.

2.4 Photoemission spectroscopy (ARPES and XPS)

The photoemission spectroscopy (PES) is based on the photoelectric effect; therefore, it may be called the photon-in, electron-out technique. Photoemission occurs only if the energy of the incident (probing) photon $h\nu$ exceeds the work function of the material (sample) Φ, which is the minimum energy required for an electron at the Fermi level E_{F} to escape into the vacuum, *i.e.* above the vacuum level E_{v}, therefore: $\Phi = E_{\mathrm{v}} - E_{\mathrm{F}}$ (refer to the schematics of Fig. 2.7). The photon energy of incident monochromatic light is a crucial parameter in PES, it may vary from VUV (6 - 124 eV) to hard X- rays (> 5 keV) [87].

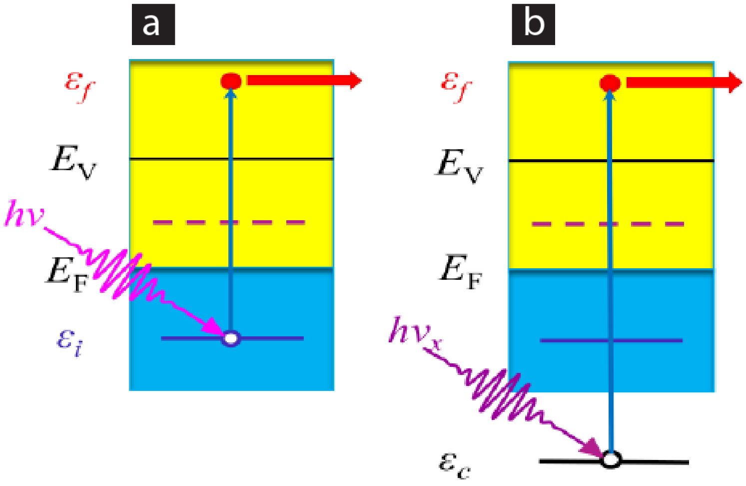

Figure 2.7 Basic sketches of two PES scenarios. One photon, illustrated as a pulse of finite duration, excites an electron from its initial (ground) state ε_i from the a) valence band (blue shaded region) - ARPES scenario or b) core level ε_c state lying closer to the element nucleus - XPS scenario- to a final state energy ε_f above the vacuum energy level E_V. The purple dashed horizontal line indicates the bottom of the conduction band. Adopted from [88].

In angle-resolved photoemission spectroscopy (ARPES) the photoelectrons ejected from the valence band of either a metallic or semiconducting crystal are collected, within a certain angular range of emission with respect to the sample normal, along the optical axis of the cylindrical lens of the electron spectrometer - the hemispherical analyser in our setup (Fig. 2.8). The intensity distribution of the photoelectrons as a function of kinetic energy E_k and the photoemission angles (θ, φ) is recorded by the spectrometer $I(E_k, \theta, \varphi)$.

The final photoelectron spectrum directly reflects the electronic structure $E(\mathrm{k})$, namely, the electron binding energy E_B versus its in-plane crystal momentum $k_{\parallel}$ in reciprocal space. The conversions $(\theta, \varphi) \to (k_x, k_y)$ - the components of $k_{\parallel}$ since $k_{\parallel} = \sqrt{k_x^2 + k_y^2}$ - and $E_k \to E_B$ are possible through the following conservation laws:

$$k_x = \frac{\sqrt{2m_e E_k}}{\hbar} \sin\theta \cos\varphi$$

$$k_y = \frac{\sqrt{2m_e E_k}}{\hbar} \sin\theta \sin\varphi$$

$$\mathrm{p} = \hbar k_{\parallel} = \sqrt{2m_e E_k}\sin\theta$$

$$E_{\mathrm{B}} = h\nu - E_k - \Phi_s$$

Where: p and m_e are the momentum and mass of the photoelectron, respectively; and Φ_s is the work function of the spectrometer. The electronic structure and photoelectron spectrum are interrelated due to the conservation of $k_{\parallel}$ components (k_x, k_y), arising from the crystal translational symmetry along x and y directions, and energy conservation during the photoemission process [89]. The measured spectra of photoelectrons, their energies and momenta distributions, convey information on the energetics and occupied band density of states (DOS) of the system.

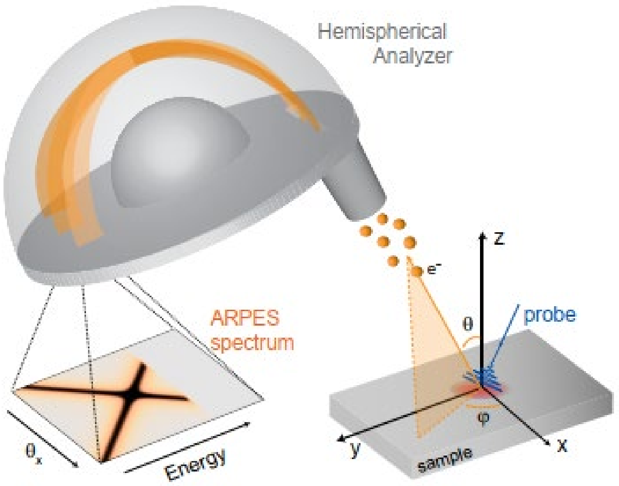

Figure 2.8 Schematic of the basic ARPES setup. The sample excitement with photons (illustrated as a blue pulse of finite duration), ranging in energy from the UV to XUV, leads to photoemission of electrons from the valence band of the sample. A fraction of the photoelectrons is then collected by the hemispherical analyser which registers them by both kinetic energy E_k and photoemission angles (θ, φ). Adopted from [89].

The dependence of the inelastic mean free path (IMFP) of a photoelectron on its E_k is illustrated by the universal curve (Fig. 2.9). The curve shows that for incident photon energies above 20 eV in the VUV region, the IMFP is short (< 0.6 nm) which indicates that ARPES is a highly sensitive surface technique, therefore a significant part of the total ARPES signal originates from the topmost surface layer of the sample. The surface sensitivity is also mandatory when probing surface states of crystals such as Ir(111) as will be shown in Section 4.2.

In X-ray Photoelectron Spectroscopy (XPS) (Fig. 2.7b) the photoelectrons are excited from the core levels that lie close to the nucleus of the probed atom, but their emission angle is disregarded, *i.e.* electron momentum information is not recorded. The final spectrum is a (I-E_B) curve where the intensity (~ number of collected photoelectrons) is plotted against the binding energy. XPS is used to identify the atomic composition and oxidation state(s) of the specimen being examined.

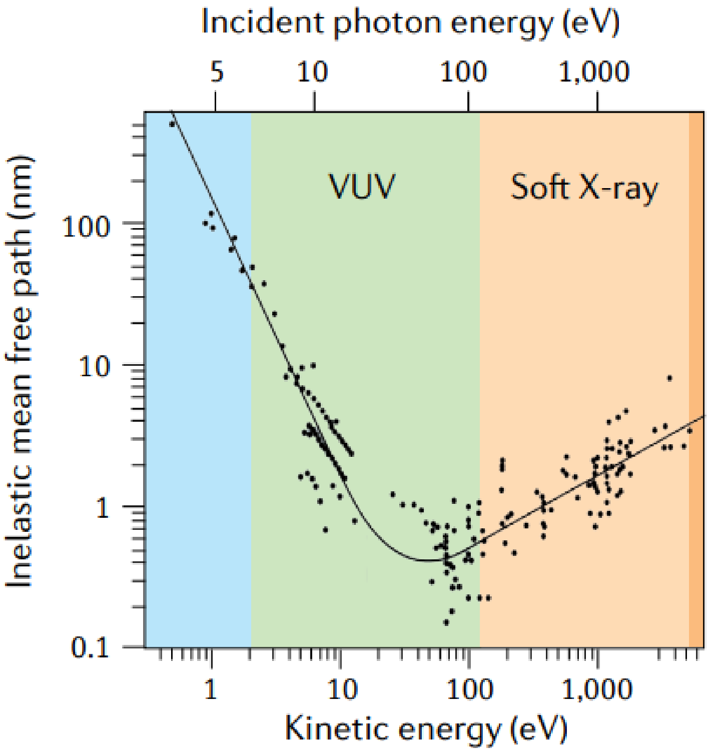

Figure 2.9 Universal curve, showing dependence of IMFP on the kinetic energy of the photoelectrons. The energy of the probing photon in PES ranges from VUV (~ 6 - 124 eV) to hard X- rays (> 5 keV). Adopted from [89].

The synchrotron-ARPES based data included in Sections 4.1, 4.2, 5.1 and 5.2 were acquired *in situ* in two setups: UARPES (currently URANOS) beamline of the Solaris synchrotron (Krakow, Poland) and the VUV-Photoemission beamline of the Elettra synchrotron (Trieste, Italy). At UARPES, data were recorded *in situ*, employing the Scienta DA30L electron analyser, at room temperature. The linearly polarized light illuminated the sample at 44° with respect to the analyser axis, with the light spot diameter on the surface of ~ 0.5 mm. 4D data sets (k_x, k_y, E, I) were acquired by exploiting the full acceptance cone of the analyser without moving the sample.

At VUV-Photoemission beamline, ARPES and XPS data were recorded under normal emission at room temperature. The base pressure of the experimental chamber was 2×10^{-10} mbar. The Scienta R4000 electron analyser, employed for data acquisition, had the entrance slit oriented parallel to the scattering plane of the experiment. Linearly polarized light illuminated the sample at 45° with respect to the axis of the analyser, with a light spot diameter on the sample surface of ~0.5 mm. 4D ARPES data sets (k_x, k_y, E, I) for the sample were acquired by rotating the sample azimuthally and by applying symmetry operations to the data. All the XPS and ARPES data presented in Chapter 4 were recorded *in situ*, in order to avoid artifacts resulting from air exposure or breaking the vacuum.

The XPS spectra shown in Section 5.1.2 were recorded at room temperature via SPECS XPS apparatus of the Faculty of Physics, University of Rijeka. A source of monochromatic X-rays was an Al anode, characterised by a photon energy of 1486.74 eV Al K_α line The angle of the incident X-ray beam was 45° and the spot size diameter of the beam was ~ 1-2 mm. For data acquisition a PHOIBOS 100 hemispherical electrostatic energy analyser with a 5-channel detector was used with the pass energy values of 10 and 20 eV. The overall energy resolution was ≈ 0.65 eV. The typical pressure in the UHV chamber in the course of the XPS analysis was in the 10^{-9} mbar range. The binding energies of all core photoemission spectra were referenced to the Fermi level. B 1*s* XPS peaks were deconvoluted by a product of Gaussian-Lorentzian functions of the ratio 0.8 and peak width (FWHM) of 0.4 eV. The background of all acquired spectra was subtracted using Shirley polynomial.

For Li deposition experiments, presented in Section 5.2, a rough estimate of the effective number of atomic layers - in our case: the layers of Ir atoms in a single-crystal contributing to the XPS signal- was determined by assuming that all Ir atoms in the topmost layer of the Ir(111) crystal contribute to the XPS signal while layers underneath contribute exponentially less. The top four layers of Ir atoms, corresponding to the sum of four exponential functions: $e^{0}+e^{-d/\lambda}+e^{-2d/\lambda}+e^{-3d/\lambda}$, are considered, where d is the interlayer separation between Ir atoms and λ is IMFP of Ir at measured kinetic energies of the photoelectrons. The Li coverage θ_{Li} was estimated from the following approximation:

$$\theta_{Li}=\frac{I_{Li}}{I_{Ir}}=\frac{I_{Li}}{\left(I_{7/2}+I_{5/2}\right)_{Ir}}$$

$$\left(I_{7/2}+I_{5/2}\right)_{Ir}=\frac{\sigma_{Li}}{\sigma_{Ir}}\left(\frac{1}{e^{0}+e^{-d/\lambda}+e^{-2d/\lambda}+e^{-3d/\lambda}}\right)\left(\frac{1}{E_k}\right)_{Li}\left[(I\times E_k)_{7/2}+(I\times E_k)_{5/2}\right]_{Ir}$$

where I_{Li}, I_{Ir} are the intensities of spectral emission (*i.e.* the area under the respective XPS peaks) of Li and Ir, respectively. Since 4*f* orbital of Ir exhibits spin-orbit splitting into the components 4*f*$_{7/2}$ and 4*f*$_{5/2}$, therefore $\left(I_{7/2}+I_{5/2}\right)_{Ir}$ is the summation of the contributions of each splitting component to I_{Ir}. E_k is the kinetic energy of photoelectrons. σ_{Li} and σ_{Ir} are photo-ionization cross-sections of Li and Ir, respectively. All the XPS peaks included in this work were deconvoluted by a product of Gaussian and Lorentzian functions. The background of all acquired spectra was subtracted using Shirley polynomial.

3 Sample synthesis

The main results given in Section 3.1 were published in the following paper: Borna Radatović, Valentino Jadriško, Sherif Kamal, Marko Kralj, Dino Novko, Nataša Vujičić and Marin Petrović, *Macroscopic Single-Phase Monolayer Borophene on Arbitrary Substrates.* ACS Applied Materials & Interfaces, 14, 21727−21737 (2022) [37].

3.1 Borophene growth

Due to the usage of several in situ experimental characterization methods, Bo samples on an Ir(111) single crystal were grown in five different UHV systems (see Table 3.1 for an overview). We have employed the same Bo preparation protocol with slight variations to compensate for different geometries of UHV chambers. For cleaning the Ir substrate, the following steps were pursued: sputtering with argon or xenon gas, annealing in oxygen and annealing without oxygen (consult Table 3.1 for the parameter values). Sample heating was achieved by electron bombardment (e-beam heating) from the back side, where electrons thermally emitted from a W filament were accelerated with high voltages towards the Ir crystal. The surface quality was monitored utilizing the following indicators: sharp LEED spots of Ir, the occurrence of Ir surface states around Γ or K- point and absence of contamination-related peaks in XPS spectra (whenever relevant).

The underlying mechanism of Bo synthesis is boron dissolution-segregation route [48, 37, 90] (see the schematic in Fig. 3.1) where the heated (T ~ 1200 °C) Ir surface is exposed to borazine ($B_3N_3H_6$) vapour at $p \sim 1 \times 10^{-8} - 5 \times 10^{-7}$ mbar. The sample is heated via e-beam bombardment at heating rates ~15 − 20 °C/s. Once borazine comes in contact with the heated catalytic surface of Ir, the following thermal decomposition takes place where the borazine molecule loses all its H atoms at once [90]:

$$B_3N_3H_6 \rightarrow B_3N_3 + 3H_2\uparrow \qquad T > 700\ ^\circ\mathrm{C}$$

Table 3.1 Experimental parameters used for the preparation of borophene in different UHV setups.

Setup	Ir sputtering	Ir annealing	Borazine dosing	Cooling rate
Nanospectroscopy beamline (Elettra)	Ar^+ at 1.5 keV	1000 °C in O_2 1230 °C without O_2	1×10^{-8} mbar at 1100 °C	3 – 10 °C/s
VUV-Photoemission beamline (Elettra)	Ar^+ at 2.5 keV	800 °C in O_2, 1100 °C without O_2	5×10^{-7} mbar at 1100 °C	3 – 10 °C/s
Surface Physics Lab (Institute of Physics)	Ar^+ at 1.5 keV	800 - 1000 °C in O_2 1200°C without O_2	3×10^{-8} mbar at 1200 °C	3 – 10 °C/s
UARPES beamline (Solaris)	Ar^+ at 1.5 keV	850 °C in O_2 1100 °C without O_2	3×10^{-8} mbar at 1070 °C	3 – 10 °C/s
STM/STS setup (University of Cologne)	Xe^+ at 2 keV	1250 °C without O_2	1×10^{-8} mbar at 990 °C	3 – 10 °C/s

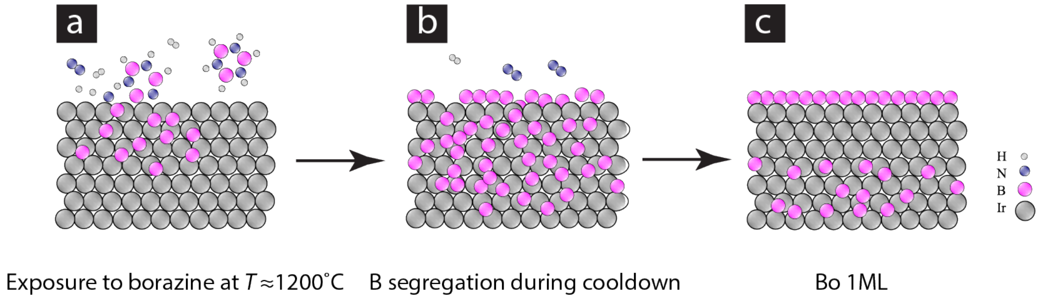

Exposure to borazine at $T \approx 1200$˚C B segregation during cooldown Bo 1ML

Figure 3.1 Mechanism of segregation-enhanced epitaxial growth of Bo on Ir(111). (a) As the precursor (borazine), is dosed onto the heated surface of Ir crystal, boron atoms dissolve into the bulk. (b) As the sample is cooled down, B atoms begin to segregate towards the surface and self-assemble into Bo sheet. (c) A full Bo monolayer forms on the surface after several dissolution-segregation cycles.

The resultant hexagonal B_3N_3 molecule conceptually consists of a diatomic building unit *i.e.* a BN dimer, bound to another pair of BN dimers [90]. At T > 1000 °C, the BN dimers dissociate with high probability into its constituent B and N atoms as follows:

$$2BN \rightarrow 2B + N_2\uparrow$$

As nitrogen desorbs, boron atoms dissolve into the substrate and they segregate back to the surface upon sample cooling, due to the reduction of B solubility in Ir, forming Bo. For a well-comprehensive treatment of the growth kinetics, the reader is advised to refer to the study conducted by Omambac *et al.*[90]. The sample cooling to room temperature was performed by gradually turning off the e-beam heating (with cooling rates ~ 3 − 10 °C/s), no additional active cooling was employed. This protocol is repeated several times to obtain a sample of a relatively high coverage exceeding 0.8 monolayer (ML) as evidenced by XPS data given in Section 4.1. Initially, the Bo coverage θ_{Bo} was studied as a function of the number of growth dissolution-segregation cycles (N_c) via LEED. The LEED patterns (a-c) displayed in Fig. 3.2 reveal the increase in Bo coverage after 5th, 7th and 11th dissolution-segregation cycles. The six LEED pattern line profiles shown in Fig. 3.3 were extracted across the first order Ir diffraction spot and its first neighbouring Bo spot at several N_c. For $N_c < 4$, Bo spots were below the detection limit of our LEED apparatus, indicating a rather low θ_{Bo}. The intensity of the Bo spot rises continuously as N_c increases, indicating a significant increase of θ_{Bo}. Whereas intensity of the Ir spot diminishes, signifying the formation of an overlayer on top of the Ir surface. Neither additional increase of Bo nor decrease of Ir diffraction spot intensities was observed at $N_c > 12$ indicating full Bo layer completion. The LEED pattern of 1 ML Bo/Ir(111), shown in the inset of Fig. 3.3, displays a characteristic sharp (6×2) pattern with three rotational domains [78, 48]. Vinogradov *et al.*, as it was mentioned in Subsection 1.3.3., assigned χ_6 polymorph to such a diffraction pattern after realizing it on Ir(111) using MBE [55]. Similar was done by employing a conventional CVD technique [47].

It should be emphasized that either higher pressure (> 10^{-8} mbar) of the precursor or lower temperature (< 1000 °C) of Ir(111) surface favours the formation of 2D hBN over Bo. Under such thermodynamic conditions most BN dimers, resulting from the thermal decomposition of borazine molecules, do not dissociate into B and N, thus yielding high nucleation density of hBN. It is noteworthy that temperature increase (T > 950 °C) promotes defect creation in hBN islands and initiates Bo formation. At T > 950 °C, hBN islands decay much slower than BN dimers. In other words, two rather different 2D materials, *i.e.* Bo and hBN, may grow from the same molecular precursor depending on how the dosing pressure of the precursor and the substrate temperature are tuned [90] and care must be taken to avoid hBN formation when Bo layers are sought. It is noteworthy that dissolution-segregation growth method rendered high-coverage samples suitable for Bo transfer onto a substrate of choice (Si wafer) [37] thus pushing applicative potential of borophene closer to realisation. Another advantage of this growth method over other methods is avoiding cluster formation either on formed Bo patches or bare regions of the substrate. Examples of non-optimum synthesis, producing samples containing hBN or Bo mixed with various B species, are presented in Section 3.2.

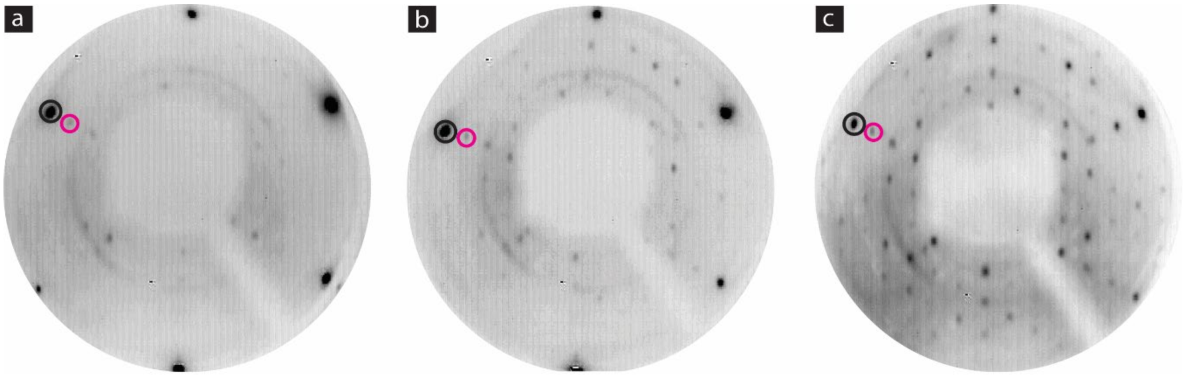

Figure 3.2 LEED patterns (a-c) reveal an increase in Bo coverage after 5th (a), 7th (b) and 11th (c) dissolution-segregation cycles. Black and magenta circles indicate Ir and Bo spots, respectively. The patterns were recorded at 44 eV. Arc-like features visible in all panels are LEED screen inhomogeneities.

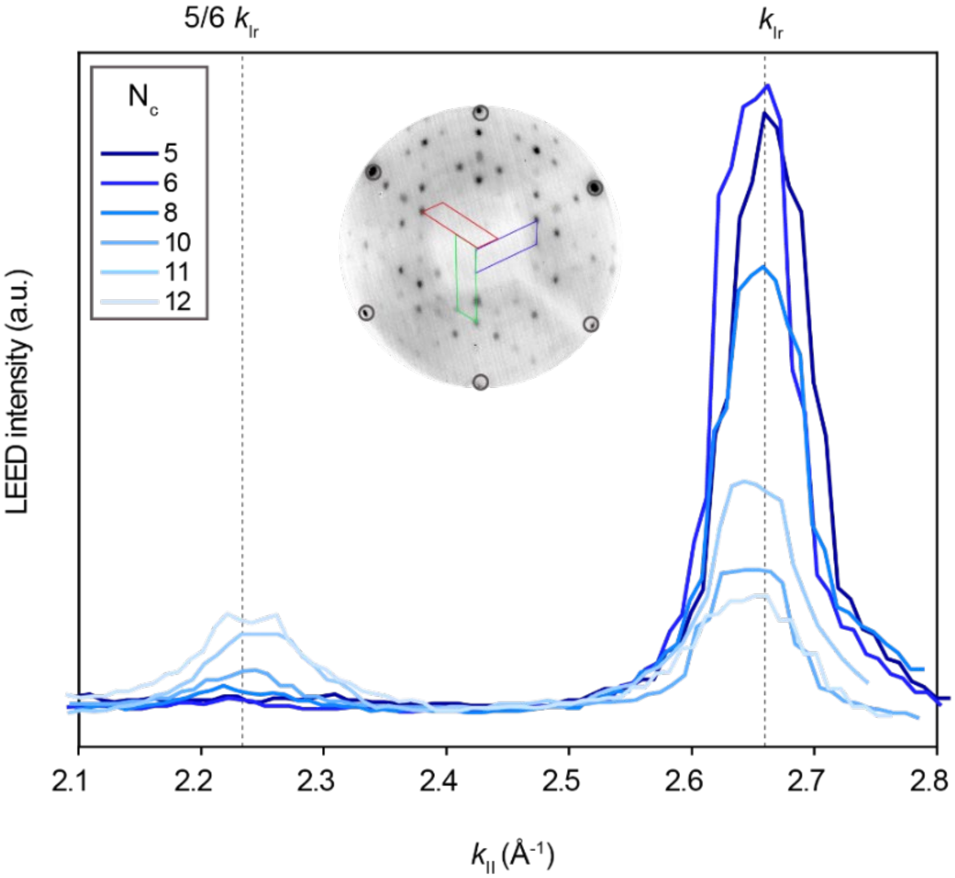

Figure 3.3 A sequence of Ir and Bo diffraction spot profiles extracted from a set of LEED patterns recorded after a given number of dissolution−segregation cycles (N_c). A decrease of Ir spot intensity (at $k_{\mathrm{Ir}} = 2.65$ Å^{-1}) and an increase of Bo spot intensity (at 5/6 $k_{\mathrm{Ir}} = 2.23$ Å^{-1}) as a function of N_c are noticeable. Inverted LEED pattern of a monolayer Bo/Ir(111) recorded at 35 eV after 12th dosing cycle, with the Ir spots encircled in grey, is shown in the inset. The superposition of three 120°-rotated (6 × 2) patterns corresponds to the Bo layer. Each parallelogram corresponds to a Bo unit cell of one orientational domain.

Bright-field LEEM was employed to monitor the formation of Bo on Ir(111) in real time. The sequence of LEEM images recorded within ~15 μm field of view (Fig. 3.4a-n) shows evolution of Bo filling of Ir terraces within 8 minutes of sample cooldown. Prior to cooldown, the Ir crystal was exposed to borazine at 1 × 10^{-8} mbar for 180 s. Panel (a) shows Ir terraces just before B atoms begin to nucleate forming Bo sheets. Panel (b) displays first nucleation of B atoms on one Ir terrace whereas panels (c-e) show further expansion of Bo sheet, covering ~ 50% of the terrace. At a cooling rate of ~ 0.3 °C/s it took about 15 s for one Ir terrace to be almost fully covered with Bo as displayed in panels (a-d).

Bo coverage of the sample region shown in Fig. 3.4, is given as a function of time in Fig. 3.5. It is evident that segregation-driven Bo growth exhibits a step-like mode, consisting of alternating periods of rapid and slow θ_{Bo} increase, rather than the smooth, continuous mode typical of graphene formation onto the same substrate [90]. The latter mode is due to the fact that nucleation of graphene islands takes place on the Ir terraces and at its step edges in contrast to the step-like mode of Bo growth arising from different segregation rates of the B atoms from the bulk of the crystal towards the surface. Each step in the graph (rapid θ_{Bo} increase) corresponds to the emergence of a new Bo nucleation site followed by Ir terrace filling with Bo. It is noticeable that, on the average, the Bo growth rate declines with time, mainly due to the depletion of B atoms from the subsurface Ir regions. The eight minutes during which the sample cooled from 1076 to 922 °C, and with the borazine exposure preceding the cooldown, yielded ~ 0.65 ML Bo coverage.

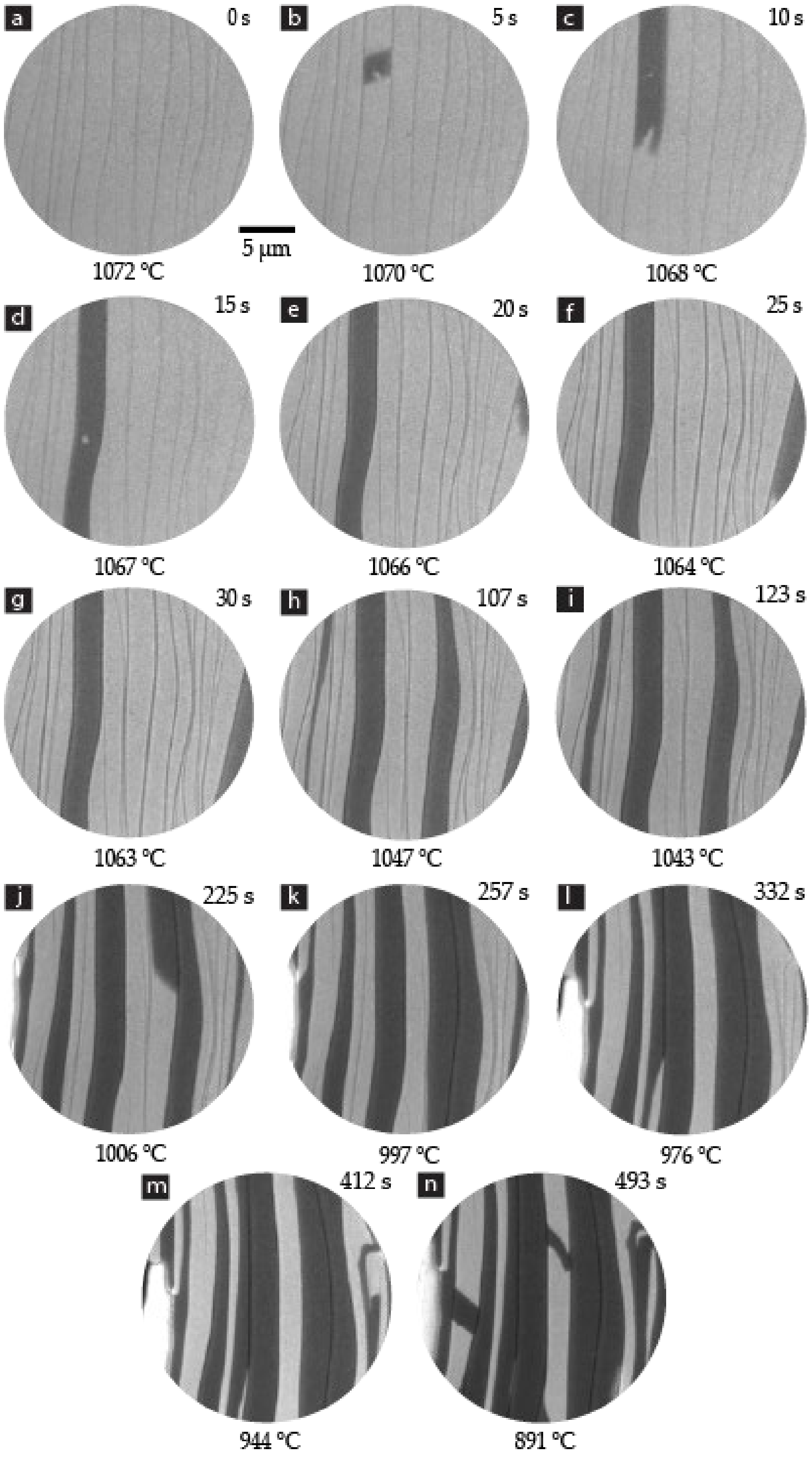

Figure 3.4 LEEM sequence (a-n), acquired at 17 eV and field of view ~15 μm, revealing Bo formation onto Ir terraces as B atoms segregate onto the surface during the sample cooldown. The time interval between (a) and (n) is 8 minutes.

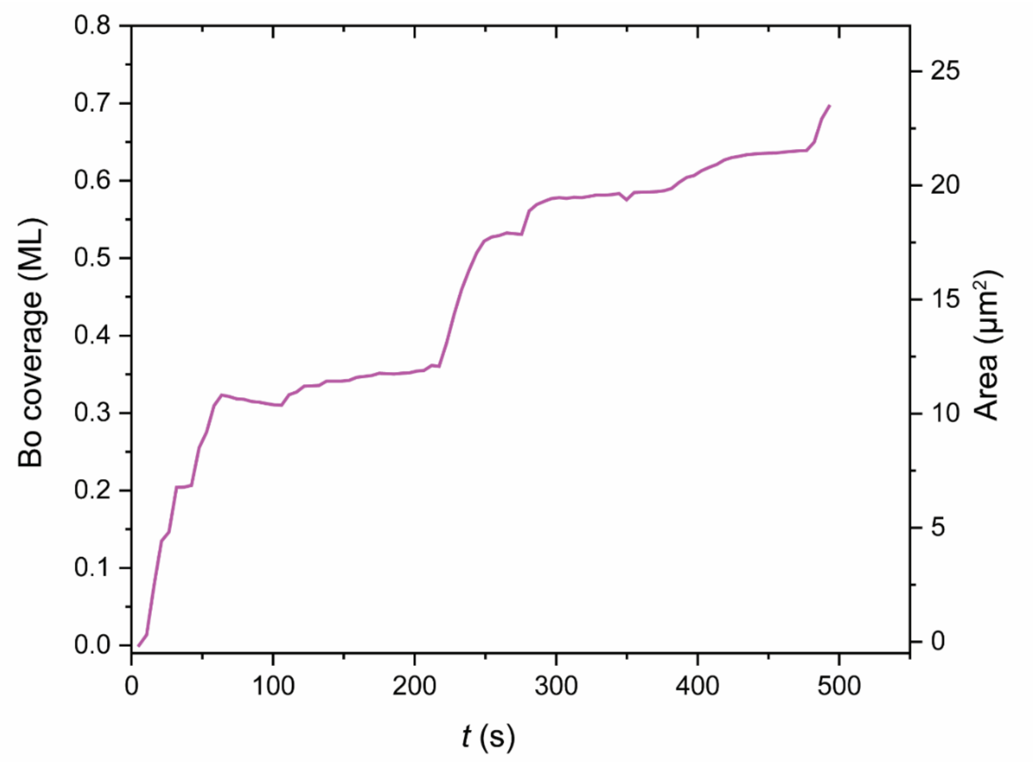

Figure 3.5 Bo coverage (θ_{Bo}) shown as a function of time. The step-like growth trend of the graph reveals the explosive nature of the Bo segregation mechanism. The graph has been extracted from the sequence of LEEM images displayed in Fig. 3.4 acquired within ~15 μm field of view. Apparent decrease of Bo coverage at *t* ~ 100 s is due to the thermal drift during the sample cooling.

3.2 Contaminated and ill-defined borophene samples

In this section, examples are provided of undesired Bo samples, due to the inhomogeneity of their chemical composition. The borazine deposition rate, surface morphology of the substrate, its cleanliness and temperature are crucial factors in the synthesis of borophene (see Section 3.1), and here we showcase typical experimental signatures of non-optimized synthesis protocols. These examples also highlight the possibility of tuning the synthesis procedure to obtain other 2D materials and structures.

The LEED pattern displayed in Fig 3.6a reveals the formation of hBN instead of borophene all over the sample surface due to high borazine pressure ($> 5 \times 10^{-7}$ mbar) whereas the pattern shown in Fig 3.6b reveals Bo mixed with hBN due to the same reason. In a spatially-resolved approach of another Bo synthesis attempt, the regions displayed in LEEM images (Figs 3.7a and 3.8a) reveal different levels of contrast (*i.e.* electron reflectivity) indicating formation of other materials on the Ir surface along with Bo. Fig. 3.7b features the corresponding intensity-voltage (I-V) curves pinpointing four areas marked with four different colours in panel (a) and provide further spectroscopic support of their difference. The magenta circle marks an Ir terrace covered with Bo while the three elongated dark patches, one of which is marked with a grey circle, are uncovered Ir terraces. The two bright triangular islands visible nearby the grey circle are assigned to hBN due to their characteristic shape. The orange and brown circles label the brighter terraces on the left, whose I-V signatures are deviated from that of Bo, are considered to be unwanted contaminations. In the following, their chemical composition will be determined.

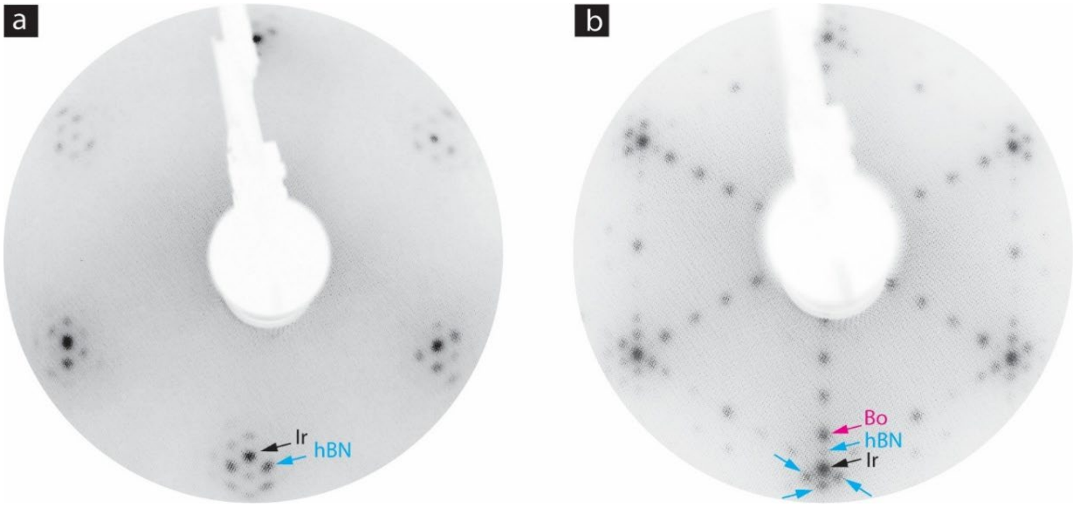

Figure 3.6 LEED patterns of (a) hBN formation on Ir(111) instead of Bo as revealed by the typical moiré pattern due to the lattice mismatch between hBN and Ir unit cells [90]. (b) Bo mixed with hBN sample where the moiré pattern still persists. Both patterns were recorded at 201 eV.

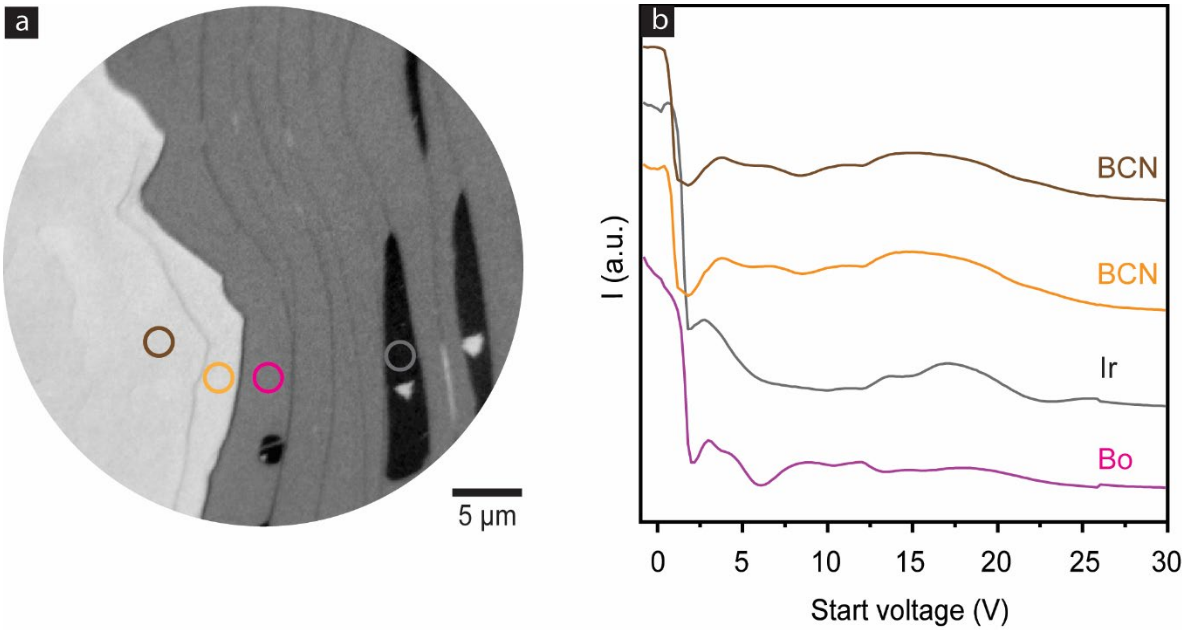

Figure 3.7 LEEM image (a) and the corresponding LEEM I-V curves (b) showing the intensity change of the reflected electrons as a characteristic feature of each of the regions formed on the surface. Aside from Bo covered Ir terraces, such as the one marked with a circle in magenta, the brighter terraces on the left reveal (orange and brown circles) the formation of BCN alloy. The three elongated dark patches, like the one marked with a grey circle, correspond to uncovered Ir terraces. The LEEM image was acquired at 24.14 eV and at 88°C.

Another region of the sample (see Fig. 3.8a), containing material(s) with LEEM-IV signatures resembling the ones shown in Fig. 3.7, was examined via micro-XPS displayed in Fig. 3.8b-c. The fit components of the B 1*s* spectrum in Fig. 3.8b1 appearing at 188.38 and 188.84 eV correspond to B atoms of Bo sheet experiencing two binding strengths to the topmost Ir atoms (see Section 4.1 for more elaboration on Bo-Ir binding). The third component of the fit at 189.42 eV corresponds to boron carbon nitride (B_xCN) hybrid bonds reported earlier in literature [91, 92]. The spectrum shown in Fig. 3.8b2 displays a small B 1*s* peak at 188.73 eV, originating from seemingly Bo-void Ir terrace marked with a black circle in Fig. 3.8a, may indicate the occurrence of some B clusters in that area. The bright area marked with orange circle in Fig. 3.8a (corresponding to the orange-circled region in Fig. 3.7a) mainly contains an amorphous BCN alloy (aBCN) because the predominant B 1*s* peak at 188 eV in Fig. 3.8b3 corresponds to the reported value of binding energy for aBCN in reference [92].

The three B 1*s* peaks of the spectrum in Fig. 3.8b4 originate from the area marked with the brown circle in Fig. 3.8a: a major contribution at 190.33 eV attributed to hexagonal BCN (hBCN) alloy and hBN (the triangular feature appearing darker than the surrounding area in the LEEM image) and two minor contributions: at 188 eV arising from aBCN [92] and at 188.90 eV corresponding to the binding energy values reported for boron carbides of different stoichiometries B_xC_y [92].

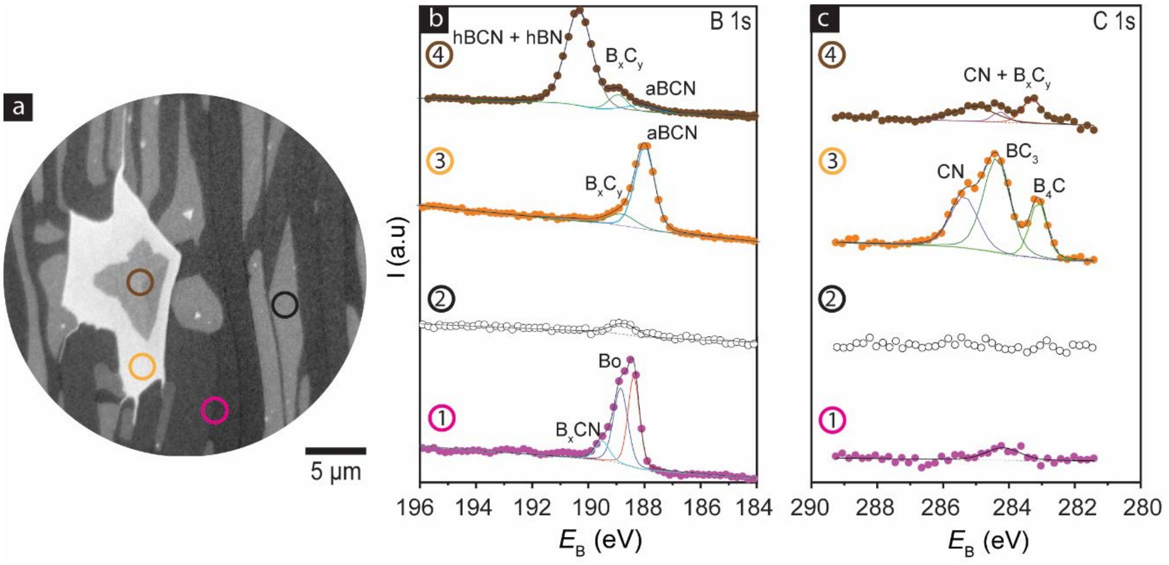

Figure 3.8 Core-level spectra of flawed region. (a) LEEM image of a various degrees of contrast showcases a region of Ir surface with mixed coverage. Field of view is 15 µm and electron energy is 24.14 eV. (b-c) the corresponding XPS spectra recorded in 1*s* spectral regions for B (b) and C (c) at photon energies 400 eV and 270 eV, respectively. The displayed spectra were extracted from four areas marked with the following colours: magenta, black, orange and brown.

The minor C 1*s* peak at 284.10 eV (Fig. 3.8c1) found in the Bo region (indicated with a magenta circle in Fig. 3.8a) indicates B-C bonding in the form B_xCN, as deduced from the examination of the B 1*s* peak. The three resolved C 1*s* peaks, extracted from the area marked with an orange circle in Fig. 3.8a, were fitted as follows: the first peak appearing at 283.10 eV may be assigned to boron carbide of B_4C stoichiometry, the second peak at 284.39 eV, corresponds to another boron carbide of BC_3 stoichiometry, and the third peak at 285.32 eV is ascribed to carbon bound to nitrogen (CN) [91, 92]. The corresponding XPS C 1*s* signal arising from the area marked with the brown circle in Fig. 3.8a indicates the formation of boron carbides of various stoichiometries B_xC_y and CN although in a smaller amount as compared to the orange-encircled region. Furthermore, the formation of graphene is excluded because of the mismatch of the aforementioned binding energy values with the C 1*s* value (284.2 eV) characteristic of pristine graphene / Ir(111) [93]. One may conclude that in the contaminated areas, marked with orange (predominantly aBCN) and brown circles (mostly hBCN and hBN), mixing of B, C and N atoms in various stoichiometric ratios took place during the synthesis of Bo. The carbon found in this region is likely to originate from degassing of the sample holder during thermal treatment or insufficient Ir surface cleaning prior to the Bo synthesis. One way to minimise the surface contamination with carbon is to repetitively anneal the sample in O_2 prior to dosing the borazine precursor. Apparently, having a Bo sample of relatively high coverage (> 0.8 ML) does not exclude the possibility of having regions contaminated with BCN thin films, sparse hBN islands or boron carbides. Thus, caution must be taken in data interpretation, especially of the data obtained from area-averaging techniques.

4 Electronic properties of borophene

The main results of this chapter were published in the following paper: Sherif Kamal, Insung Seo, Pantelis Bampoulis, Matteo Jugovac, Carlo Alberto Brondin, Tevfik Onur Menteş, Iva Šarić Janković, Andrey V. Matetskiy, Paolo Moras, Polina M. Sheverdyaeva, Thomas Michely, Andrea Locatelli, Yoshihiro Gohda, Marko Kralj, and Marin Petrović, *Unidirectional Nano-modulated Binding and Electron Scattering in Epitaxial Borophene,* ACS Applied Materials & Interfaces, 15, 57890-57900 (2023) [94].

4.1 Core-level spectroscopy

Spectral investigation of the core levels of the substrate and 2D material in question is crucial for understanding the nature of binding between the two in terms of strength and homogeneity. Therefore, a reference (conventional, area-averaged) XPS spectrum of pristine Ir in the 4*f* region was recorded prior to Bo growth on Ir substrate, Fig. 4.1a (bottom). The fitting procedure involves both surface and bulk components since they are found at two distinct binding energies. In addition, the two components of each of those peaks arise from spin-orbit coupling exhibited by the electrons of 4*f* orbital: the component $4f_{7/2}$ corresponds to lower E_B: 60.33 eV and 60.80 eV, and $4f_{5/2}$ corresponds to higher E_B: 63.33 eV and 63.80 eV. Thus, the difference in binding energies between surface (Ir_s) and bulk (Ir_b) is ~ 0.50 eV (Fig. 4.1a). The given values match the data reported in literature [95]. Following the Bo growth with high coverage (~ 0.8 ML), evidenced by the comparable intensities of Ir and Bo diffraction spots [37] (consult the LEED inset in Fig. 4.1a), the characteristic B peak in the corresponding 1*s* region (Fig. 4.1b) was recorded at the same photon energy. Although there was no change in the binding energies of Ir 4*f* spectrum (Fig. 4.1a, top), the reduction of surface-to-bulk intensity ratios for the spectral components by a factor of ~ 4 accounts for quenching of the Ir 4*f* surface component by the Bo monolayer on top of the Ir. Therefore, we presume the occurrence of considerable interaction between the Bo and Ir(111): similar reduction of the surface component peak is observed after adsorption of chemical species strongly bound to

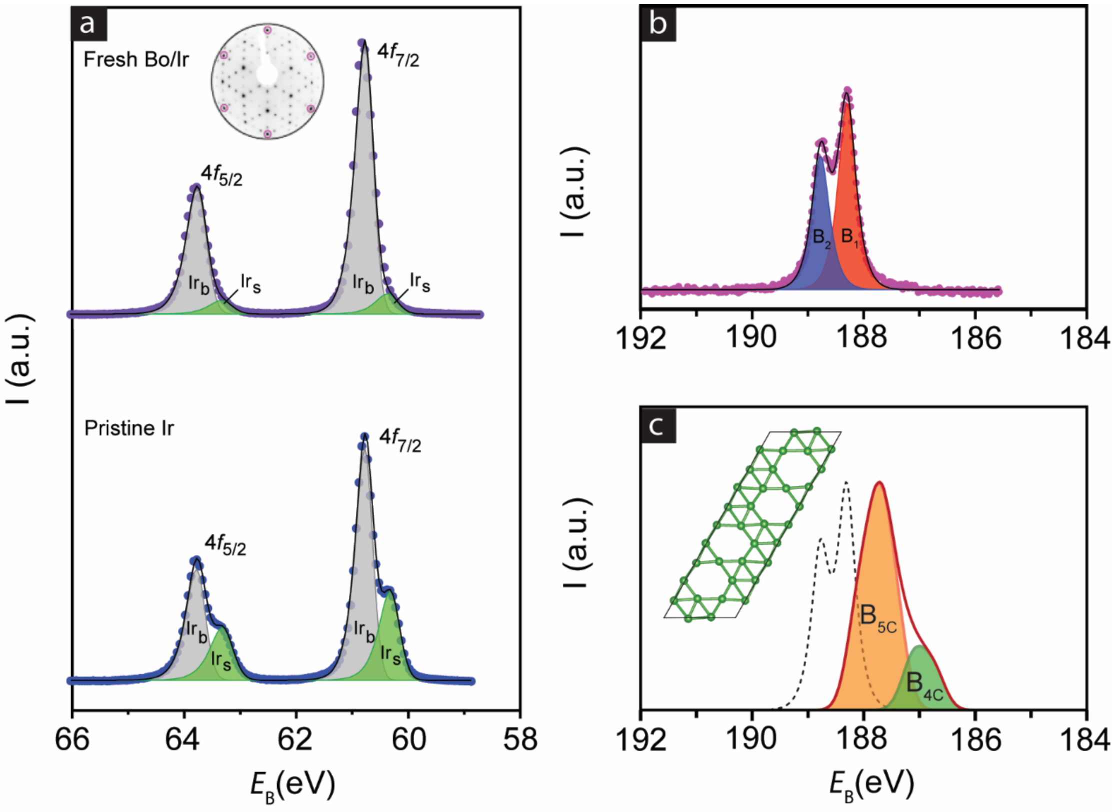

Figure 4.1 (a) Ir 4*f* spectra recorded for Ir(111) before and after Bo synthesis: pristine Ir (bottom) and Bo/Ir (top) samples. The surface components (Ir_s) decline by a factor of ~ 4 after Bo formation on the surface. The bulk components (Ir_b) remain intact. The LEED inset, revealing the characteristic Bo 6 × 2 superstructure, was recorded prior to the acquisition of the spectrum. (b) B 1*s* spectrum of freshly synthesized Bo/Ir sample, fitted with two components. The two distinctive components reveal inhomogeneous binding between B and Ir atoms. (c) Calculated XPS spectrum of freestanding Bo reveal two components, labelled B_{4C} and B_{5C}, arising from four- and five-coordinated B atoms, respectively. The unit cell of Bo χ_6 -polymorph is shown in the inset. The measured XPS spectra (a-b) were acquired via *p*-polarized light at *hν* = 300 eV.

the Ir surface [96, 97]. In contrast, in epitaxial layers exhibiting weak interaction, for instance graphene or hBN on Ir(111) [95, 98] , the surface component remains intact after the formation of 2D material on top. The relatively minute Ir 4*f* surface component is thought to have originated from the Bo-void patches of the Ir surface after the Bo formation, referring to the recent micro-XPS study of Bo/Ir where merely bulk Ir 4*f* peaks have been observed in fully covered Bo/Ir regions [99].

The B 1*s* spectrum of a freshly prepared Bo/Ir(111) sample, shown in Fig. 4.1b, was acquired for the purpose of investigating its chemical composition and binding strength of Bo to the Ir substrate. The spectrum is visually resolved into two distinct peaks located at the following binding energy values: 188.30 (B_1) and 188.78 eV (B_2). The ratio between the peaks' intensities ~ 1.4. The peaks were deconvoluted by a product of Gaussian-Lorentzian functions of the ratio 0.8 and peak width (FWHM) of 0.4 eV. No other boron-related peaks were found, which also excludes the formation of hBN layers [98]. Spin-orbit coupling plays no role here because of the zero value of the quantum number *l* of the 1*s* electron. One is, therefore left with the following two assumptions to account for the two B 1*s* peaks: coordination effect and/or inhomogeneity in binding between B atoms of Bo sheet and the topmost Ir atoms of the substrate. Further insight into the origin of the two peaks of B 1*s*, was gained from the theoretical simulations of XPS spectrum of freestanding Bo χ_6-polymorph. The inset in Fig. 4.1c. displays the relaxed positions of B atoms within the unit cell, which contains 25 atoms. The coordination number *i.e.* the number of first-neighbour B atoms surrounding each B atom, varies and may be either 4 or 5 [55]. The calculated spectrum has two peaks at 187 and 187.7 eV (Fig. 4.1c), with the dominant peak (B_{5C}) towards the higher binding energy, in contrast to the experimentally measured double-peaked spectrum where the more intense peak (B_1 peak in Fig. 4.1b) is found at lower binding energy. This difference in the peaks' intensities is due to the fact that five-coordinated B atoms outnumber the four-coordinated ones. The shift in E_B towards lower values in the calculated spectrum, when comparing it with the experimental one, indicated by a dashed line, is due to the absence of the substrate effect. Interestingly, the calculated spectrum matches the coordination effect reported in [47].

One may conclude that ascribing the B 1*s* two peaks to the coordination effect is not justified. However, the second assumption *i.e.* B-Ir binding inhomogeneity, reasonable as it seems, requires further confirmation, which will be provided in Section 4.3. Additional XPS data of *in-siu* / *ex-situ* aged Bo and Li-decorated Bo samples are provided in Sections 5.1.1 and 5.1.2 where XPS technique is used to investigate even more complex samples extending beyond pristine Bo.

4.2 Valence band structure

As a prerequisite, our interest is to have a detailed overview of the electronic structure of bare Ir(111) in order to facilitate detection of any Bo-induced modifications of the band structure and/or appearance of Bo-related features. Iridium, like other metals, hosts *k*-dependent energy band gaps. It also hosts surface states in which electrons wavefunctions are rapidly damped when moving away either from the crystal surface into vacuum or into the bulk of the crystal. In other words, surface state is a discrete energy level split from an energy band due to the disturbance caused by the free surface. Observation of surface states indicate that the crystal surface is clean *i.e.* no strong interaction exists between surface adsorbates and the topmost layer of the substrate atoms. The experimental investigation of the band structure of bare Ir along the Γ-K symmetry direction reveals four surface states marked with white arrows in Fig. 4.2: one parabolic state (Ir S_1) with a vertex at Γ-point ($k_{||} = 0$ Å^{-1}) and three states marked Ir S_2, S_3 and S_4 around the K- point ($k_{||} = 1.52$ Å^{-1}). For a detailed study of the band structure of Ir(111), the reader is advised to consult reference [100]. If novel features related to Bo valence band happened to appear within energy gaps of Ir band structure, in the vicinity of either Γ-point or K-point, they would be easily detectable. The work done earlier on graphene/Ir, for instance, provides a good example as graphene Dirac cones were observed within the parallelogram-like energy band gap at the K- point of Ir band structure [101]. If, however, intrinsic electronic bands of Bo overlap in *k*-space with Ir bands, hybridization effects would be expected due to the potentially strong interaction between Ir and the overlaying 2D material, as in the case of *e.g.* graphene/Ni system [102].

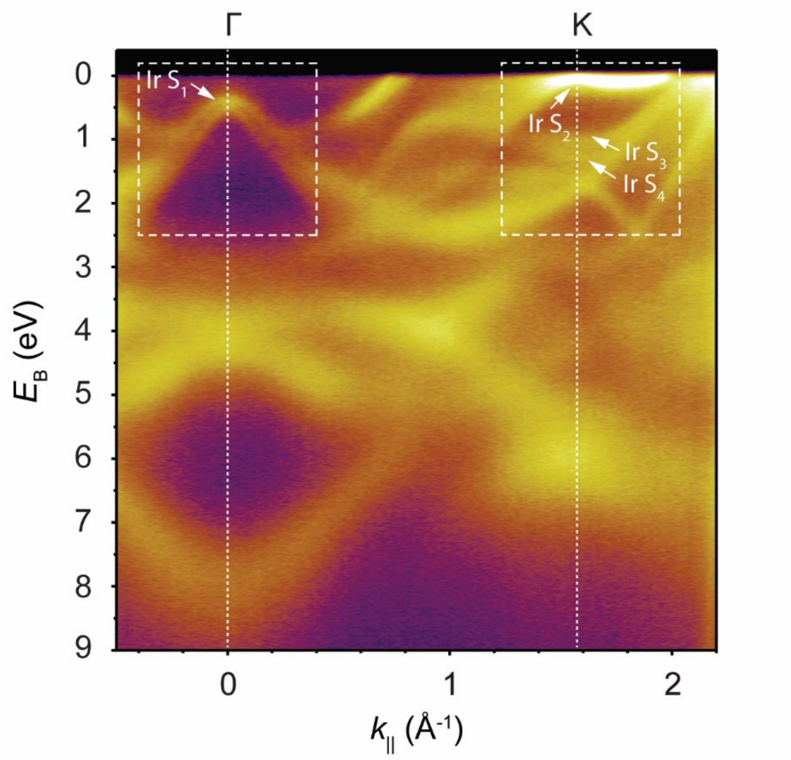

Figure 4.2 ARPES characterisation of bare Ir(111) $k_{||}$ along the symmetry line Γ-K reveals four surface states indicated as follows: Ir S_1 at Γ-point ($k_{||}$ = 0 Å^{-1}), and Ir S_2, Ir S_3 and Ir S_4 around the K- point ($k_{||}$ = 1.52 Å^{-1}). The spectrum was recorded at *hν* = 100 eV.

After growing Bo, the sample was mapped via a spatially averaging ARPES with a spot size diameter of ~ 0.5 mm. The ARPES spectrum shown in Fig. 4.3a reveals new electronic bands in the gap surrounding Ir S_1, and no other novel bands were detected. The newly observed bands show linear energy dispersion extending down to ~ 1 eV of binding energy. They also appear in the Fermi surface of Ir as three pronounced arc-like features in the proximity of the centre (Γ-point) of surface Brillouin zone (SBZ) indicated by the white arrows in Fig. 4.3b. The three arc-like features correspond to the rotational domains of Bo (consult Fig. 3.3). The novel bands are not intrinsic to Bo because of two reasons: they are located outside the Bo 1st surface Brillouin zone, and the arcs shape bears no resemblance to the expected geometry arising solely from the symmetry of Bo surface Brillouin zones.

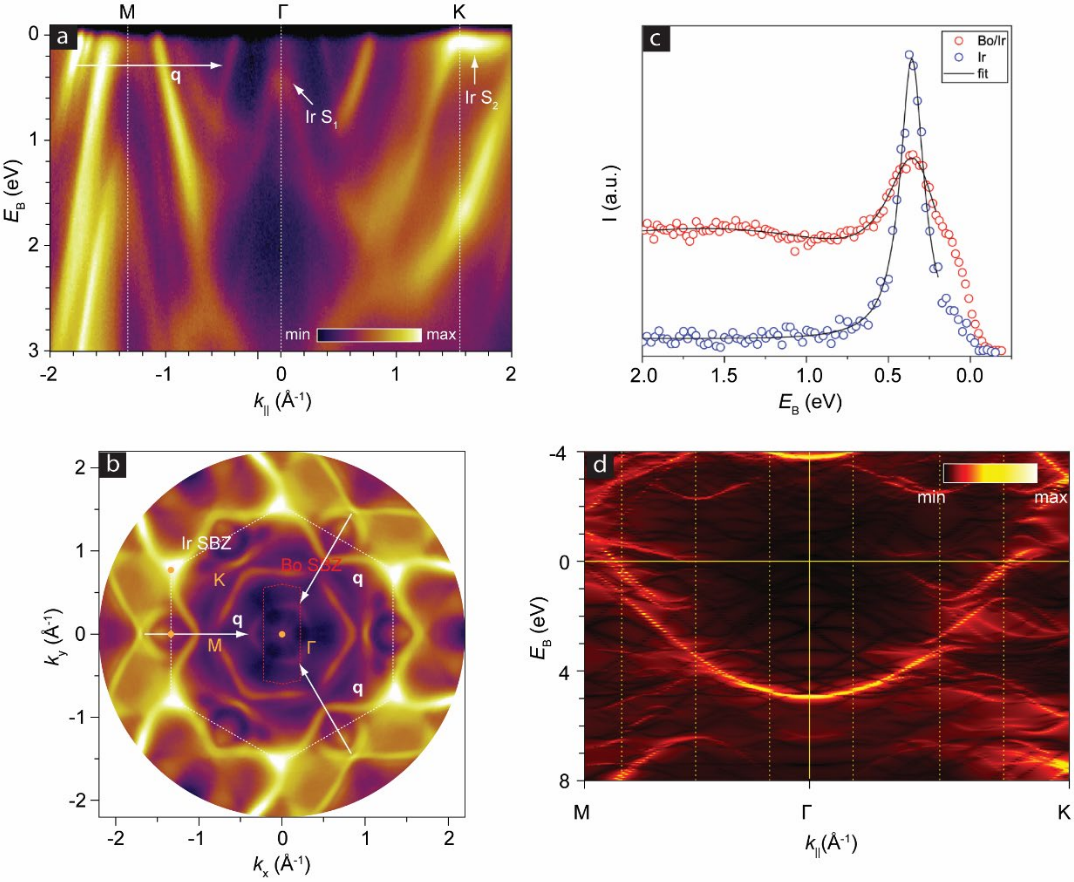

Figure 4.3 ARPES spectra of Bo epitaxially grown on Ir(111). (a) Spectrum along the M−Γ−K symmetry line. The wavevector **q** and surface states of Ir (Ir S_1 and Ir S_2) are marked with white arrows. (b) Fermi surface of epitaxial Bo on Ir: the 1st surface Brillouin zone of Ir(111) and Bo are marked with white regular hexagon and red elongated hexagon, respectively. The white arrows simultaneously indicate both Bo-induced bands and the replication wavevectors **q**. (c) EDCs at the Γ-point before and after growing Bo on Ir(111) (indicated with blue and red circles, respectively). The spectra were acquired with *p*-polarized light at $h\nu$ = 100 eV. (d) Calculated valence band structure of freestanding Bo. The boundaries of 1st, 2nd and 3rd surface Brillouin zones of Bo are marked with vertical yellow dashed lines.

By comparing the dispersion of the newly observed Ir band in Fig. 4.3a to the dispersion of other intrinsic Ir bulk bands, we find that it resembles the dispersion of the intrinsic band located at the tail of the wavevector **q** arrow**.** One, therefore may rightly assume that the band, located at the head of the wavevector **q** arrow in Fig. 4.3a, is a Bo-induced Ir band arising from Umklapp process. Consequently, the three vectors **q** sketched in Fig. 4.3b, pointing from the original Ir bands towards the Bo-induced bands along Γ-M symmetry line, are assumed to be replication wavevectors. The magnitude of each wavevector is $|\mathbf{q}| = 1.33$ Å^{-1}. It is worth adding that the position and intensity of Bo-induced bands remain intact in UHV environment, for up to ten hours following the sample synthesis. This enhances the credibility of the replication scenario, because Bo valence band structure is also expected to be influenced by any chemical modification of Bo (see Section 5.2).

Energy distribution curves (EDCs), extracted at the Γ-point from the ARPES spectrum shown in Fig. 4.3a and displayed in Fig. 4.3c, feature an unaltered surface state Ir S_1 binding energy after the formation of Bo overlayer. However, the surface state intensity declines (by a factor of 2) as the corresponding linewidth increases (by a factor of 2.4). The broadening of surface state linewidth signals a reduction of the surface state at the Γ-point. Although the impact of the Bo uncovered Ir surface on such reduced coherence may not be excluded, due to the contributions from both Bo and Bo-free regions to the area-averaged ARPES signal, it is likely the surface state is influenced by the Bo sheet formed on the surface of Ir.

To complement the experimental data, theoretical calculations of the band structure of freestanding Bo were carried out. It was found that the most pronounced feature in the calculated band dispersion (Fig. 4.3d) is a parabolic band with the vertex at $E_B \sim 5$ eV. No pronounced electronic bands are noticeable adjacent to E_F near the Γ-point, which may be considered another evidence for the plausible Ir band replication scenario.

SBZs of Ir (grey hexagon) and Bo (red hexagon) are sketched in Fig. 4.4a. The vectors of the *k*-space unit cells of Ir are indicated as $\boldsymbol{g}_1$ and $\boldsymbol{g}_2$, and those of Bo are indicated as $\boldsymbol{b}_1$ and $\boldsymbol{b}_2$. The dots mark the reciprocal lattice points of Ir and Bo. It is important to emphasize that the wavevectors $3\boldsymbol{b}_1$ or $\boldsymbol{b}_2$ themselves, matching in magnitude the value $|\mathbf{q}|$, could not induce the Umklapp process, since in that case replicated bands would have emerged near the edges of the SBZ of Ir along with the three replicas observed in the vicinity of the Γ-point. Thus, the proposed replication scenario must be induced by some Bo-related feature of lower symmetry, other than the reciprocal lattice of Bo. As it turns out, replication is caused by Bo stripes which may be considered a 1D lattice with a wavevector $\mathbf{q}$ (see Section 4.3 for the corresponding STM data description). One may infer from the ARPES data of the Fermi surface displayed in Fig. 4.3b that the observed band replication occurs only for Ir electrons whose momentum is perpendicular to the Bo stripes.

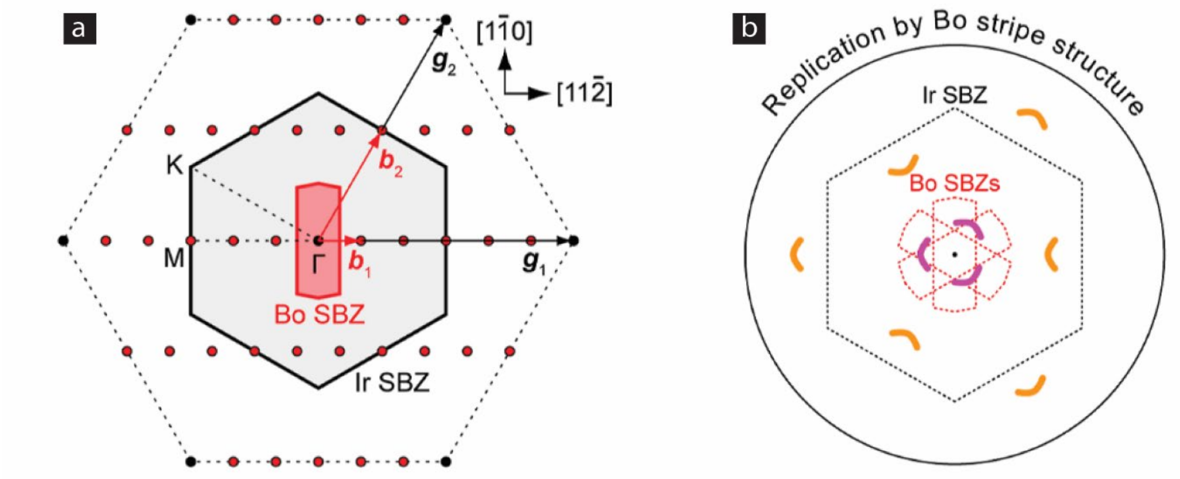

Figure 4.4 (a) A sketch of the reciprocal unit cells of Ir (the black hexagon and the reciprocal vectors $\boldsymbol{g}_1$ and $\boldsymbol{g}_2$) and Bo (the elongated red hexagon and the reciprocal vectors $\boldsymbol{b}_1$and $\boldsymbol{b}_2$). The grey and red fillings of the hexagons correspond to the SBZs of Ir and Bo, respectively. The dots indicate the lattice points of Ir and Bo in *k*-space. (b) A sketch of Fermi surface, illustrating the band replication by the Bo stripes. The three 120°-rotated SBZs of Bo are shown. The intrinsic Ir bands and its replicas are indicated with yellow and magenta features, respectively.

Umklapp processes resembling this 1D scattering scenario have also been reported for the following systems: graphene nanoribbons on Ni(771) [103], graphene sheets on Pt(997) [104] and reconstructed Au(001) [105]. Band replication has been reported earlier for other 2D materials grown on well-defined metallic substrates such as silicene on Ag(111) [106] and TaS on Au(111) [107]. To note, there may be a correlation between band replication and significant surface localization of the replicated electronic state. To elaborate, the Ir state undergoing Umklapp replication in our experiments is localized on the surface of Ir which matches the band structure calculations from references [108, 109]. One, therefore, may conclude that surface localization of the electrons, which are more sensitive to the scattering potential of the 1D lattice of Bo located directly above them, might be the reason behind the scattering of this particular state as suggested in literature [103-109].

4.3 Topography and spectroscopy at the nanoscale

STM and STS measurements revealed atomic-scale features of Bo/Ir (111) topography and electronic structure. Fig. 4.5 displays a characteristic STM image of the system, with a distinctive stripy pattern of Bo $\chi6$ polymorph. The stripes, separated by trenches that appear darker in colour, run diagonally across the field of view. Two parallel rows of lobes, forming two wave-like substripes, constitute each stripe. The width of each stripe has been estimated to be $d = 14.0 \pm 0.1$ Å , in agreement with other investigations of the same Bo polymorph [55, 48, 47]. Substrate role in the formation of the stripy pattern of Bo is evident when comparing freestanding Bo with substrate-supported Bo: the freestanding Bo displayed in the DFT generated image (the inset in the top-right corner of Fig. 4.5a) is void of any stripes.

STS measurements were performed in order to examine the contribution of the electronic structure to such appearance of Bo on Ir(111). Fig. 4.5b shows two-point spectra, recorded at the lobe (P_1) and trench (P_2) positions. The spectra adopt an asymmetric V-shape near Fermi level E_F, thus indicating the metallic nature of Bo/Ir. The two spectra, however, differ significantly within the energy range 0.3 - 0.5 eV below the Fermi level where the P_1 spectrum has DOS much higher than P_2 spectrum. Higher DOS is linked to the electronic state observed on the bare Ir(111) surface (refer to the inset of Fig. 4.5b) and can be assigned to the surface state of Ir located at the Γ-point [100]. Therefore, one may conclude that although the Ir surface state remains pronounced under the Bo sheet in the lobe positions, however with spatial modulation in intensity, it is suppressed in the trench positions. Since surface states are often quenched when interacting strongly with adsorbed species [110, 111], we conclude that the interaction between B and Ir atoms varies in strength. In addition, the spatially modulated intensity of the Ir surface state is better visualized in the STS line scan displayed in Fig. 4.5c. The line scan displays a periodic sequence of high DOS regions at the lobe positions, 0.3 - 0.5 eV below the Fermi level, *i.e.* at negative sample bias, as evident from a comparison with the topographic image in the inset, while the area lying in between two consecutive lobes correspond to low DOS regions. This correspondence between line scan and the topographic images provides a connection between the Bo crystal structure and the coherence of Ir surface state. In other words, a strong B-Ir binding corresponds to a suppressed Ir surface state (low DOS region) which is a state strongly perturbed by B atoms, whereas a weaker B-Ir binding corresponds to the pronounced Ir surface state (high DOS region) which is a state weakly perturbed by B atoms. Furthermore, one may assume, referring to Fig. 4.1b, that the B_1 and B_2 components of B 1*s* peak correspond to weakly bound lobe and strongly bound trench (Fig. 4.5a), respectively. Thus, the spectral modifications of Ir surface state (Ir S_1) shown in Fig. 4.3c and its spatial intensity modulation (Fig. 4.5b-c) are related features showcasing Bo-Ir inhomogeneous binding.

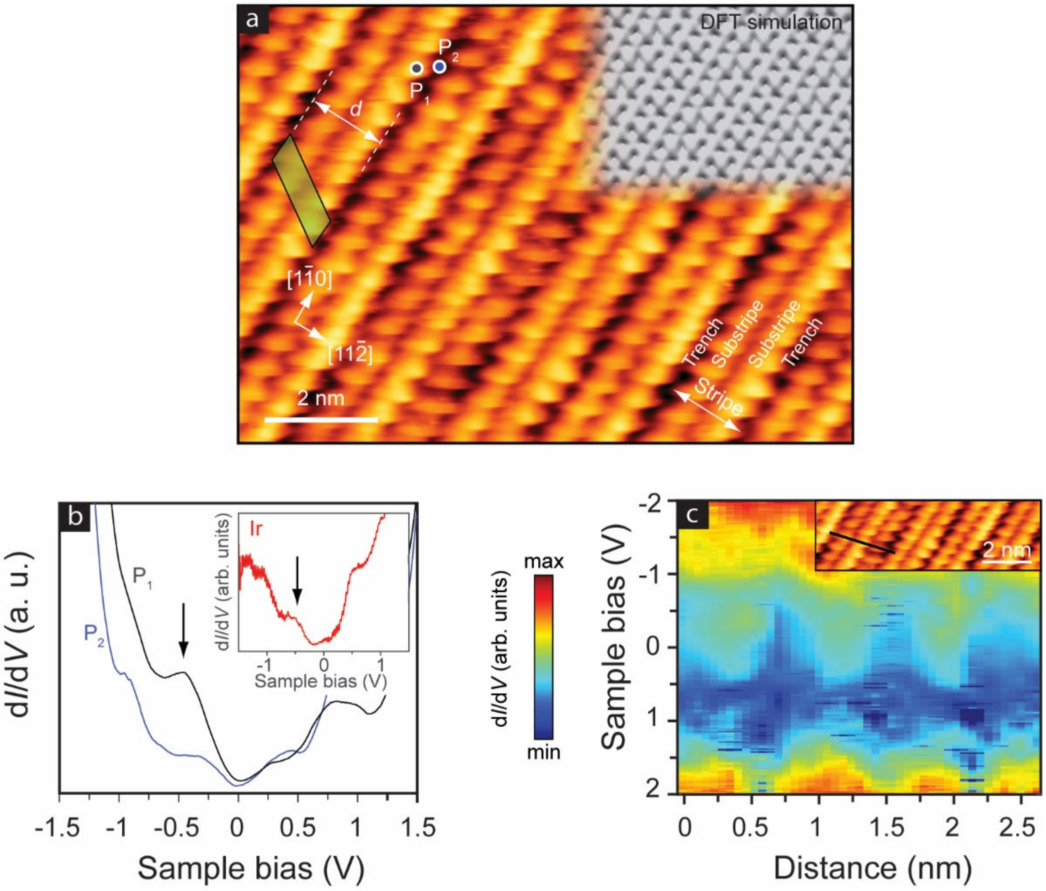

Figure 4.5 STM and STS of Bo on Ir(111). (a) A striped Bo sheet is revealed by a high-resolution STM topographical image. The stripe width is d = 14.0 ± 0.1 Å. The unit cell of Bo is indicated by a green parallelogram. Set points: − 0.5 V, 0.5 nA. A DFT-simulated STM image of a freestanding χ_6 Bo is shown in the inset (top right corner). (b) dI/dV spectra acquired at the P_1 and P_2 positions in (a): P_1 features Ir surface electronic state peak at − 0.4 eV (marked by an arrow) which is absent at position P_2. Set point: 0.5 nA. Inset: the dI/dV spectrum of the bare Ir(111) surface; the state at − 0.4 eV is present. Set point: 0.5 nA. (c) The electronic structure across consecutive Bo stripes: the dI/dV line spectroscopy, acquired along the black line shown in the inset, displays modulation −0.4 V. Set points: 0.5 nA (− 0.5 V, 0.5 nA for the inset).

Upon comparing ARPES data of Section 4.2 with STM/STS data shown in this section, it was found that one third of the Bo stripe width (*d*/3) in real space - matching the separation between the two substripes - corresponds to the replication wavevector length in reciprocal space *q* by calculating ($2\pi/q$) = 4.69 ± 0.03 Å. Such a periodicity is a length-scale hallmark of both Ir surface-state modulation in a direction perpendicular to the Bo substripes in one Bo rotational domain. One, therefore, may conclude that the unidirectional nanoscale modulation of the binding between Bo and Ir perturbs the Bo layer such that it forms 1D scattering lattice with a principal scattering component q, giving rise to the observed Umklapp process. Henceforth, the three arc-like features observed in the Fermi surface of Bo on Ir arise from the three rotational Bo domains.

4.4 Summary

When a comparison is drawn between the experimental data and theoretical simulations given in this chapter, one may conclude that monolayer Bo sheet exhibits a considerable nanoscopic and unidirectional modulation on the Ir substrate. The modulation is regarded as evidence for the nonuniformity in B-Ir binding, thus affirming the second assumption made in Section 4.1 regarding the inhomogeneity in B-Ir binding. Although the B atom coordination effect within the Bo sheet is most likely present in our XPS data, it is overshadowed by the B-Ir binding inhomogeneity. Furthermore, only electrons with momentum perpendicular to the Bo stripes (having width *d* ~ 1.4 nm) of an extended Bo-sheet experience scattering and causes the sheet to function as an electron diffraction (scattering) grating. The Ir-replicated bands, observed close to Fermi level in the ARPES spectra of Bo/Ir, demonstrate the resultant electron diffraction. This system serves as a good example for the potential of 2D materials as a scattering medium.

5 Beyond pristine borophene

Some of the results shown in this chapter were published in the following paper: Sherif Kamal, Insung Seo, Pantelis Bampoulis, Matteo Jugovac, Carlo Alberto Brondin, Tevfik Onur Menteş, Iva Šarić Janković, Andrey V. Matetskiy, Paolo Moras, Polina M. Sheverdyaeva, Thomas Michely, Andrea Locatelli, Yoshihiro Gohda, Marko Kralj, and Marin Petrović, *Unidirectional Nano-modulated Binding and Electron Scattering in Epitaxial Borophene,* ACS Applied Materials & Interfaces, 15, 57890-57900 (2023) [94].

5.1 Borophene ageing

5.1.1 *In situ* ageing of borophene

The B 1*s* XPS spectrum of a fresh Bo/Ir(111) sample (Fig. 5.1a) acquired following Bo growth (see Section 3.1) will be used as a reference to examine the chemical stability and ageing of Bo in different environments. The well-resolved components at 188.30 and 188.78 eV are ascribed to the nonuniform B-Ir binding as elaborated in Section 4.1. The ageing effect was studied by merely monitoring the modifications of the B 1*s* peaks over a long time span while keeping the sample in UHV conditions (base pressure of 10^{-10} mbar) and at room temperature. The two spectra in Figs. 5.1b-c were recorded 11 and 22 hours following the synthesis, respectively, and were fitted with four components. The spectra display changes of the initial B_1 and B_2 peaks along with the formation of two new peaks B_3 and B_4 at higher binding energies at 189.07 and 189.37 eV, respectively. The small-intensity B_5 peak at binding energy 192.2 eV emerges after 22 hours of ageing and it may be ascribed to B_xO_y [112, 113]. The B_1 peak displays no energy shift, however as the sample ages, the peak intensity diminishes. In contrast, the B_2 peak intensity remains almost constant whereas it displays a slight energy shift towards lower values by 74 meV. The ratio I_{B1}/I_{B2} is reduced to 0.65 after 22 hours (for the fresh sample, that ratio was ~ 1.4).

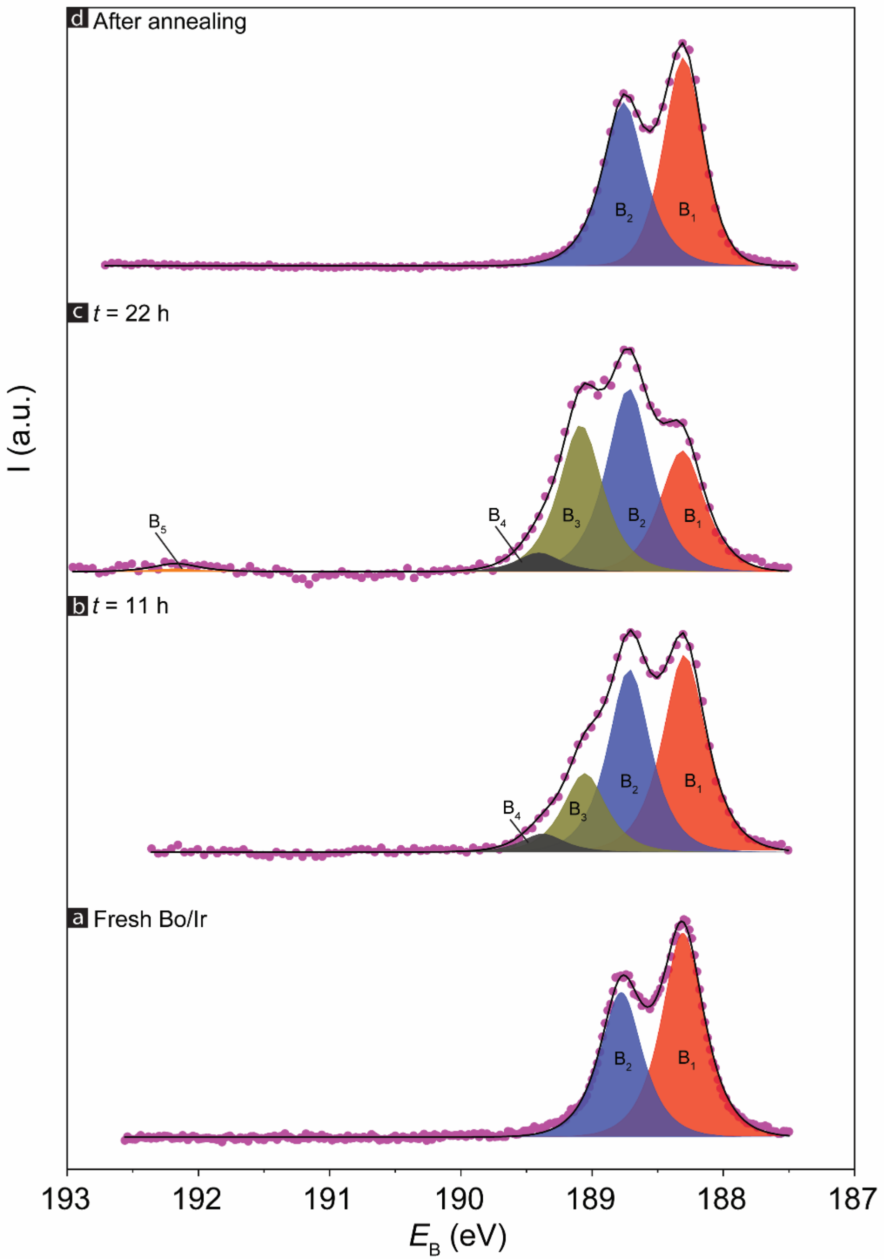

Figure 5.1 XPS spectra of in-situ aged Bo. In comparison with the pristine Bo reference spectrum (a) where only two B 1*s* components (B_1 and B_2) are present, 11 and 22 h aged samples (b and c) exhibit the appearance of new components (B_3, B_4 and B_5) signalling Bo contamination with adsorbed species coming from the UHV chamber. The spectrum of the annealed sample (d) resembles the spectrum of the initial pristine Bo/Ir sample with restored positions and intensities. $h\nu = 300$ eV.

The changes in B 1*s* peak are due to the Bo binding to residual C- and/or O-containing chemical species in the UHV chamber [112-114]. The vacuum base pressure inside the chamber, *i.e.* the partial pressure of the gases above the walls of the chamber stainless steel from inside, is significantly lower than atmospheric pressure, which creates a driving force for the gases to diffuse out of the steel giving rise to C- and/or O- contamination. By comparing the intensity ratio of the pristine and aged Bo peaks, one may conclude that approximately 1/3 of B atoms in the Bo sheet were bound to the residual molecules in the UHV chamber after 22 hours of ageing. In addition, the decline in the B_1 peak intensity indicates that dominantly the B atoms weakly bound to Ir atoms underwent oxidation. The chemically inert 2D materials, such as hBN, in contrast to Bo, display no contamination when exposed even to air for a long time as revealed by XPS [115]. Enhancement of Bo stability may be achieved by capping Bo with another inert 2D material like hBN or graphene, thus forming a vertical heterostructure such as hBN / Bo [47] or graphene / Bo [99].

It was found that pristine Bo was retrievable by flashing the aged sample to 1100 °C followed by immediate cooldown. The recorded B 1*s* spectrum for the retrieved Bo (Fig. 5.1d) resembles the one recorded for freshly prepared sample (Fig. 5.1a). The sample flashing leads to boron dissolution into Ir and simultaneous desorption of surface contaminants. Pristine Bo patches form as B atoms segregate back onto the Ir surface during the cooldown. Elaborate studies on Bo growth kinetics such as [48] and [90] may be consulted for an in-depth treatment of the subject.

5.1.2 *Ex situ* ageing of borophene

After the Bo sample was characterised in-situ at the VUV beamline in Elettra, it was taken out of the UHV chamber to age for one year in ambient conditions. Its loading back into UHV and short annealing (flashing) to 1100 – 1200 °C were performed in order to study the retrievability of Bo after such an extended period of exposure to air. The annealing took place at Faculty of physics in Rijeka inside the analytical UHV chamber of the XPS setup. Prior to the 1st annealing, reference XPS spectra (Fig. 5.2a-c; bottom) were recorded for B 1*s*, C 1*s* and O 1*s* to investigate the status of the sample. There was merely noise in the spectral region of B 1*s* (Fig. 5.2a) which was expected due to the effect of surface adsorbates whereas B atoms lay buried underneath. The sample exposure to ambient conditions results in the formation of such surface adsorbates. In accordance with the B 1*s* absence, there was evidence of significant oxidation and formation of carbides as revealed by C and O peaks in their respective 1*s* regions Fig. 5.2b-c, bottom spectra. XPS spectrum of C at 284.30 eV may support the likelihood of having boron carbides B_xC_y, alongside adventitious carbon formed on the substrate due to long exposure to ambient conditions [48, 116].

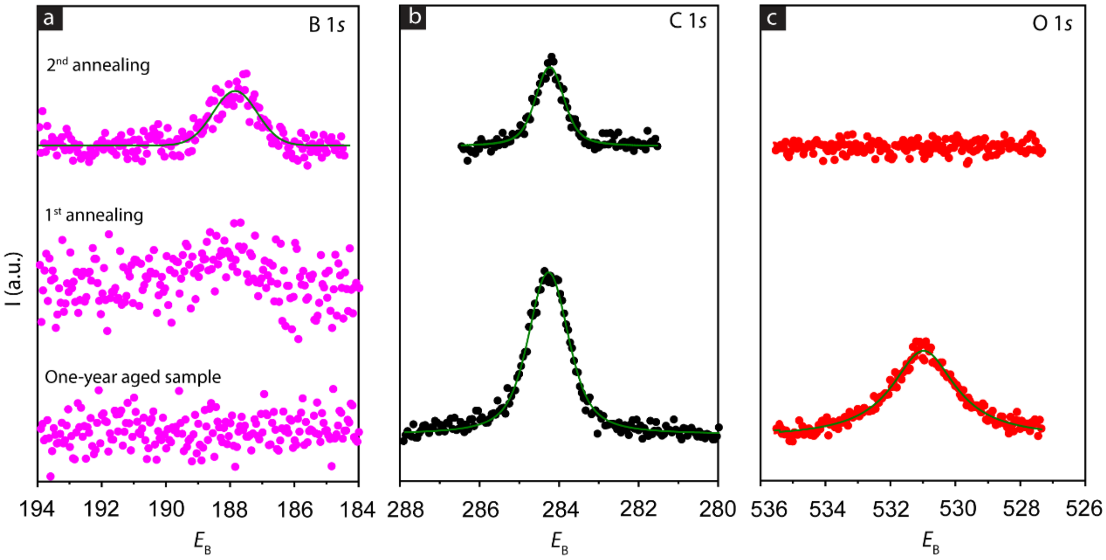

Figure 5.2 XPS spectra recorded before and after the first and second flashings of the one-year aged Bo sample. (a) B 1*s* spectra: characteristic peak emerges as a result of flashing. (b) C 1*s* spectra: the amount of carbon diminishes after flashing. (c) O 1*s* spectra: oxygen was completely gone after 2nd flashing of the sample. All spectra were recorded at $h\nu = 1.48$ keV.

1st annealing cycle, which lasted seven minutes at a background pressure of $p \sim 10^{-7}$ mbar (sample degassing), led to the emergence of a weak signal at the position of the B 1*s* peak as shown in the middle spectrum of Fig. 5.2a. The B 1*s* peak at 187.94 eV becomes clearly visible, as shown in Fig. 5.2a (top), after 2nd annealing, which was run for four minutes at the background pressure of $p \sim 10^{-8}$ mbar. The peak position is shifted by 0.36 eV towards lower binding energy in comparison to the pristine Bo

(Fig. 5.1a). The shift may suggest the presence of carbon adsorbates on the surface. For the same sample, the amount of carbon on the sample surface was reduced by 64%, as evidenced from the decrease in C 1*s* peak area Fig. 5.2b (top). The reduction in the C 1*s* peak area may be ascribed to the desorption of carbon adsorbates from the surface which, apparently, was not complete at the annealing conditions applied. The oxides, however were no longer adsorbed onto Ir surface as evidenced by the noise obtained in the O 1*s* spectral region Fig. 5.2c (top) *i.e.* no remnant oxygen was detected. Thus, as a result of 2nd annealing of the one-year-aged sample, Bo regions could be retrieved on the Ir surface, however there was still carbon contamination on the surface.

For comparison, it has been reported [35] that one-minute of ambient exposure of Bo on Ag(111) results in reduction of pristine B 1*s* peak intensity, signalling accumulation of surface adsorbates. This was accompanied by the emergence of a new B 1*s* peak at ~192 eV which is indicative of B–O bonding. Five-minute ambient exposure of the degraded Bo did not change the XPS spectra significantly, which indicates rapid degradation of Bo due to its high reactivity [35]. Apparently, minute-long exposures of Bo to air do not necessarily lead to its complete oxidation. However, during prolonged exposure of Bo to ambient, reaching up to one year as in our case, sample degradation is total unless it is covered by a protective layer which provides chemical stabilization, such as a relatively thick (> 6 nm) layer of AlO_x [117].

The effects of Bo exposure to ambient conditions were also studied on the nanoscopic level by utilizing STM and STS. Another Bo sample was freshly prepared in the UHV chamber at the Institute of Physics in Zagreb using the growth parameters reported earlier in Section 3.1 (Table 3.1), it was taken out of the chamber and transported to the University of Twente in the Netherlands. The overall time of exposure to ambient conditions was approximately six days. Insertion of the air-exposed sample back into UHV was followed by its initial low-temperature annealing at 300 – 400 °C and $p \sim 10^{-7}$ mbar for 21 minutes which did not improve the rough and contaminated Ir terraces as evident from the STM topography images shown in Fig. 5.3a-c. Afterwards, the 1st high-temperature annealing ($1200 \geq T > 1000$ °C, $p \sim 10^{-7}$ mbar) for 5 minutes was performed with the aim of triggering dissolution-segregation process and retrieving pristine Bo regions on the surface as described in Section 5.1.1. However, STM imaging showed no improvement of the rough and contaminated Ir terraces (not shown). Eventually, the 2nd high-temperature annealing ($1200 \geq T > 1000$ °C, $p \sim 10^{-7}$ mbar) for 18 minutes, led to partial recovery of Bo patches, recognized by their stripy appearance (Fig. 5.4a-b) and ranging in width between 3.8 and 13 nm. The spatial orientations of Bo patches marked with white arrows in Fig. 5.4b demonstrate the three rotational domains of Bo discussed earlier in Sections 3.1 and 4.2. Partial loss of B atoms is expected after 2nd annealing due to the desorption of B atoms from the surface and their trapping in the bulk of Ir crystal. Thus, the formation of Bo patches and perhaps even nanoribbons (see below) on Ir terraces was more likely to happen instead of more extended Bo layers covering the entire Ir terraces.

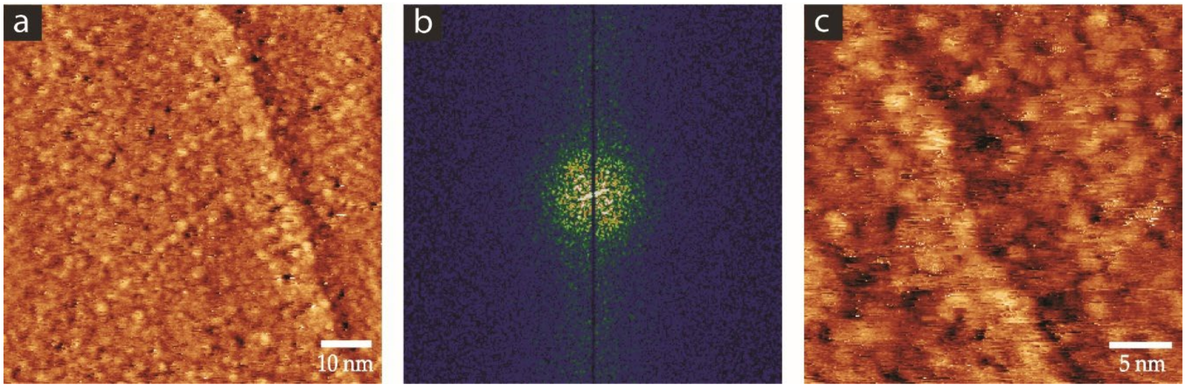

Figure 5.3 STM images recorded after low temperature annealing 300 – 400 °C of aged Bo/Ir(111). (a) Disordered arrangement, evidenced by the corresponding FFT pattern shown in panel (b), of what appears to be contaminants adsorbed onto Ir surface (75×75 nm^2, $I = 0.2$ nA, $V = -0.4$ V). (c) An enlarged view of the Ir terrace edge covered with contamination (30×30 nm^2, $I = 0.2$ nA, $V = -0.4$ V).

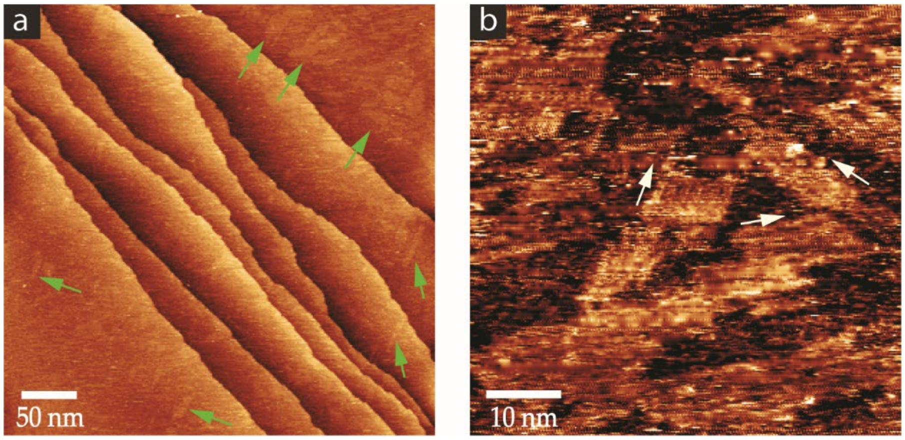

Figure 5.4 STM images displaying first evidence of retrieved Bo patches as a result of high temperature annealing (1200 > T > 1000 °C) of aged Bo/Ir(111). (a) An overview of Ir terraces with partial Bo coverage appearing as scattered patches as indicated by green arrows (400 × 400 nm^2, $I = 0.3$ nA, $V = -0.5$ V). (b) One terrace of Ir with irregular Bo patches in three rotational domains the directions of which are indicated by white arrows (58 × 58 nm^2, $I = 0.3$ nA, $V = -0.2$ V).

The V-shaped graph of (dI/dV) versus the applied bias to the retrieved Bo sample is displayed in Fig. 5.5 reveals the metallic nature of Bo stripe where dI/dV is approximately proportional to the density of states for small samples biases. For comparison, the dI/dV curve of a freshly-made Bo sample (the sample shown in Section 4.3) is also shown in Fig. 5.5. Both graphs feature asymmetrical rate of decrease in LDOS with respect to E_F of the scanned different Bo samples. Moreover, the similarity of the dI/dV patterns also implies the full recovery of electronic properties of Bo.

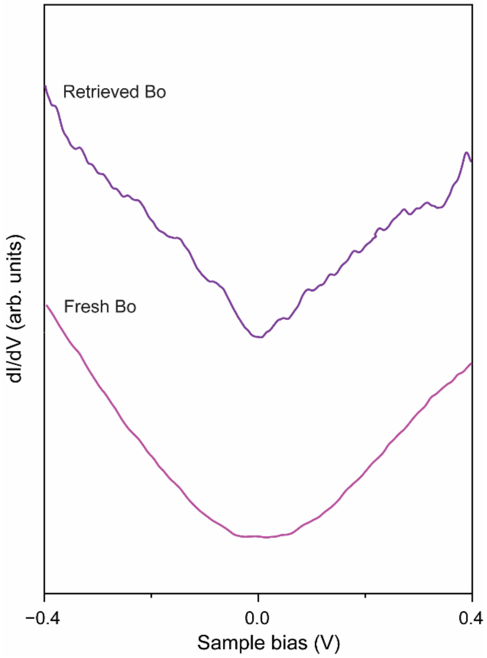

Figure 5.5 dI/dV spectra recorded for fresh and retrieved Bo stripes. A similar V-shape, which is a signature for the metallicity of the measured regions, suggests a full recovery of Bo after annealing the ex-situ aged sample. 15-point adjacent-averaging smoothing was applied to each curve in order to lower the noise level (I = 0.4 nA).

Bo islands and patches may be thought of as being made of a series of parallel Bo nanoribbons (~10 nm in length on average) (Fig. 5.6a-b), where a nanoribbon is actually one stripe of the Bo structure as described in Section 4.3. Therefore, the width of a nanoribbon may be estimated by measuring the width of an island or a patch and counting the number of stripes within it (see below). Obviously, a single nanoribbon can be considered to be the basic building block of Bo layer because of two reasons: (i) neither a "half-ribbon" nor a sub-stripe (in terms of its width) was ever observed; (ii) all Bo islands always contain an integer number of ribbons. One characteristic feature of the isolated Bo nanoribbon is the zig-zig pattern of atomic arrangement displayed in Fig. 5.6d, originating indeed from aforementioned lobes (see Section 4.3), which is preserved in Bo islands and extended layers as well (see Fig. 4.5a). The average Bo nanoribbon width ($d \approx 1.56$ nm) (Fig. 5.6d) was estimated from the line profile shown in Fig. 5.7 made across three Bo stripes of the Bo patch displayed in Fig. 5.6b.

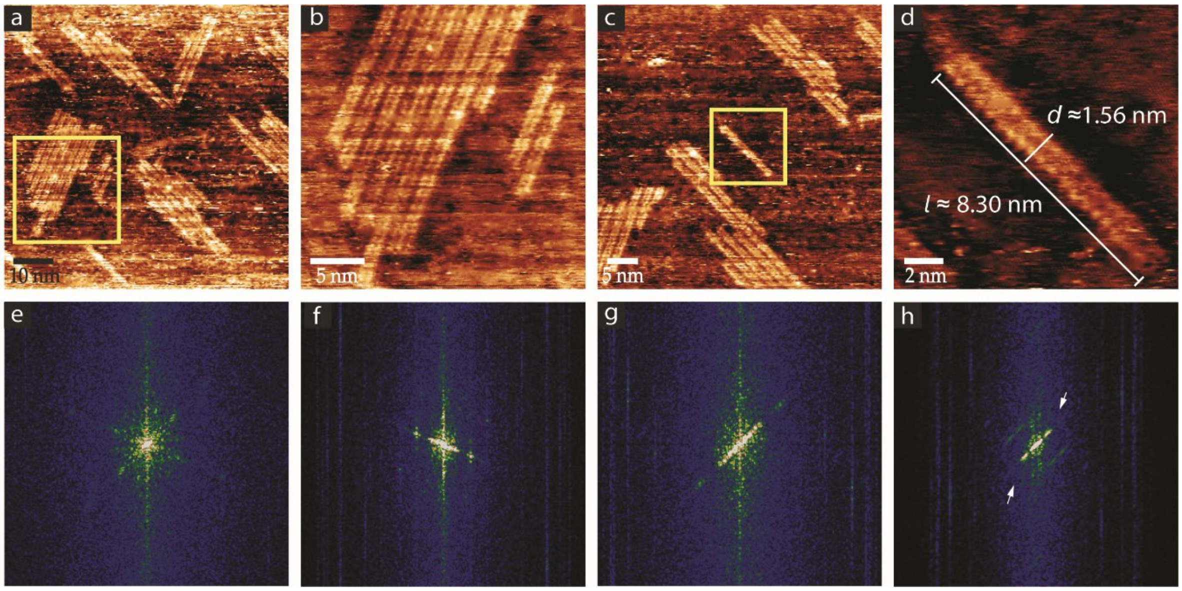

Figure 5.6 STM images of retrieved Bo following high temperature annealing (1200 > T > 1000 °C) of aged Bo/Ir(111). (a) Bo patches of various widths and two 60°-rotated spatial orientations (~ 70 × 70 nm^2, I = 0.3 nA, V = - 0.32 V) (b) Zoom-in to the area marked by a yellow square in (a) (25 × 25 nm^2, I = 0.4 nA, V = - 0.2 V) (c) Co-existing Bo patches and nanoribbons (50 × 50 nm^2, I = 0.4 nA, V = - 0.3 V) (d) Zoom-in to the area marked by a yellow square in (c), displaying a solitary Bo nanoribbon of the following dimensions $l \approx 8.3$ nm and $d \approx 1.56$ nm (14 × 14 nm^2, I = 0.4 nA, V = - 0.3 V). (e-g) FFT patterns reveal the region predominant spatial orientation(s) in STM images (a-c). (h) The ring-like feature seen in the FFT pattern of the single Bo nanoribbon in panel (d), marked by white arrows, arises from the zig-zig pattern of atomic arrangement in the nanoribbon.

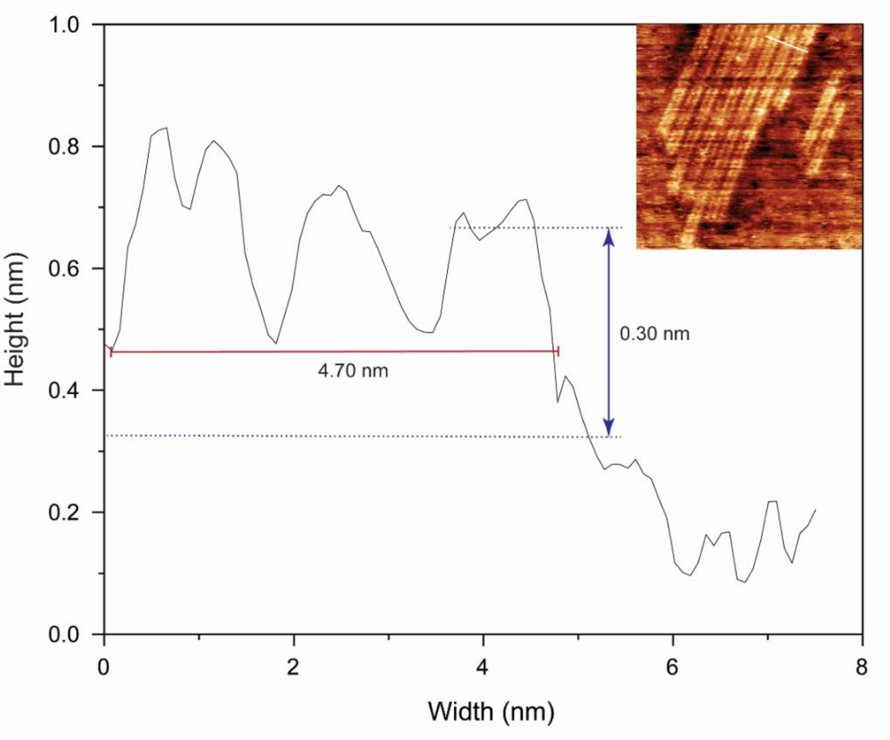

Figure 5.7 Line profile extracted along the white line drawn across the three Bo nanoribbons of the Bo patch shown in the STM inset. The height is ~ 0.3 nm. The width of a nanoribbon (*d* ≈1.56 nm) was estimated by averaging the widths of the three nanoribbons marked in the inset.

For comparison, metallic Bo nanoribbons fabricated via B atoms evaporation have been reported on Au(111) [118] which are narrower (~1 nm) and longer (20 nm) than the ones shown in Fig. 5.6. Also, Li *et al.* reported two mixed phases of Bo nanoribbons grown on vicinal Ag(977) with atomically precise edge geometry. Each phase revealed an oscillation in LDOS along the nanoribbon length (Friedel oscillations) [19, 119, 120]. However, the passivation of Bo nanoribbons and controlling their lateral segregation require further investigation in future, also possibly by considering vicinal surfaces as suitable substrates. Nevertheless, our data showcase the possibility for a straightforward Bo nanoribbon fabrication route which is viable even for the air-exposed epitaxial boron systems. Further investigation is required, preferably by scanning probe spectroscopies, to gain deeper insight into the electronic structure of such quasi-1D quantum objects.

5.2 Li decoration of borophene

Li atoms, characterised by their small size (crystal radius ~ 0.90 Å) [121] and high reactivity, are to be used to study one route of the Bo chemical modification. Our interest is to investigate which scenario of the following is likely to take place as Li is deposited onto Bo/Ir: adsorption, intercalation or both, and how these configurations may affect the crystallography and electronic structure of epitaxial Bo.

We recorded the XPS spectra of Ir 4*f* (Fig. 5.8a bottom) and Li 1*s* regions (Fig. 5.8b bottom) for the pristine Bo/Ir sample as a reference for the forthcoming experiments. Surface and bulk components of the Ir 4*f* peaks appear at the following binding energies: 60.33, 60.80 eV, and 63.33, 63.80 eV, respectively, in agreement with the values reported earlier in Section 4.1. Given that the surface component of the Ir 4*f* peak is suppressed in the presence of the Bo overlayer [99], we may conclude that Bo coverage on the surface was less than a monolayer. Based on the surface component intensity, we estimate the Bo coverage to be ~ 0.8 ML. Afterwards, Li was deposited sequentially via Li evaporation from an SAES getter at an applied current $I = 7$ A whereas the Bo/Ir sample was kept at room temperature (RT). Ir 4*f* and Li 1*s* spectra were recorded after each step of Li deposition *i.e.* after 3, 6 and 15 minutes of cumulative deposition time. Continuous decrease in the surface component (SC) area of Ir 4*f* peak is noticeable as more Li is deposited. There is a total reduction in SC by 16% after 15 minutes of Li deposition. The presence of Li is evidenced by XPS spectra (Fig. 5.8b) revealing the characteristic Li 1*s* peak, recorded 3 minutes of Li deposition, appearing at 55.87 eV, which is a slightly higher binding energy than what has been reported for Li on graphene [122] and Li on hBN [123]. A total shift of 0.3 eV towards a lower E_B, growth in the peak intensity along with peak broadening were observed after the fifteen-minute Li deposition. The shift towards lower binding energies is consistent with earlier reports for Li on graphite systems [122]. The Li coverage of Bo in monolayers (ML), θ_{Li}, was estimated from the recorded XPS data by introducing corrections such as atomic subshell photoionization cross-section σ and integral of the spectral peak [124] (see Section 2.4 for details of θ_{Li} quantification). Li dosing for 3 minutes resulted in $\theta_{Li} \approx 0.9$ ML, total 6 minutes yielded 1.8 ML and after 15 minutes of total deposition time $\theta_{Li} \approx 4.7$ ML.

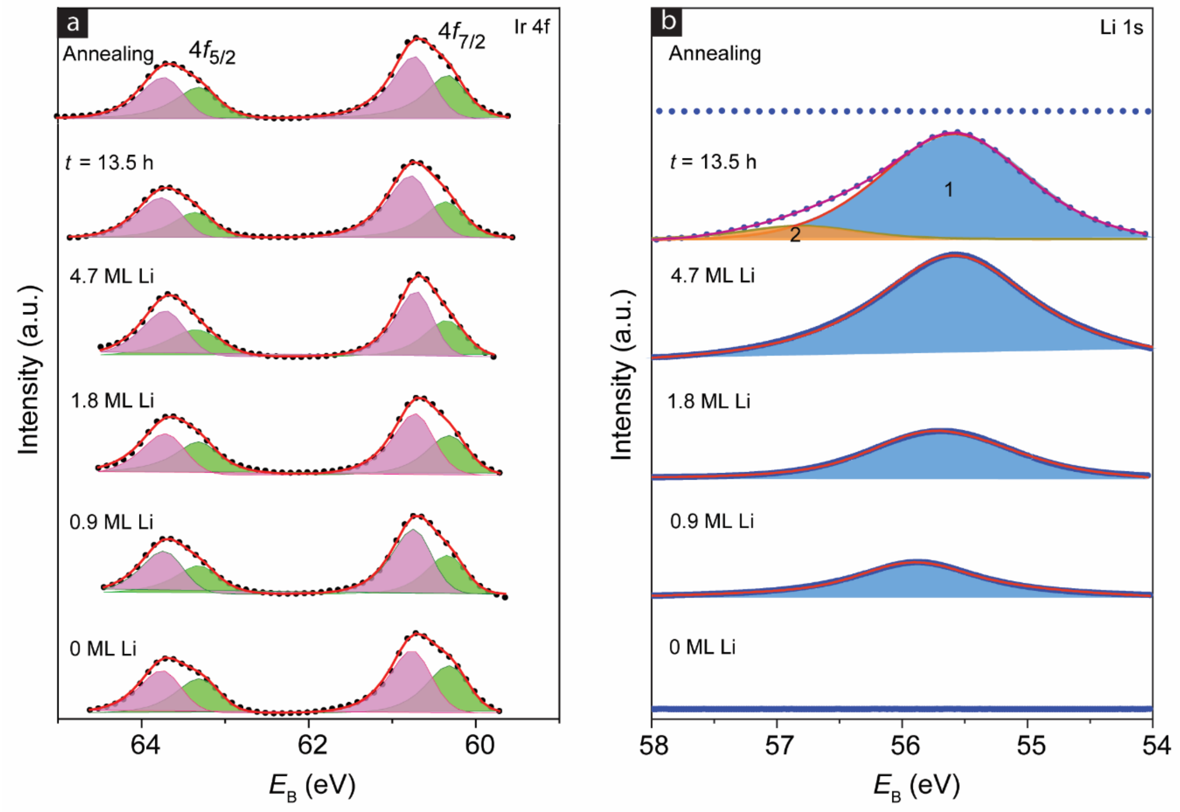

Figure 5.8 Core-level spectra before, during and after step-wise Li decoration of Bo/Ir. (a) Ir 4*f* spectra reveal surface and bulk components labelled with different colours. (b) Li 1*s* spectra. The peak shifts to a lower binding energy as more Li is deposited. Ageing causes peak broadening and emergence of a new component ascribed to Li oxide species. Annealing the sample at 1100 °C for three minutes removes all Li atoms. The spectra were recorded with *p*-polarized light at $h\nu = 100$ eV.

After the final Li deposition step, the sample was left in UHV for 13.5 hours. Such ageing renders additional 10% drop in the area of SC compared to the area of SC of the Ir 4*f* spectrum acquired at the end of Li deposition. The area reduction is presumably the effect of adsorbates bound to the bare Ir surface. Ageing also resulted in Li 1*s* peak broadening indicating chemical change in the sample: peak 2 in Fig. 5.8b appearing at 56.81 eV may be attributed to Li oxide species of variable stoichiometry since it is known from literature that Li_2O peak appears at 56.40 eV while Li_2O_2 peak appears at 57.51 eV of binding energy [125, 126]. The sample ageing renders ~ 0.1 eV shift in peak 1 towards a higher E_B while the peak width remains intact. Peak 1 may be ascribed to either unoxidized Li or Li bound to Bo. The large width of peak 1 is likely to arise from an average of several chemical configurations of Li on the surface, however, individual components could not be resolved in our measurements. When comparing the areas under the curves before and after ageing, we presume that ~ 9% of Li underwent oxidation in 13.5 hours. Annealing the sample at 1100 °C for three minutes removed all Li atoms adsorbed on Bo/Ir as revealed by the noise in Li 1*s* region in Fig. 5.8b (top), void of any detectable peak. It is noteworthy that the noise in the 0 ML Li (bottom) and annealing spectra (top) are seemingly dotted lines rather than scattered points because the intensity scales for all the spectra have been reset to be the same. Also, the number of the acquired data points for Li 1*s* spectra shown in Fig. 5.8b are not the same (*i.e.* different number of XPS scans) given the time limitation during synchrotron beamtime.

The formation of 4.7 ML Li gives rise to several components in the B 1*s* spectrum. The first peak was fitted with three components B_0, B_1+B_2 and B_3 with a major contribution of B_1+B_2 component (Fig. 5.9, bottom) at 188.66 eV. The spectrum indicates a change in the chemical environment of B atoms in the Bo sheet due to the deposited Li, and it is no longer possible to discern the individual B_1 and B_2 components visible in Fig. 4.1b. Hence, we use the B_1+B_2 component in Li-decorated samples to jointly address modifications of the peaks which were detected in pristine Bo. An important factor triggering the chemical modifications of Bo is linked to a charge transfer from Li to B and creation of various Li-B-O complexes. The B_0 and B_3 components of the first peak appearing at 187.60 eV and 189.80 eV, respectively, may be ascribed to a reduced state of boron oxide B_xO ($1< x \leq 6$) [127, 128]. One may not exclude the possibility of lithium boride (Li_xB_y) formation, which might also have a minor contribution at ~188 eV to the B_0 component . Additionally, the second peak at 191.85 eV indicates the formation of B_xO_y during the relatively short Li deposition experiment. The formation of boron oxides seems to be accelerated, in comparison to Li-free Bo samples, due to the reactivity of Li atoms which can facilitate production of highly reactive O atoms from residual O_2 molecules present in the UHV environment. Indeed, upon ageing for additional 2.5 hours (Fig. 5.9, top) inside the UHV chamber at a base pressure of ~ 10^{-10} mbar, Li expedites further Bo oxidation yielding a large B_xO_y peak and the formation of other B- / C- oxides (BC_xO_y) revealed by the two minor components at 190.50 and 191.35 eV [99, 112].

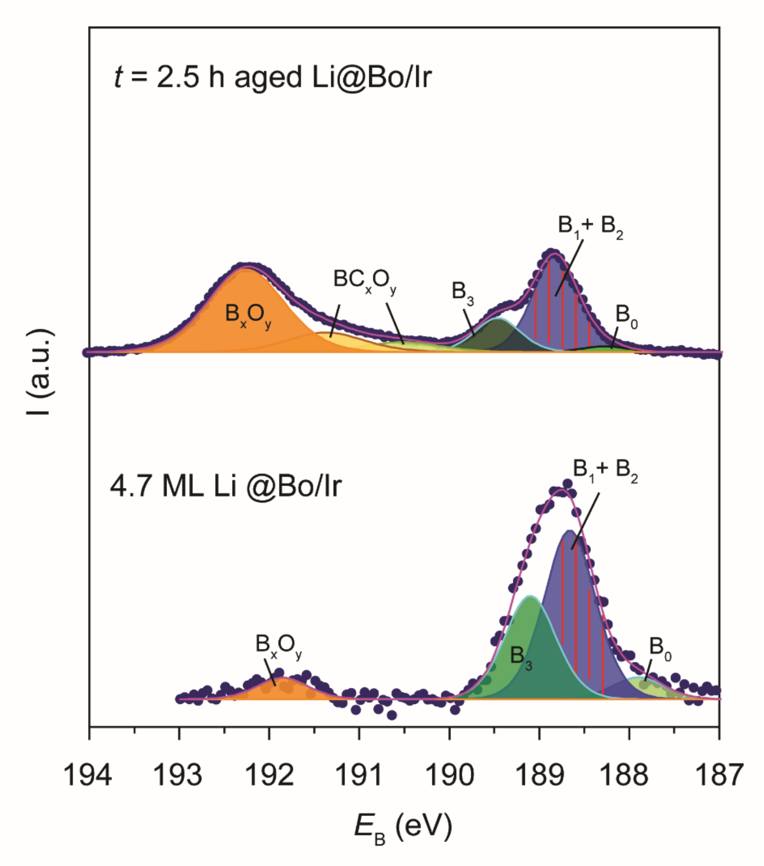

Figure 5.9 XPS of the B 1*s* region (a) after 4.7 ML Li deposition and (b) additional ageing for 2.5 hours in UHV. Emergence of three boron oxide peaks (B_0, B_3, B_xO_y) and the mixing of B_1 and B_2 components is attributed to the Li effect on Bo. *In-situ* ageing (top) gives rise to additional boron oxide peaks of various stoichiometries.

Besides the core-level investigation via XPS, crystallography of the Li-decorated samples described up to now was examined with electron diffraction. Since XPS spectra indicate the presence of uncovered Ir on the sample, the first step was to study possible structures of Li on bare Ir. Sequential LEED patterns, therefore, were recorded to study the evolution of Li superstructures onto bare Ir(111) in order to have a reference guideline for subsequent, more complicated experiments which involve Bo. The LEED pattern displayed in Fig. 5.10a results from averaging over a sequence of patterns acquired over 45-minute time span of Li deposition totalling to θ_{Li} ≈ 1.6 ML. Overall, two well-defined Li superstructures formed: (1.31 × 1.31)R10.89° and (2√3 × 2√3)R30° as schematically shown in Fig. 5.10b-c. Also, additional superstructures exhibiting faint and/or blurred diffraction spots were detected which indicate poor Li ordering on the sample surface.

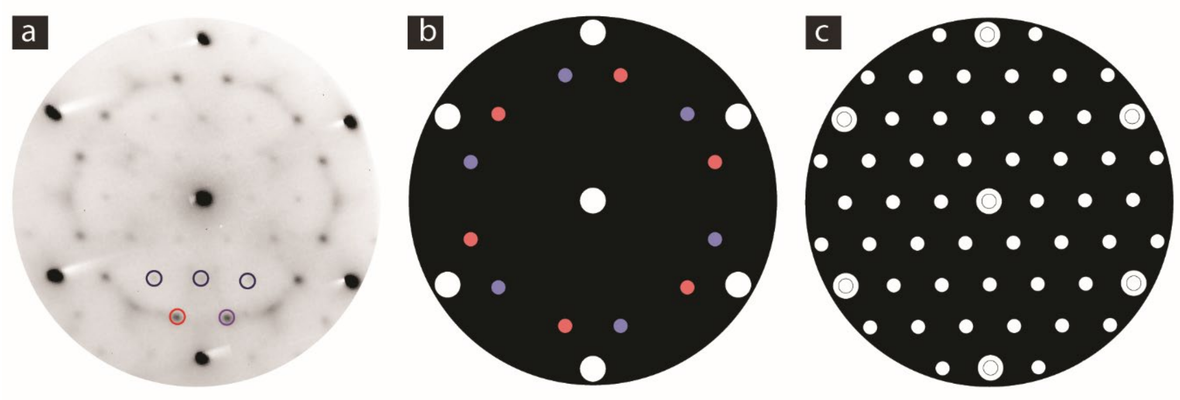

Figure 5.10 Two well-defined Li superstructures with respect to Ir (111) at θ_{Li} ≈ 1.6 ML. (a) An averaged LEED pattern generated from a sequence of patterns recorded at 40 eV throughout the Li deposition for 45 minutes. The pattern reveals the Li superstructures (2√3 × 2√3)R30° (blue circles) and (1.31 × 1.31)R10.89° in two rotational domains (red and purple circles). The corresponding simulations of superstructures (generated by LEEDpat software) are shown for (b) (1.31 × 1.31)R10.89° superlattice in two rotational domains marked with red and purple spots and (c) (2√3 × 2√3)R30° superlattice.

In the following, we proceed with the examination of the crystallography of Li deposited onto Bo/Ir(111). The LEED patterns displayed in Figs. 5.11a, b, d and e can be related to the Li 1*s* spectra shown in Fig. 5.8b. At θ_{Li} ~ 0.9 ML, a superstructure identified as (12 × 12) is visible in the LEED data shown in Fig. 5.11b. Apparently, that superstructure bears no resemblance to the ones found during Li deposition on bare Ir(111), displayed in Fig. 5.10a, indicating Bo involvement in its formation.

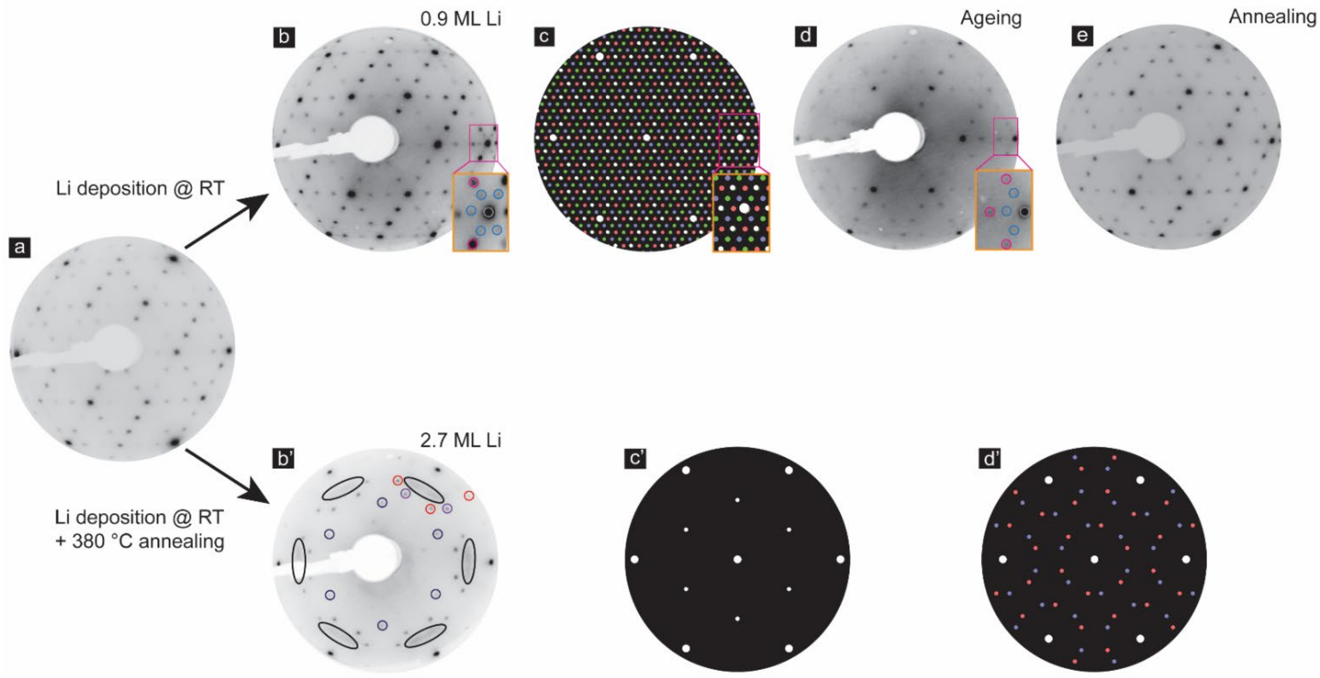

Figure 5.11 LEED patterns for different concentrations of Li on uniform Bo/Ir(111) (~ 0.8 ML). (a) Pristine Bo/Ir(111). (b-c) Li (12 × 12) superstructure at θ_{Li} ~ 0.9 ML and its LEEDpat simulation. The Li superstructure is marked with red, green and purple spots whereas the Bo pattern is indicated with white spots of the same size in both figures; the seven white spots of greater size indicate Ir pattern. (d) 13.5-hour aged sample. (e) Pristine Bo is retrieved after annealing. (b′) Two Li superstructures formed at θ_{Li} ~ 2.7 ML after one-minute annealing at 380°C: (√3×√3)*R*30° (blue circles) and √7 × √7 (magenta and purple circles mark two rotational domains). (c′-d′) The simulation of Li (√3 × √3)*R*30° and √7 × √7 superstructures, respectively. All patterns were acquired at *E* = 83 eV.

The decline in the LEED pattern intensity of 13.5-hour aged sample (Fig. 5.11d) may be attributed to the formation of adsorbates on the surface (see Fig. 5.9, top). In the follow-up control experiment, the sample was first flashed to 1100 °C to remove Li, however Li (12 × 12) superstructure was still there as revealed by LEED (not shown). Annealing the sample at 1100 °C for three minutes caused the disappearance of the (12 × 12) superstructure as revealed by LEED data in Fig. 5.11e. Also, no new traces of any Li superstructure were found, which indicates that the pristine Bo was retrieved. This is in agreement with the earlier XPS data in Fig. 5.8b which confirms removal of all Li atoms from Bo/Ir after such extended high temperature annealing. Alternatively, Li deposition onto Bo/Ir for 9 minutes at $I = 8$A ($\theta_{\mathrm{Li}} \sim 2.7$ ML) followed by moderate one-minute annealing at 380 °C resulted in the formation of two other identified Li superstructures presented in Fig. 5.11b′: $(\sqrt{3} \times \sqrt{3})R30°$ (marked with blue circles) and $\sqrt{7} \times \sqrt{7}$ (magenta and purple circles). Additionally, the six blurred streaks, marked with black oval shapes, in Fig. 5.11b′ might relate to the disordered Li (1.31 × 1.31)R10.89° superstructure formed at a lower coverage ($\theta_{\mathrm{Li}} \approx 1.6$ ML) on bare Ir (Fig. 5.10a). Interestingly, the Li superstructures displayed in Fig. 5.11b-b′ were obtained by varying Li concentration ($\theta_{\mathrm{Li}} = 0.9$ ML and 2.7 ML, respectively) and thermal treatment. Thus, our results imply that Li atomic positions depend on the abundance of Li atoms on the surface and the energy which is provided to the system via low-temperature annealing. Overall, Bo coverage, total amount of deposited Li atoms and the thermal treatment of the sample play a significant part in determining the resulting superstructure. Homogeneity of Li adsorption on the surface needs further investigation, including theoretical calculations, in order to fully understand the mechanism underlying the formation of different Li superstructures.

Valence band structure modifications upon Li deposition have been tracked with ARPES and are shown in panels (a-d) of Fig. 5.12. The data feature the characteristic surface state (Ir S_1) of Ir(111), marked with a white arrow at the Γ-point in the vicinity of the Fermi level as well as the Bo-induced replicated bands, marked with grey arrows, reported earlier in Section 4.2. Fig. 5.12a shows ARPES spectrum of pristine Bo/Ir(111), which was recorded immediately after Bo growth on bare Ir(111) and taken as a reference, where the binding energy of surface state (E_{ss}) appears at 0.35 eV below the Fermi level.

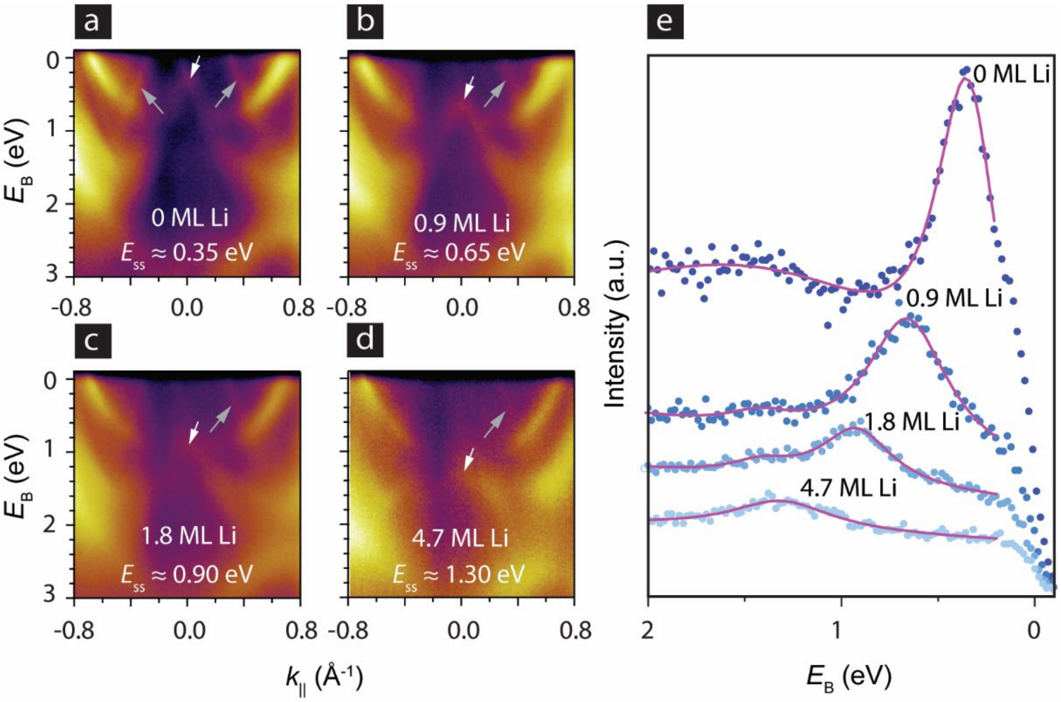

Figure 5.12 ARPES data of submonolayer Bo on Ir(111) decorated with Li. (a-d) Stepwise Li deposition gradually shifts Ir S_1 (indicated by a white arrow) to a higher binding energy. The Ir replicated band (grey arrow) remains visible after depositing 4.7 ML Li, although with lower intensity. (e) The corresponding EDCs were extracted from the displayed ARPES spectra at the Γ-point ($k_{||} = 0$ Å^{-1}). The total shift of Ir S_1 $\Delta E_{ss} \approx 1.30$ eV along with the reduction in its intensity are associated with Li adsorption. The spectra were recorded with p-polarized light at $h\nu = 100$ eV.

A comparison between panels (a) and (b) of Fig. 5.12, where the latter was recorded at θ_{Li} = 0.9 ML, reveals a considerable surface state shift towards a higher binding energy (to E_{ss} ≈ 0.65 eV below the Fermi level) whereas its intensity declines. The E_{ss} shifts further to ≈ 0.9 eV at θ_{Li} ≈ 1.84 ML and then to ≈ 1.30 eV at θ_{Li} ≈ 4.7 ML (Fig. 5.12c-d). The surface state intensity deteriorates considerably at θ_{Li} ≈ 4.7 ML. In addition, the intensity of both Bo-induced replicas and Ir energy bands are reduced as more Li is deposited. Reduction of the Ir surface state intensity is expected, since adsorbates are well known to disturb the coherence of these surface-localized electronic states [129]. Moreover, pile-up of Li atoms on top of the sample can cause attenuation of photoemission intensity of all electronic bands, including the surface state bands as well as the replica bands. However, considering that the replica intensity reduction is more pronounced than the reduction of other bands in the ARPES data, then it is reasonable to assume that deterioration of the Bo grating effect is taking place. We propose two possible scenarios for this: (i) random adsorption of Li on Bo sheet, causing Bo lattice disruption and decoherence of the diffracted electrons, or (ii) lifting of Bo sheet from Ir because of the intercalation as Li atoms go in between the Bo sheet and topmost Ir atoms, resulting in the Bo grating "flattening", hence the reduced diffraction effect.

Fig. 5.12e displays the corresponding energy distribution curves (EDCs), extracted from the ARPES data, where the expected response to the sequential introduction of Li is evident. Continuous broadening of the Γ-point peak of EDC as more Li is deposited and a total energy shift by ≈ 1.30 eV at θ_{Li} ≈ 4.7 ML are both pronounced. Both the shift and broadening of surface states are hallmarks of reduced momentum coherence [130] induced by the alkali metal. Pervan *et al.* reported a similar shift in the Ir surface state at the K-point and decrease in the peak spectral intensity of EDCs for disordered Li phase on bare Ir(111) which result from the hybridization between Li states and Ir surface state [129]. However, when they investigated disordered Li phase on graphene/Ir, only the energy shift without a decline in the spectral intensity was detected. The latter observation arises from the fact that graphene, unlike Bo, blocks the incoherent scattering of Ir surface state electrons by exhausting DOS of Li, which would otherwise hybridise with Ir surface state causing its momentum decoherence [129].

Considering the fact that Bo coverage on Ir(111) for the data shown in Fig. 5.12 was lower than 1 ML (~ 0.8 ML), the Ir S_1 shift caused by Li might be due to direct adsorption of Li atoms onto uncovered Ir terraces and/or intercalation of Li at the Bo-Ir interface. The latter scenario may be explained by diffusion of Li atoms through the HH of Bo sheet, as the Li ion size (~ 0.9 Å) [121] is smaller than the HH size (1.5 Å), whereas diffusion through Bo triangular lattice sites is unlikely to happen due to their small size.

Aside from the Brillouin zone centre and vicinity of the Fermi level, the valence band structure near the K-point and down to 10 eV of binding energy, was recorded for the pristine Bo/Ir and the lithiated Bo/Ir ($\theta_{\mathrm{Li}} \approx 4.7$ ML) samples. The panels in Fig. 5.13 display the ARPES spectra along with the EDCs extracted from them at $k_{\|} = 1.2$ Å^{-1}. The Ir surface state (Ir S_2) at the K-point shifts farther from the Fermi level by 0.12 eV towards a higher E_B. (Fig. 5.13d). In addition, by comparing the insets in (a) and (b) in Fig. 5.13, where the contrast has been readjusted for a better visibility of the low-intensity feature, a non-dispersing band (indicated by a white arrow) is observed at 8.8 eV in the latter inset. This new band gives rise to the small peak appearing at the same energy in the extracted EDC shown in Fig. 5.13d (marked with a black arrow) which is absent in Fig. 5.13c. The flat band may be ascribed to the formation of oxide species promoted by the adsorbed Li on top of Bo [131], in line with the XPS data shown in Fig. 5.8b. One may consider the observation of such a band a proof that Li adsorption occurred on top of the sample and that Li intercalation at the Bo/Ir interface is less probable. Had all Li atoms been intercalated between Bo and Ir atoms, Li atoms would likely have been screened off from oxygen atoms existing in the UHV environment, in such a way that the flat band would not have formed. However, to further elucidate the likelihood of these different Li geometries (adsorption vs. intercalation) on Bo/Ir, dedicated STM and DFT studies are planned in the future.

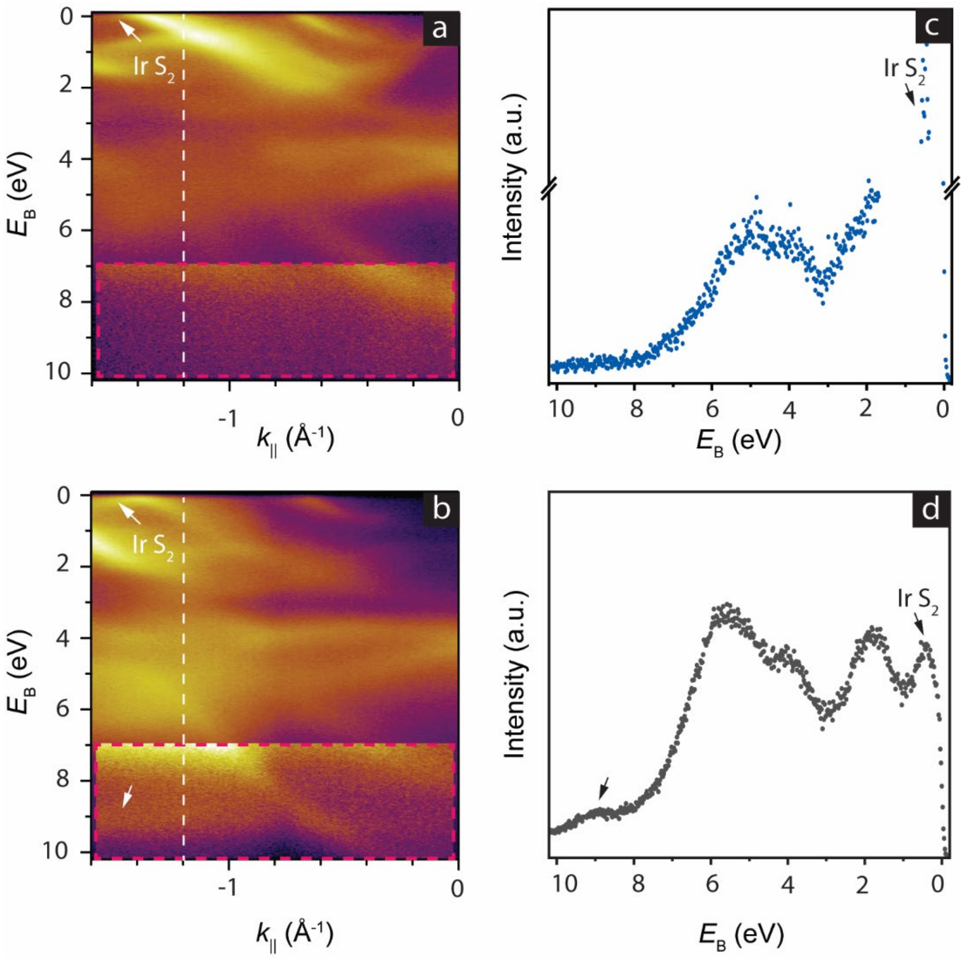

Figure 5.13 ARPES spectra of Bo/Ir before (a) and after deposition of 4.7 ML of Li (b). The corresponding EDCs extracted at $k_{||}$ = 1.2 Å^{-1} are displayed in (c-d). A flat band (white arrow) appears at E_B = 8.8 eV (b) after Li deposition. Brightness and contrast were enhanced in the E_B range 7 – 10 eV (inset, marked by dashed rectangles) for a better visibility of ARPES spectra. The spectra were acquired with *p*-polarized light at $h\nu$ = 100 eV.

5.3 Summary

Observed changes in B 1*s* peak arising from Bo binding to residual C- and/or O-containing chemical species in the UHV chamber indicate the high reactivity of epitaxial Bo. When the XPS spectral intensities of B 1*s* peak, recorded during the sample ageing were compared, it was estimated that ~ 1/3 of B atoms in the Bo sheet were bound to the residual molecules in the chamber after 22 hours. Thus, B atoms undergo chemical changes as the time passes, however the extent of the changes depends on how strong they are bound to the Ir atoms. Li was found to promote oxidation of Bo as it reacts with residual chemical species in the UHV and is known to efficiently crack O_2 molecules into reactive O atoms. An aged Li/Bo/Ir sample showed a pronounced effect of Li-promoted oxidation as signalled by the huge B-O peak in the XPS data.

High-temperature annealing (1200 > T > 1000 °C) enables the dissolution-segregation mechanism of B atoms by which pristine Bo is retrieved from aged, *i.e.* contaminated samples. In addition to temperature, the time duration of the annealing needed to trigger B dissolution is a crucial parameter, since it takes a few minutes to obtain pristine Bo from in-situ aged samples. However, to retrieve Bo from ex-situ aged samples, it takes longer time, tens of minutes, due to the high surface coverage of various adsorbates which is the consequence of the sample exposure to air. While utilizing dissolution-segregation steps to retrieve pristine Bo, partial loss of B atoms is expected, thus resulting in reduced Bo coverage after each step.

Decoration of pristine Bo with Li at room temperature in UHV environment gives rise to a variety of Li superstructures which depend on the concentration of deposited Li and thermal treatment of the system afterwards. Li adatoms piling up on the surface may either cause the decoherence of the diffracted electrons and/or diffuse through the Bo sheet hexagonal holes lifting Bo sheet from Ir, thus causing intercalation.

The mere decline in the intensity of the surface state at Γ-point and of the other Ir energy bands after Li deposition, is not conclusive evidence for the most likely dynamics scenario of Li atoms: adsorption on top of Bo sheet or intercalation between Bo and Ir. However, one may assume that Li adsorption on top of Bo/Ir is more likely considering the flat energy band in the valence band spectra which can be assigned to oxidized Li on top of Bo. Therefore, the homogeneity and regularity of Li adsorption calls for further theoretical and experimental studies.

6 Conclusions and outlook

The investigated samples of monolayer Bo χ_6 polymorph presented in this thesis were grown on Ir(111) via boron dissolution-segregation route using borazine as a precursor (Section 3.1). The advantage of this route of choice over other synthesis approaches is the high and uniform coverage (up to 1 ML) of Ir terraces with a Bo monolayer, as revealed by LEEM data. Also, the utilized growth method diminishes the probability of B clusters formation either on formed Bo patches or bare regions of the substrate, and minimises the number of grain boundaries and other defects within the Bo.

The experimental data and theoretical calculations for pristine Bo/Ir(111) system provided in Chapter 4 reveal nanoscopic and unidirectional modulation exhibited by monolayer Bo sheet on the Ir substrate. This modulation originates from the inhomogeneity in Bo-Ir binding demonstrated by two well-resolved B 1*s* XPS peaks and spatial variation of Ir surface state coherency, which consequently yield Ir band replication (*i.e.* Umklapp process) observed close to Fermi level in the ARPES spectra of the system. To add, the overall Bo-Ir binding is of considerable strength in comparison with weakly-bound graphene on Ir, as evidenced by the decline of surface components of Ir 4*f* doublet in the respective XPS spectrum. Overall, the Bo-sheet also acts as an electron diffraction (scattering) grating due to its stripe-like morphology which arises from the Bo-Ir binding modulation.

The pristine structure of Bo, demonstrated considerable chemical (re)activity even in vacuum environment: it was estimated from the XPS spectra that 1/3 of B atoms of the Bo sheet were bound to residual contaminants (C- and O- containing chemical species) after 22 hours of ageing in UHV (Section 5.1). Therefore, pristine Bo, driven by the electron deficiency of its constituent B atoms, readily reacts with the surrounding atoms and molecules. However, the pristine Bo structure is easily retrievable after *in situ* and to a certain extent after *ex situ* ageing through high-temperature annealing (1200 ≥ T > 1000 °C) thanks to the dissolution-segregation mechanism, during which B atoms reassemble into a fresh Bo mesh on the Ir surface. The downside of such a protocol is the decrease of resultant Bo coverage due to the loss of B atoms during the substrate annealing.

Decoration of pristine Bo with Li at room temperature in a UHV environment gave rise to a variety of Li superstructures depending on the concentration of deposited Li and thermal treatment of the system afterwards (Section 5.2). The mere decline in the intensity of the ARPES spectrum after Li deposition, in conjunction with other experimental data, does not provide conclusive evidence for the most likely scenario of Li atoms dynamics: adsorption on top of Bo sheet or intercalation between Bo and Ir. However, the Li adsorption scenario seems to be more probable due to the observed non-dispersing electronic band close to the Fermi level, which may pinpoint oxide formation promoted by Li atoms lying atop the Bo sheet. Bo decoration with other alkali metal atoms such as Cs is proposed for future studies, due to their relatively large crystal radii, which would enable a comparison with much smaller Li atoms addressed herein. In such way, further details about alkali-Bo interaction would be clarified and possible routes for dedicated alkali-based Bo modifications proposed.

The chemical stability and environmental inertness of a material are crucial factors as far as applicative aspects are considered. One grand challenge in the borophenes research, as demonstrated in the thesis, is their instability due to high reactivity. Deliberate oxidation and hydrogenation of Bo on silver, for instance, have reportedly demonstrated improved Bo stability in non-pristine form and the retrievability of pristine Bo upon annealing. In line with this strand, chemical tuneability of Bo should be further investigated as a potential route for stabilising Bo and tailoring its properties. In another approach, enhancement of Bo stability may also be achieved by coupling it with another inert 2D material like hBN or graphene, thus forming a vertical heterostructure such as hBN-Bo or graphene-Bo. This direction awaits further exploration and requires refinement of currently available synthesis protocols and development of methods for the transfer of such heterostructures to substrates of choice.

By examining even further the possibilities of layer stacking in the vertical direction, bilayer Bo systems inevitably come into play. Bilayer samples have been experimentally realised on some metal substrates, however bilayer Bo on Ir(111) remains unexplored system to date. The investigation of bilayer Bo grown on Ir may enable thorough study of the intrinsic electronic properties of pristine Bo χ_6 polymorph, which is a step further towards better modelling of various Bo-based applications. In addition, future realisation of multilayer Bo may serve as a Bo stabilisation route, *i.e.* a form of its homogeneous encapsulation, however this research direction still faces many challenges due to the complex boron chemistry and boron's intrinsic hindrance to exist in 2D form. Finally, the predicted superconductivity in intercalated bilayer Bo is still to be experimentally realised and may expand the investigation of many-body effects in 2D materials, thus expediting the development of boron-based 2D superconductors.

Bibliography

[1] P. Pervan, M. Milun, and R. Brako, ‘Quantum Well States in Metallic Films, Wires, and Dots’, *Surface and Interface Science: Solid-Solid Interfaces and Thin Films: Volume 4*, pp. 493–544, 2014, doi: 10.1002/9783527680566.ch21.

[2] K. S. Novoselov *et al.*, ‘Two-dimensional atomic crystals’, *Proc Natl Acad Sci USA*, vol. 102, no. 30, pp. 10451–10453, 2005, doi: 10.1073/pnas.0502848102.

[3] K. S. Novoselov *et al.*, ‘Electric field in atomically thin carbon films’, *Science*, vol. 306, no. 5696, pp. 666–669, 2004, doi: 10.1126/science.1102896.

[4] A. K. Geim and K. S. Novoselov, ‘The rise of graphene’, *Nature Mater*, vol. 6, no. 3, pp. 183–191, 2007, doi: 10.1038/nmat1849.

[5] K. I. Bolotin *et al.*, ‘Ultrahigh electron mobility in suspended graphene’, *Solid State Commun*, vol. 146, no. 9–10, pp. 351–355, 2008, doi: 10.1016/J.SSC.2008.02.024.

[6] J. H. Gosling *et al.*, ‘Universal mobility characteristics of graphene originating from charge scattering by ionised impurities’, *Commun Phys*, vol. 4, no. 1, pp. 1–8, 2021, doi: 10.1038/s42005-021-00518-2.

[7] X. Peng and R. Ahuja, ‘Symmetry breaking induced bandgap in epitaxial graphene layers on SiC’, *Nano Lett*, vol. 8, no. 12, pp. 4464–4468, 2008, doi: 10.1021/nl802409q.

[8] I. Meric, M. Y. Han, A. F. Young, B. Ozyilmaz, P. Kim, and K. L. Shepard, ‘Current saturation in zero-bandgap, top-gated graphene field-effect transistors’, *Nat Nanotech*, vol. 3, no. 11, pp. 654–659, 2008, doi: 10.1038/nnano.2008.268.

[9] X. Li *et al.*, ‘Graphene and related two-dimensional materials: Structure-property relationships for electronics and optoelectronics’, *Appl Phys Rev*, vol. 4, no. 2, 2017, doi: 10.1063/1.4983646/279721.

[10] E. S. Penev, N. Marzari, and B. I. Yakobson, ‘Theoretical prediction of two-dimensional materials, behavior, and properties’, *ACS Nano*, vol. 15, no. 4, pp. 5959–5976, 2021, doi: 10.1021/acsnano.0c10504.

[11] N. Briggs *et al.*, ‘A roadmap for electronic grade 2D materials’, *2D Mater*, vol. 6, no. 2, p. 022001, 2019, doi: 10.1088/2053-1583/AAF836.

[12] N. R. Glavin *et al.*, ‘Emerging Applications of Elemental 2D Materials’, *Adv Mater*, vol. 32, no. 7, pp. 1–22, 2020, doi: 10.1002/adma.201904302.

[13] J. Shi *et al.*, ‘THz photonics in two dimensional materials and metamaterials: properties, devices and prospects’, *J Mater Chem C Mater*, vol. 6, no. 6, pp. 1291–1306, 2018, doi: 10.1039/C7TC05460B.

[14] Q. Qiu, Z. Huang, Q. Qiu, and Z. Huang, ‘Photodetectors of 2D materials from ultraviolet to terahertz waves’, *Adv Mater*, vol. 33, no. 15, p. 2008126, 2021, doi: 10.1002/adma.202008126.

[15] C. X. Zhao and J. F. Jia, ‘Stanene: a good platform for topological insulator and topological superconductor’, *Front Phys*, vol. 15, no. 5, 2020, doi: 10.1007/S11467-020-0965-5.

[16] L. Daukiya *et al.*, ‘Functionalization of 2D materials by intercalation’, *Prog Surf Sci*, vol. 94, no. 1, pp. 1–20, 2019, doi: 10.1016/j.progsurf.2018.07.001.

[17] X. Wang and H. Dai, ‘Etching and narrowing of graphene from the edges’, *Nat Chem*, vol. 2, no. 8, pp. 661–665, 2010, doi: 10.1038/nchem.719.

[18] C. Chen *et al.*, ‘Sub-10-nm graphene nanoribbons with atomically smooth edges from squashed carbon nanotubes’, *Nat Electron*, vol. 4, no. 9, pp. 653–663, 2021, doi: 10.1038/s41928-021-00633-6.

[19] Q. Li, L. Wang, H. Li, M. K. Y. Chan, and M. C. Hersam, ‘Synthesis of quantum-confined borophene nanoribbons’, *ACS Nano*, vol. 18, no. 1, pp. 483–491, 2024, doi: 10.1021/acsnano.3c08089.

[20] J. Cheng *et al.*, Phosphorene two-dimensional black phosphorus nanomaterials: Emerging advances in electrochemical energy storage science,

Nano-Micro Lett, vol. 12, no. 1. Springer Singapore, 2020, doi: 10.1007/s40820-020-00510-5.

[21] J. Nevalaita and P. Koskinen, 'Atlas for the properties of elemental two-dimensional metals', *Phys. Rev. B*, vol. 97, no. 3, p. 035411, 2018, doi: 10.1103/physrevb.97.035411.

[22] S. Bin Mujib, Z. Ren, S. Mukherjee, D. M. Soares, and G. Singh, 'Design, characterization, and application of elemental 2D materials for electrochemical energy storage, sensing, and catalysis', *Mater Adv*, vol. 1, no. 8, pp. 2562–2591, 2020, doi: 10.1039/d0ma00428f.

[23] A. Molle, J. Yuhara, Y. Yamada-Takamura, and Z. Sofer, 'Synthesis of Xenes: physical and chemical methods', *Chem Soc Rev*, vol. 54, no. 4, pp. 1845–1869, 2025, doi: 10.1039/D4CS00999A.

[24] A. J. Mannix, B. Kiraly, M. C. Hersam, and N. P. Guisinger, 'Synthesis and chemistry of elemental 2D materials', *Nat Rev Chem*, vol. 1, pp. 1–15, 2017, doi: 10.1038/s41570-016-0014.

[25] Y. C. Lin *et al.*, 'Recent advances in 2D material theory, synthesis, properties, and applications', *ACS Nano*, vol. 17, no. 11, pp. 9694–9747, 2023, doi: 10.1021/acsnano.2c12759.

[26] Z. Zhang, E. S. Penev, and B. I. Yakobson, 'Polyphony in B flat', *Nat Chem*, vol. 8, no. 6, pp. 525–527, 2016, doi: 10.1038/nchem.2521.

[27] M. Corso, W. Auwärter, M. Muntwiler, A. Tamai, T. Greber, and J. Osterwalder, 'Boron Nitride Nanomesh', *Science*, vol. 303, no. 5655, pp. 217–220, 2004, doi: 10.1126/science.1091979.

[28] R. R. Zope, T. Baruah, K. C. Lau, A. Y. Liu, M. R. Pederson, and B. I. Dunlap, 'Boron fullerenes: From B_{80} to hole doped boron sheets', *Phys Rev B*, vol. 79, no. 16, pp. 1–4, 2009, doi: 10.1103/PhysRevB.79.161403.

[29] X. Wu, J. Dai, Y. Zhao, Z. Zhuo, J. Yang, and X. C. Zeng, 'Two-dimensional boron monolayer sheets', *ACS Nano*, vol. 6, no. 8, pp. 7443–7453, 2012, doi: 10.1021/nn302696v.

[30] E. S. Penev, S. Bhowmick, A. Sadrzadeh, and B. I. Yakobson, ‘Polymorphism of two-dimensional boron’, *Nano Lett*, vol. 12, no. 5, pp. 2441–2445, 2012, doi: 10.1021/nl3004754.

[31] Y. Liu, E. S. Penev, and B. I. Yakobson, ‘Probing the synthesis of two-dimensional boron by first-principles computations’, *Angew Chem*, vol. 52, no. 11, pp. 3156–3159, 2013, doi: 10.1002/anie.201207972.

[32] E. S. Penev, A. Kutana, and B. I. Yakobson, ‘Can two-dimensional boron superconduct?’, *Nano Lett*, vol. 16, no. 4, pp. 2522–2526, 2016, doi: 10.1021/acs.nanolett.6b00070.

[33] Z. Zhang, E. S. Penev, and B. I. Yakobson, ‘Two-dimensional boron: structures, properties and applications’, *Chem Soc Rev*, vol. 46, no. 22, pp. 6746–6763, Nov. 2017, doi: 10.1039/C7CS00261K.

[34] H. Tang and S. Ismail-Beigi, ‘Novel precursors for boron nanotubes: the competition of two-center and three-center bonding in boron sheets’, *Phys Rev Lett*, vol. 99, no. 11, p. 115501, 2007, doi: 10.1103/PhysRevLett.99.115501.

[35] X. Liu, M. S. Rahn, Q. Ruan, B. I. Yakobson, and M. C. Hersam, ‘Probing borophene oxidation at the atomic scale’, *Nanotechnology*, vol. 33, no. 23, p. 235702, 2022, doi: 10.1088/1361-6528/AC56BD.

[36] A. Mazaheri, M. Javadi, and Y. Abdi, ‘Chemical vapor deposition of two-dimensional boron sheets by thermal decomposition of diborane’, *ACS Appl Mater Interfaces*, vol. 13, no. 7, pp. 8844–8850, 2021, doi: 10.1021/acsami.0c22580.

[37] B. Radatović *et al.*, ‘Macroscopic single-phase monolayer borophene on arbitrary substrates’, *ACS Appl Mater Interfaces*, vol. 14, no. 18, pp. 21727–21737, 2022, doi: 10.1021/acsami.2c03678.

[38] X. Zhang, J. Hu, Y. Cheng, H. Y. Yang, Y. Yao, and S. A. Yang, ‘Borophene as an extremely high capacity electrode material for Li-ion and Na-ion batteries’, *Nanoscale*, vol. 8, no. 33, pp. 15340–15347, 2016, doi: 10.1039/c6nr04186h.

[39] B. Mortazavi, A. Dianat, O. Rahaman, G. Cuniberti, and T. Rabczuk, ‘Borophene as an anode material for Ca, Mg, Na or Li ion storage: A first-principle study’, *J Power Sources*, vol. 329, pp. 456–461, 2016, doi: 10.1016/j.jpowsour.2016.08.109.

[40] J. Yu, M. Zhou, M. Yang, Q. Yang, Z. Zhang, and Y. Zhang, ‘High-Performance Borophene/Graphene Heterostructure Anode of Lithium-Ion Batteries Achieved via Controlled Interlayer Spacing’, *ACS Appl Energy Mater*, vol. 3, no. 12, pp. 11699–11705, 2020, doi: 10.1021/acsaem.0c01808.

[41] A. J. Mannix *et al.*, ‘Synthesis of borophenes: Anisotropic, two-dimensional boron polymorphs’, *Science*, vol. 350, no. 6267, pp. 1513–1516, 2015, doi: 10.1126/science.aad1080.

[42] B. Feng *et al.*, ‘Experimental realization of two-dimensional boron sheets’, *Nat Chem*, vol. 8, no. 6, pp. 563–568, 2016, doi: 10.1038/nchem.2491.

[43] B. Kiraly *et al.*, ‘Borophene Synthesis on Au(111)’, *ACS Nano*, vol. 13, no. 4, pp. 3816–3822, 2019, doi: 10.1021/acsnano.8b09339.

[44] R. Wu, A. Gozar, and I. Božović, ‘Large-area borophene sheets on sacrificial Cu(111) films promoted by recrystallization from subsurface boron’, *NPJ Quantum Mater*, vol. 4, no. 1, pp. 1–6, 2019, doi: 10.1038/s41535-019-0181-0.

[45] P. Ranjan, J. M. Lee, P. Kumar, and A. Vinu, ‘Borophene: new sensation in flatland’, *Adv Mater*, vol. 32, no. 34, pp. 1–13, 2020, doi: 10.1002/adma.202000531.

[46] H. Li *et al.*, ‘Scalable Production of Few-Layer Boron Sheets by Liquid-Phase Exfoliation and Their Superior Supercapacitive Performance’, *ACS Nano*, vol. 12, no. 2, pp. 1262–1272, 2018, doi: 10.1021/acsnano.7b07444.

[47] M. G. Cuxart *et al.*, ‘Borophenes made easy’, *Sci Adv*, vol. 7, no. 45, p. 1490, 2021, doi: 10.1126/sciadv.abk1490/.

[48] K. M. Omambac *et al.*, ‘Segregation-enhanced epitaxy of borophene on Ir(111) by Thermal Decomposition of Borazine’, *ACS Nano*, vol. 15, no. 4, pp. 7421–7429, 2021, doi: 10.1021/acsnano.1c00819.

[49] N. R. Innis, C. Marichy, C. Journet, and C. Bousige, ‘Borophene bottom-up syntheses: a critical review’, *2D Mater*, vol. 12, no. 2, p. 022005, 2025, doi: 10.1088/2053-1583/adafbf.

[50] Q. Li, E. B. Aklile, A. Tsui, and M. C. Hersam, ‘Progress and future directions in borophene research’, *Nat Chem*, vol. 17, no. 5, pp. 642–652, 2025, doi: 10.1038/s41557-025-01773-4.

[51] S. Ajmal *et al.*, ‘realizing electrochemical energy conversion and storage with borophene: science, engineering, obstacles, and future opportunities’, *Small*, vol. 21, no. 10, p. 2411311, 2025, doi: 10.1002/smll.202411311.

[52] C. Chen *et al.*, ‘Synthesis of bilayer borophene’, *Nat Chem*, vol. 14, no. 1, pp. 25–31, 2022, doi: 10.1038/s41557-021-00813-z.

[53] Z. Zhang, Y. Yang, G. Gao, and B. I. Yakobson, ‘Two-dimensional boron monolayers mediated by metal substrates’, *Angew Chem*, vol. 127, no. 44, pp. 13214–13218, 2015, doi: 10.1002/ange.201505425.

[54] R. Wu *et al.*, ‘Large-area single-crystal sheets of borophene on Cu(111) surfaces’, *Nat Nanotech*, vol. 14, no. 1, pp. 44–49, 2019, doi: 10.1038/s41565-018-0317-6.

[55] N. A. Vinogradov, A. Lyalin, T. Taketsugu, A. S. Vinogradov, and A. Preobrajenski, ‘Single-phase borophene on Ir(111): formation, structure, and decoupling from the support’, *ACS Nano*, vol. 13, no. 12, pp. 14511–14518, 2019, doi: 10.1021/acsnano.9b08296.

[56] A. B. Preobrajenski, A. Lyalin, T. Taketsugu, N. A. Vinogradov, and A. S. Vinogradov, ‘Honeycomb Boron on Al(111): from the concept of borophene to the two-dimensional boride’, *ACS Nano*, vol. 15, no. 9, pp. 15153–15165, 2021, doi: 10.1021/acsnano.1c05603.

[57] P. Sutter and E. Sutter, ‘Large-scale layer-by-layer synthesis of borophene on Ru(0001)’, *Chem Mater*, vol. 33, no. 22, pp. 8838–8843, 2021, doi: 10.1021/acs.chemmater.1c03061.

[58] X. Liu, Q. Li, Q. Ruan, M. S. Rahn, B. I. Yakobson, and M. C. Hersam, 'Borophene synthesis beyond the single-atomic-layer limit', *Nat Mater*, vol. 21, pp. 35–40, 2022, doi: 10.1038/s41563-021-01084-2.

[59] Q. Li *et al.*, 'Synthesis of borophane polymorphs through hydrogenation of borophene', *Science*, vol. 371, no. 6534, pp. 1143–1148, 2021, doi: 10.1126/science.abg1874.

[60] Z. Zhang, Y. Yang, E. S. Penev, and B. I. Yakobson, 'Elasticity, Flexibility, and Ideal Strength of Borophenes', *Adv Funct Mater*, vol. 27, no. 9, p. 1605059, 2017, doi: 10.1002/ADFM.201605059.

[61] M. Q. Le, B. Mortazavi, and T. Rabczuk, 'Mechanical properties of borophene films: a reactive molecular dynamics investigation', *Nanotechnology*, vol. 27, no. 44, p. 445709, 2016, doi: 10.1088/0957-4484/27/44/445709.

[62] T. Tsafack and B. I. Yakobson, 'Thermomechanical analysis of two-dimensional boron monolayers', *Phys Rev B*, vol. 93, no. 16, p. 165434, 2016, doi: 10.1103/PhysRevB.93.165434.

[63] A. J. Mannix, Z. Zhang, N. P. Guisinger, B. I. Yakobson, and M. C. Hersam, 'Borophene as a prototype for synthetic 2D materials development', *Nat Nanotech*, vol. 13, no. 6, pp. 444–450, 2018, doi: 10.1038/s41565-018-0157-4.

[64] X. F. Zhou, X. Dong, A. R. Oganov, Q. Zhu, Y. Tian, and H. T. Wang, 'Semimetallic two-dimensional boron allotrope with massless Dirac fermions', *Phys Rev Lett*, vol. 112, no. 8, pp. 1–5, 2014, doi: 10.1103/PhysRevLett.112.085502.

[65] S. Gupta, A. Kutana, and B. I. Yakobson, 'Dirac Cones and Nodal Line in Borophene', *J Phys Chem Lett*, vol. 9, no. 11, pp. 2757–2762, 2018, doi: 10.1021/acs.jpclett.8b00640.

[66] Z. Gao, M. Li, and J. S. Wang, 'Insight into two-dimensional borophene: five-center bond and phonon-mediated superconductivity', *ACS Appl Mater Interfaces*, vol. 11, no. 50, pp. 47279–47288, 2019, doi: 10.1021/acsami.9b17896.

[67] B. Feng *et al.*, 'Dirac fermions in borophene', *Phys Rev Lett*, vol. 118, no. 9, pp. 1–6, 2017, doi: 10.1103/PhysRevLett.118.096401.

[68] B. Feng *et al.*, 'Discovery of 2D anisotropic Dirac cones', *Adv Mater*, vol. 30, no. 2, pp. 2–7, 2018, doi: 10.1002/adma.201704025.

[69] C. Cheng *et al.*, 'Suppressed superconductivity in substrate-supported β_{12} borophene by tensile strain and electron doping', *2D Mater*, vol. 4, no. 2, p. 025032, 2017, doi: 10.1088/2053-1583/AA5E1B.

[70] A. Nakai, R. Rajeev, and A. Varghese, 'Synthesis, properties, and state-of-the-art advances in surface tuning of borophene for emerging applications', *Mater Today Sustain*, vol. 26, p. 100743, 2024, doi: 10.1016/J.mtsust.2024.100743.

[71] B. Mortazavi, O. Rahaman, S. Ahzi, and T. Rabczuk, 'Flat borophene films as anode materials for Mg, Na or Li-ion batteries with ultra high capacities: A first-principles study', *Appl Mater Today*, vol. 8, pp. 60–67, 2017, doi: 10.1016/j.apmt.2017.04.010.

[72] C. Fwalo, A. Kochaev, and R. E. Mapasha, 'Understanding diffusion behavior of multiple Li and Na-ions on a β_{12}-borophene electrode: A first-principles study', *Surf Sci*, vol. 755, p. 122700, 2025, doi: 10.1016/j.susc.2025.122700.

[73] P. Xiang *et al.*, 'Metallic borophene polytypes as lightweight anode materials for non-lithium-ion batteries', *Phys Chem Chem Phys*, vol. 19, no. 36, pp. 24945–24954, 2017, doi: 10.1039/c7cp04989g.

[74] S. M. Mozvashi, M. R. Givi, and M. B. Tagani, 'The effects of substrate and stacking in bilayer borophene', *Sci Rep*, pp. 1–10, 2022, doi: 10.1038/s41598-022-18076-0.

[75] M. Ebrahimi, 'The birth of bilayer borophene', *Nat Chem*, vol. 14, no. 1, pp. 3–4, 2021, doi: 10.1038/s41557-021-00868-y.

[76] B. N. Šoškić, J. Bekaert, C. Sevik, Ž. Šljivančanin, and M. V. Milošević, 'First-principles exploration of superconductivity in intercalated bilayer borophene phases', *Phys Rev Mater*, vol. 8, no. 6, p. 064803, 2024, doi: 10.1103/physrevmaterials.8.064803.

[77] D. Usachov *et al.*, 'Experimental and computational insight into the properties of the lattice-mismatched structures: Monolayers of h-BN and graphene on Ir(111)', *Phys Rev B*, vol. 86, no. 15, pp. 1–9, 2012, doi: 10.1103/PhysRevB.86.155151.

[78] M. Petrović, U. Hagemann, M. Horn-von Hoegen, and F. J. Meyer zu Heringdorf, 'Microanalysis of single-layer hexagonal boron nitride islands on Ir(111)', *Appl Surf Sci*, vol. 420, pp. 504–510, 2017, doi: 10.1016/j.apsusc.2017.05.155.

[79] W. Moritz and M. A. Van Hove, *Surface Structure Determination by LEED and X-rays*, Cambridge University Press, 2022.

[80] 'Low-energy electron diffraction'. Accessed: Oct. 05, 2025. [Online]. Available: https://www.maths.tcd.ie/~bmurphy/thesis/thesisse2.html#x9-120002.2.1

[81] T. O. Menteş and A. Locatelli, 'Angle-resolved X-ray photoemission electron microscopy', *J Electron Spectros*, vol. 185, no. 10, pp. 323–329, 2012, doi: 10.1016/j.elspec.2012.07.007.

[82] A. Locatelli, T. O. Menteş, C. A. Brondin, I. Cojocariu, and M. Jugovac, 'Advancements in X-ray photoemission electron microscopy applied to thin film magnetism, 2D materials and molecular interfaces', *Adv Phys X*, vol. 10, no. 1, 2025, doi: 10.1080/23746149.2025.2549757.

[83] A. C. Anderson *et al.*, 'Surface Studies by Scanning Tunneling Microscopy', *Phys Rev Lett*, vol. 49, no. 1, p. 57, 1982, doi: 10.1103/PhysRevLett.49.57.

[84] R. Wiesendanger, *Scanning Probe Microscopy Analytical Methods*, Springer-Verlag, 1998.

[85] P. Atkins, Julio de Paula, and J. Keeler, *Atkins' Physical Chemistry*, 11th ed. Oxford, 2018.

[86] I. Horcas, R. Fernández, J. M. Gómez-Rodríguez, J. Colchero, J. Gómez-Herrero, and A. M. Baro, 'WSXM: A software for scanning probe microscopy and a tool for nanotechnology', *Rev Sci Instrum*, vol. 78, no. 1, p. 48, 2007, doi: 10.1063/1.2432410/349965.

[87] B. Lv, T. Qian, and H. Ding, 'Angle-resolved photoemission spectroscopy and its application to topological materials', *Nat Rev Phys*, vol. 1, no. 10, pp. 609–626, 2019, doi: 10.1038/s42254-019-0088-5.

[88] K. Wandelt, *Encyclopedia of Interfacial Chemistry: Surface Science and Electrochemistry*, Elsevier, 2018.

[89] H. Zhang *et al.*, 'Angle-resolved photoemission spectroscopy', *Nat Rev Methods Primers*, vol. 2, no. 1, pp. 1–1, 2022, doi: 10.1038/s43586-022-00146-2.

[90] K. M. Omambac *et al.*, 'Interplay of kinetic limitations and disintegration: selective growth of hexagonal boron nitride and borophene monolayers on metal substrates', *ACS Nano*, vol. 17, no. 18, pp. 17946–17955, 2023, doi: 10.1021/acsnano.3c04038.

[91] Q. Yang, C. B. Wang, S. Zhang, D. M. Zhang, Q. Shen, and L. M. Zhang, 'Effect of nitrogen pressure on structure and optical properties of pulsed laser deposited BCN thin films', *Surf Coat Technol*, vol. 204, no. 11, pp. 1863–1867, 2010, doi: 10.1016/j.surfcoat.2009.11.033.

[92] A. Prakash and K. B. Sundaram, 'Deposition and XPS studies of dual sputtered BCN thin films', *Diam Relat Mater*, vol. 64, pp. 80–88, 2016, doi: 10.1016/j.diamond.2016.01.014.

[93] A. B. Preobrajenski, M. L. Ng, A. S. Vinogradov, and N. Mårtensson, 'Controlling graphene corrugation on lattice-mismatched substrates', *Phys Rev B*, vol. 78, no. 7, p. 073401, 2008, doi: 10.1103/PhysRevB.78.073401.

[94] S. Kamal *et al.*, 'Unidirectional Nano-modulated Binding and Electron Scattering in Epitaxial Borophene', *ACS Appl Mater Interfaces*, 2023, doi: 10.1021/acsami.3c14884.

[95] A. Varykhalov *et al.*, 'Ir(111) surface state with giant rashba splitting persists under graphene in air', *Phys Rev Lett*, vol. 108, no. 6, p. 066804, 2012, doi: 10.1103/PhysRevLett.108.066804.

[96] M. Bianchi *et al.*, 'Surface core level shifts of clean and oxygen covered Ir(111)', *New J Phys*, vol. 11, no. 6, p. 063002, 2009, doi: 10.1088/1367-2630/11/6/063002.

[97] S. Baronio *et al.*, 'Vibrational fine structure in C 1s high-resolution core-level spectra of CO chemisorbed on Ir(111)', *J Phys Chem C*, vol. 126, no. 3, pp. 1411–1419, 2022, doi: 10.1021/acs.jpcc.1c09646.

[98] F. H. Farwick Zum Hagen *et al.*, 'Structure and Growth of Hexagonal Boron Nitride on Ir(111)', *ACS Nano*, vol. 10, no. 12, pp. 11012–11026, 2016, doi: 10.1021/acsnano.6b05819.

[99] M. Jugovac *et al.*, 'Coupling borophene to graphene in air-stable heterostructures', *Adv Electron Mater*, vol. 9, no. 8, p. 2300136, 2023, doi: 10.1002/aelm.202300136.

[100] I. Pletikosić, M. Kralj, D. Okević, R. Brako, P. Lazić, and P. Pervan, 'Photoemission and density functional theory study of Ir(111); energy band gap mapping', *J Phys Condens Matter*, vol. 22, no. 13, p. 135006, 2010, doi: 10.1088/0953-8984/22/13/135006.

[101] I. Pletikosić *et al.*, 'Dirac cones and minigaps for graphene on Ir(111)', *Phys Rev Lett*, vol. 102, no. 5, pp. 1–4, 2009, doi: 10.1103/PhysRevLett.102.056808.

[102] D. Pacilé *et al.*, 'Artificially lattice-mismatched graphene/metal interface: Graphene/Ni/Ir(111)', *Phys Rev B*, vol. 87, no. 3, p. 035420, 2013, doi: 10.1103/PhysRevB.87.035420.

[103] A. M. Shikin, S. A. Gorovikov, V. K. Adamchuk, W. Gudat, and O. Rader, 'Electronic Structure of Carbon Nanostripes', *Phys Rev Lett*, vol. 90, no. 25, p. 4, 2003, doi: 10.1103/PhysRevLett.90.256803.

[104] M. Pisarra *et al.*, 'Electronic structure of epitaxial graphene grown on stepped Pt (997)', *Phys Rev B*, vol. 195438, pp. 1–6, 2014, doi: 10.1103/PhysRevB.89.195438.

[105] T. O. Terasawa *et al.*, 'Band gap opening in graphene by hybridization with Au (001) reconstructed surfaces', *Phys Rev Mater*, vol. 7, no. 1, p. 014002, 2023, doi: 10.1103/PhysRevMaterials.7.014002.

[106] P. M. Sheverdyaeva *et al.*, 'Electronic states of silicene allotropes on Ag(111)', *ACS Nano*, vol. 11, no. 1, pp. 975–982, 2017, doi: 10.1021/acsnano.6b07593.

[107] D. Dombrowski *et al.*, ‘Two phases of monolayer tantalum sulfide on Au(111)’, *ACS Nano*, vol. 15, no. 8, pp. 13516–13525, 2021, doi: 10.1021/acsnano.1c04249.

[108] S. Bornemann *et al.*, ‘Trends in the magnetic properties of Fe, Co, and Ni clusters and monolayers on Ir(111), Pt(111), and Au(111)’, *Phys Rev B*, vol. 86, no. 10, p. 104436, 2012, doi: 10.1103/PhysRevB.86.104436.

[109] A. Dal Corso, ‘Clean Ir(111) and Pt(111) electronic surface states: A first-principle fully relativistic investigation’, *Surf Sci*, vol. 637–638, pp. 106–115, 2015, doi: 10.1016/j.susc.2015.03.013.

[110] S. D. Kevan, ‘Observation of a new surface state on Cu(001)’, *Phys Rev B*, vol. 28, no. 4, p. 2268, 1983, doi: 10.1103/PhysRevB.28.2268.

[111] W. Jolie *et al.*, ‘Confinement of Dirac electrons in graphene quantum dots’, *Phys Rev B*, vol. 89, no. 15, p. 155435, 2014, doi: 10.1103/PhysRevB.89.155435.

[112] C. W. Ong, H. Huang, B. Zheng, R. W. M. Kwok, Y. Y. Hui, and W. M. Lau, ‘X-ray photoemission spectroscopy of nonmetallic materials: Electronic structures of boron and B_xO_y’, *J Appl Phys*, vol. 95, no. 7, pp. 3527–3534, 2004, doi: 10.1063/1.1651321.

[113] W. E. Moddeman, A. R. Burke, W. C. Bowling, and D. S. Foose, ‘Surface oxides of boron and $B_{12}O_2$ as determined by XPS’, *Surf Interface Anal*, vol. 14, no. 5, pp. 224–232, 1989, doi: 10.1002/SIA.740140503.

[114] M. Cattelan *et al.*, ‘Microscopic view on a chemical vapor deposition route to boron-doped graphene nanostructures’, *Chem Mater*, vol. 25, no. 9, pp. 1490–1495, 2013, doi: 10.1021/cm302819b.

[115] P. R. Kidambi *et al.*, ‘In situ observations during chemical vapor deposition of hexagonal boron nitride on polycrystalline copper’, *Chem Mater*, vol. 26, no. 22, pp. 6380–6392, 2014, doi: 10.1021/cm502603n.

[116] T. Hasegawa, K. Yamamoto, and Y. Kakudate, ‘Influence of raw gases on B-C-N films prepared by electron beam excited plasma CVD’, *Diam Relat Mater*, vol. 12, no. 3–7, pp. 1045–1048, 2003, doi: 10.1016/S0925-9635(03)00067-0.

[117] E. B. Aklile *et al.*, ‘Achieving ambient stability of borophene via ultrahigh vacuum alumina encapsulation’, *Nano Lett*, vol. 25, no. 25, pp. 10240–10245, 2025, doi: 10.1021/acs.nanolett.5c02510.

[118] H. Wang *et al.*, ‘Formation of Supernarrow Borophene Nanoribbons’, *Angew Chem*, vol. 63, no. 28, p. e202406535, 2024, doi: 10.1002/ANIE.202406535.

[119] Q. Zhong *et al.*, ‘Synthesis of borophene nanoribbons on Ag(110) surface’, *Phys Rev Mater*, vol. 1, no. 2, p. 021001, 2017, doi: 10.1103/PhysRevMaterials.1.021001.

[120] Q. Zhong *et al.*, ‘Metastable phases of 2D boron sheets on Ag(1 1 1)’, *J Phys Condens Matter*, vol. 29, no. 9, p. 095002, 2017, doi: 10.1088/1361-648x/aa5165.

[121] G. L. Miessler, P. J. Fischer, and D. A. Tarr, *Inorganic Chemistry*, 2014, Pearson.

[122] U. A. Schröder *et al.*, ‘Core level shifts of intercalated graphene’, *2D Mater*, vol. 4, no. 1, 2017, doi: 10.1088/2053-1583/4/1/015013.

[123] A. Fedorov *et al.*, ‘Efficient gating of epitaxial boron nitride monolayers by substrate functionalization’, *Phys Rev B*, vol. 92, no. 12, p. 125440, 2015, doi: 10.1103/PhysRevB.92.125440.

[124] J. J. Yeh and I. Lindau, ‘Subshell photoionization cross sections and asymmetry parameters: $1 \leq Z \leq 103$’, *At Data Nucl Data Tables*, vol. 32, 1985.

[125] K. N. Wood and G. Teeter, ‘XPS on Li-battery-related compounds: analysis of inorganic SEI phases and a methodology for charge correction’, *ACS Appl Energy Mater*, vol. 1, no. 9, pp. 4493–4504, 2018, doi: 10.1021/acsaem.8b00406.

[126] S. L. Qiu, C. L. Lin, J. Chen, and M. Strongin, ‘Photoemission studies of the interaction of Li and solid molecular oxygen’, *Phys Rev B*, vol. 39, no. 9, p. 6194, 1989, doi: 10.1103/PhysRevB.39.6194.

[127] A. R. Burke *et al.*, ‘Ignition mechanism of the titanium–boron pyrotechnic mixture’, *Surf Interface Anal*, vol. 11, no. 6–7, pp. 353–358, 1988, doi: 10.1002/SIA.740110614.

[128] M. Belyansky, M. Trenary, and C. Ellison, 'Boron chemical shifts in B_6O', *Surf Sci Spectra*, vol. 3, no. 2, pp. 147–150, 1994, doi: 10.1116/1.1247776.

[129] P. Pervan *et al.*, 'Li adsorption versus graphene intercalation on Ir(111): From quenching to restoration of the Ir surface state', *Phys Rev B*, vol. 92, no. 24, p. 245415, 2015, doi: 10.1103/physrevb.92.245415.

[130] S. D. Kevan, 'Perturbations on surface electronic structure induced by trace impurities: K on Cu(111)', *Surf Sci*, vol. 178, pp. 229–243, 1986.

[131] P. Matyba *et al.*, 'Controlling the electronic structure of graphene using surface-adsorbate interactions', *Phys Rev B*, vol. 92, no. 4, p. 041407, 2015, doi: 10.1103/physrevb.92.041407.

List of Figures

List of Tables